

# Theoretical and Computational Studies of Stability, Transition and Flow Control in High-Speed Flows

Principal Investigator: A. Tumin

February 22, 2011

Report Documentation Page				Form Approved OMB No. 0704-0188	
Public reporting burden for the collection of information is estimated to average 1 hour per response, including the time for reviewing instructions, searching existing data sources, gathering and maintaining the data needed, and completing and reviewing the collection of information. Send comments regarding this burden estimate or any other aspect of this collection of information, including suggestions for reducing this burden, to Washington Headquarters Services, Directorate for Information Operations and Reports, 1215 Jefferson Davis Highway, Suite 1204, Arlington VA 22202-4302. Respondents should be aware that notwithstanding any other provision of law, no person shall be subject to a penalty for failing to comply with a collection of information if it does not display a currently valid OMB control number.					
1. REPORT DATE <b>22 FEB 2011</b>		2. REPORT TYPE <b>Final</b>		3. DATES COVERED <b>18-06-2008 to 30-11-2010</b>	
4. TITLE AND SUBTITLE <b>Theoretical and computational studies of stability, transition and flow control in high-speed flows.</b>				5a. CONTRACT NUMBER <b>FA9550-08-1-0322</b>	
				5b. GRANT NUMBER	
				5c. PROGRAM ELEMENT NUMBER	
6. AUTHOR(S) <b>Anatoli Tumin</b>				5d. PROJECT NUMBER	
				5e. TASK NUMBER	
				5f. WORK UNIT NUMBER	
7. PERFORMING ORGANIZATION NAME(S) AND ADDRESS(ES) <b>University of Arizona ,888 North Euclid Avenue ,Tucson,AZ,85721-0001</b>				8. PERFORMING ORGANIZATION REPORT NUMBER <b>; AFRL-OSR-VA-TR-2011-0210</b>	
9. SPONSORING/MONITORING AGENCY NAME(S) AND ADDRESS(ES) <b>AFOSR, 875 North Randolph Street, Suite 325, Arlington, VA, 22203</b>				10. SPONSOR/MONITOR'S ACRONYM(S)	
				11. SPONSOR/MONITOR'S REPORT NUMBER(S) <b>AFRL-OSR-VA-TR-2011-0210</b>	
12. DISTRIBUTION/AVAILABILITY STATEMENT <b>Approved for public release; distribution unlimited</b>					
13. SUPPLEMENTARY NOTES					
14. ABSTRACT <b>Theoretical and computational studies of stability in high-speed boundary layers have been carried out with an emphasis on the multimode decomposition including nonparallel flow effects. The multimode decomposition can serve to analysis of DNS results for transitional boundary layers. It is shown that using the biorthogonal eigenfunction system, one can compare DNS results with theoretical predictions for the unstable and stable modes. Application of the multimode decomposition required re-evaluation of discrete modes branching and clarification of the terminology issues. Depending on flow parameters, the spectrum may have two unstable modes that are associated with inviscid instabilities of Mack first and second modes. With another choice of the parameters, the spectrum may have only one unstable mode having two maxima. Effect of chemical reactions in binary mixtures of oxygen and nitrogen has been studies within the inviscid stability analysis. In addition to the studies of high-speed boundary layers, fundamental aspects were addressed to evaluate foundations of global (bi-global) stability concept.</b>					
15. SUBJECT TERMS					
16. SECURITY CLASSIFICATION OF:			17. LIMITATION OF ABSTRACT <b>Same as Report (SAR)</b>	18. NUMBER OF PAGES <b>131</b>	19a. NAME OF RESPONSIBLE PERSON
a. REPORT <b>unclassified</b>	b. ABSTRACT <b>unclassified</b>	c. THIS PAGE <b>unclassified</b>			

# Contents

<b>1</b>	<b>Introduction</b>	<b>3</b>
<b>2</b>	<b>Numerical simulation and theoretical analysis on hypersonic boundary-layer receptivity to wall blowing-suction</b>	<b>5</b>
2.1	Introduction . . . . .	5
2.2	Outline of the multimode decomposition . . . . .	6
2.3	Direct numerical simulation approach . . . . .	8
2.4	Results . . . . .	10
2.4.1	Flat plate . . . . .	10
2.4.2	Sharp wedge . . . . .	17
2.5	Discussion of the results . . . . .	19
<b>3</b>	<b>High-speed boundary-layer instability: Old terminology and a new framework</b>	<b>24</b>
3.1	Introduction . . . . .	24
3.2	Discussion of discrete spectrum in high-speed boundary layers . . . . .	30
3.2.1	Temporal stability theory . . . . .	30
3.2.2	Spatial stability theory . . . . .	36
3.3	A model of the discrete spectrum branching . . . . .	41
3.4	Eigenfunctions of slow and fast modes . . . . .	50
3.5	Conclusions . . . . .	53
<b>4</b>	<b>Stability of boundary layers in binary mixtures of oxygen and nitrogen</b>	<b>55</b>
4.1	Introduction . . . . .	56
4.2	The real gas model . . . . .	58
4.3	The mean flow problem . . . . .	60
4.3.1	Governing equations . . . . .	60
4.3.2	Numerical method . . . . .	62
4.3.3	Some examples of the mean flow profiles . . . . .	63
4.4	Inviscid stability analysis. Governing equations and numerical method . . . .	66
4.4.1	Governing equations . . . . .	66
4.4.2	Numerical method . . . . .	70

4.5	Inviscid stability analysis. Numerical examples for reacting binary mixtures .	71
4.5.1	Oxygen . . . . .	71
4.5.2	Nitrogen . . . . .	84
4.6	Conclusion . . . . .	86
<b>5</b>	<b>Flow instabilities and transition</b>	<b>92</b>
5.1	Introduction . . . . .	92
5.2	Stability analysis of two-dimensional flows . . . . .	93
5.2.1	Outline of the linear stability theory . . . . .	93
5.2.2	Blasius boundary-layer flow . . . . .	97
5.2.3	The Falkner-Skan profiles. The pressure gradient effect . . . . .	99
5.2.4	The Rayleigh equation and structure of the TS wave at high Reynolds numbers . . . . .	101
5.2.5	The Rayleigh theorem . . . . .	103
5.2.6	Three-dimensional perturbations . . . . .	104
5.3	Receptivity of boundary layers . . . . .	105
5.4	Paths to turbulence in wall layers . . . . .	105
5.5	Transition prediction: modal growth scenario (path A) . . . . .	106
5.6	Conclusion . . . . .	108
<b>6</b>	<b>Toward the foundation of a global (bi-global) modes concept</b>	<b>110</b>
6.1	Introduction . . . . .	110
6.2	A model . . . . .	111
6.3	An example of “global” modes with the Dirichlet boundary conditions . . . .	112
6.4	Preliminary conclusions . . . . .	113
<b>7</b>	<b>Conclusions</b>	<b>114</b>
<b>A</b>	<b>Appendices to Chapter 2</b>	<b>116</b>
A.1	Comparison of DNS mean velocity and temperature profiles with the self-similar solution. Comparison of eigenvalues $\alpha = \alpha_r + i\alpha_i$ obtained using DNS and self-similar profiles. . . . .	116

# Chapter 1

## Introduction

The potential of sustained hypersonic flight to revolutionize military and commercial activity is well recognized, and is reflected in recent initiatives such as the National Aerospace Initiative. High-speed vehicles will substantially impact military strategy by providing new defensive options such as a rapid on-demand global strike capability with much shorter response times than currently possible. Furthermore, the development of new technologies based on air-breathing propulsion can be leveraged to considerably reduce the cost of access-to-space, the benefits of which are both military as well as commercial.

However, daunting technical challenges remain in realizing such vehicles. The harsh environment imposed by the envelope of such future missions is manifested in the severe anticipated thermo-mechanical loads and various propulsion-related requirements. Although the diversity of the physical phenomena encountered is broad, several key limiting issues have been identified as primary challenges, including both local and global constraints such as, for example, cowl lip loading and airframe balance. A scrutiny of the problems identified reveals the pervasive importance of several basic fluid dynamic phenomena. One of these, and possibly the least understood, is that of high-speed transition.

In the present report, the main results stemming from research supported by AFOSR grant are presented. The theoretical and computational studies of stability, transition and flow control have been carried out with an emphasis on the multimode decomposition including nonparallel flow effects. The multimode decomposition can serve to analysis of DNS results for transitional boundary layers. Application of the multimode decomposition required re-evaluation of discrete modes branching and clarification of the terminology issues. Effect of chemical reactions in binary mixtures of oxygen and nitrogen has been studied within the inviscid stability analysis. In addition to the studies of high-speed boundary layers, fundamental aspects were addressed to evaluate fundamentals of global (bi-global) stability concept.

The principal investigator is thankful to Prof. A. Fedorov, Prof. X. Zhong, Dr. J. Klentzman, Dr. X. Wang, Mr. E. Ulker for their significant input into this three-year project.

The results have been published in Encyclopedia of Aerospace Engineering, 1 journal paper and in 5 conference publications.

### **Encyclopedia of Aerospace Engineering**

1. A. Tumin, Flow Instabilities and Transition, in *Encyclopedia of Aerospace Engineering*, R. Blochley and W. Shyy (eds), John Wiley & Sons Ltd, Chichester, UK, pp. 139-150

### **Journal Paper**

1. A. Tumin, X. Wang, and X. Zhong, Numerical Simulation and Theoretical Analysis of Perturbations in Hypersonic Boundary Layers, AIAA J, Vol. 49, No. 3, 2011.

### **Conference publications**

1. A. Tumin, X. Wang, and X. Zhong, Numerical Simulation and Theoretical Analysis on Hypersonic Boundary-Layer Receptivity to Wall Blowing-Suction, Orlando FL, AIAA Paper 2010-0534, 2010.
2. A. Fedorov and A. Tumin, Branching of Discrete Modes in High-Speed Boundary Layers and Terminology Issues, Chicago IL, AIAA Paper 2010-5003, 2010.
3. E. Ulker, J. Klentzman, and A. Tumin, Stability of Boundary Layers in Binary Mixtures of Oxygen and Nitrogen, Orlando FL, AIAA Paper 2011-0370, 2011.
4. A. Tumin, X. Wang, and X. Zhong, Direct Numerical Simulation and Theoretical Analysis of Perturbations in Hypersonic Boundary Layers, in *Seventh IUTAM Symposium on Laminar-Turbulent Transition*, Proceedings of the Seventh IUTAM Symposium on Laminar-Turbulent Transition, Stockholm, Sweden, 2009, Springer, 2010, pp. 427-432.
5. A. Tumin, Toward the Foundation of a Global (Bi-Global) Modes Concept, in *Global Flow Instability and Control-IV*, Creta Maris, Hersinissos, Crete, Sept 28-Oct 2, 2009, V. Theofilis, T. Colonius, and A. Seifert eds., ISBN-13: 978-84-692-6247-4

# Chapter 2

## Numerical simulation and theoretical analysis on hypersonic boundary-layer receptivity to wall blowing-suction

This section is based on the results published in collaboration with X. Wang and X. Zhong [TWZ10, TWZ11]

### 2.1 Introduction

The progress being made in computational fluid dynamics provides an opportunity for reliable simulations of such complex phenomena as laminar-turbulent transition. The dynamics of flow transition depends on the instability of small perturbations excited by external sources. Computational results provide complete information about the flow field that would be impossible to measure in real experiments.

Recently, a method of normal mode decomposition was developed for two- and three-dimensional perturbations in compressible and incompressible boundary layers [Tum03, GT04, Tum07]. In Ref. [TWZ07], the method was applied to the theoretical analysis of a perturbation flow field in the vicinity of a blowing-suction actuator obtained from direct numerical simulation (DNS). The results demonstrated very good agreement between the amplitudes of the modes filtered out from the DNS data and those solved by linear theory of the flow receptivity to wall blowing-suction. However, the development of the perturbations downstream from the actuator has not been analyzed yet.

Perturbations observed in experiments and computations in the vicinity of an actuator possess a nonmonotonic character. This behavior occurs because the perturbation introduced by the actuator is composed of modes of the discrete (unstable and stable modes) and continuous spectra, and one cannot distinguish the unstable mode clearly. Are the observations still compatible with the linear stability theory (LST)? In order to answer this question, we must decompose the perturbation into the normal modes and compare their amplitudes with those predicted by LST. However, the LST prediction must take into account the non-

parallel boundary-layer flow effects because the development of the perturbation takes place on a length scale much larger than the boundary-layer thickness.

The nonparallel flow effects on the development of unstable discrete modes on a length scale that is much larger than the boundary-layer thickness have been studied within the scope of the method of multiple scales [Bou72, Gas74, SN75, SN77, PN79, Gap80, Nay80, EH80, TF82] (MMS). Another method that allows inclusion of the nonparallel flow effects on unstable modes is based on the parabolized stability equations [HB87, Ber91, Her97] (PSE). Fedorov and Khokhlov [FK01] pointed out that the role of decaying modes can be significant, and one has must pay attention to them if there is a synchronism with the other modes. Because the analysis of decaying modes is important, one must include the nonparallel boundary-layer flow effects using the MMS.

In the present work, we apply the multimode decomposition to DNS results downstream from the blowing-suction actuator in hypersonic boundary layers past a flat plate and a sharp wedge to compare the amplitudes of the modes found from the computations with the prediction of the linear stability theory including nonparallel flow effects.

## 2.2 Outline of the multimode decomposition

The method of multimode decomposition of perturbations having a prescribed frequency is based on the biorthogonal eigenfunction system for linearized Navier-Stokes equations [Tum07]. For the clarity of further discussion, we reproduce the main definitions necessary for discussing the present work.

We consider a compressible two-dimensional boundary layer in Cartesian coordinates, where  $x$  and  $z$  are the downstream and spanwise coordinates, respectively, and coordinate  $y$  corresponds to the distance from the wall. We write the linearized Navier-Stokes equations for a periodic-in-time perturbation (the frequency is equal to zero in the case of a roughness-induced perturbation),  $\sim \exp(-i\omega t)$ , in matrix form as

$$\frac{\partial}{\partial y} \left( \mathbf{L}_0 \frac{\partial \mathbf{A}}{\partial y} \right) + \mathbf{L}_1 \frac{\partial \mathbf{A}}{\partial y} = \mathbf{H}_1 \mathbf{A} + \mathbf{H}_2 \frac{\partial \mathbf{A}}{\partial x} + \mathbf{H}_3 \frac{\partial \mathbf{A}}{\partial z} + \mathbf{H}_4 \mathbf{A}, \quad (2.1)$$

where vector  $\mathbf{A}$  has 16 components

$$\mathbf{A}(x, y, z) = (u, \partial u / \partial y, v, \pi, \theta, \partial \theta / \partial y, w, \partial w / \partial y, \partial u / \partial x, \partial v / \partial x, \partial \theta / \partial x, \partial w / \partial x, \partial u / \partial z, \partial v / \partial z, \partial \theta / \partial z, \partial w / \partial z)^T. \quad (2.2)$$

$\mathbf{L}_0, \mathbf{L}_1, \mathbf{H}_1, \mathbf{H}_2, \mathbf{H}_3$ , and  $\mathbf{H}_4$  are  $16 \times 16$  matrices (their definitions are given in Ref. [Tum08]);  $u, v, w, \pi$ , and  $\theta$  represent three velocity components, pressure, and temperature perturbations, respectively; and the superscript  $T$  in (2.2) stands for transpose. Matrix  $\mathbf{H}_4$  originates from the nonparallel character of the flow. It includes terms with the  $y$ -component of the mean flow velocity and derivatives of the mean flow profiles with respect to the coordinate  $x$ .

In the quasi-parallel flow approximation, the solution of the linearized Navier-Stokes equations can be expanded into normal modes of the discrete and continuous spectra  $\{\mathbf{A}_{\alpha\beta}, \mathbf{B}_{\alpha\beta}\}$



[Tum07], where  $\mathbf{A}_{\alpha\beta}$  and  $\mathbf{B}_{\alpha\beta}$  are eigenfunctions of the direct and adjoint problems. Subscripts  $\alpha$  and  $\beta$  indicate the eigenfunctions corresponding to the streamwise,  $\alpha$ , and spanwise,  $\beta$ , wave numbers, respectively. The eigenfunction system  $\{\mathbf{A}_{\alpha\beta}, \mathbf{B}_{\alpha\beta}\}$  has an orthogonality relation given as

$$\langle \mathbf{H}_2 \mathbf{A}_{\alpha\beta}, \mathbf{B}_{\alpha'\beta} \rangle \equiv \int_0^\infty (\mathbf{H}_2 \mathbf{A}_{\alpha\beta}, \mathbf{B}_{\alpha'\beta}) dy = \Gamma \Delta_{\alpha\alpha'}, \quad (2.3)$$

where  $\Gamma$  is a normalization constant,  $\Delta_{\alpha\alpha'}$  is a Kronecker delta if either  $\alpha$  or  $\alpha'$  belongs to the discrete spectrum, and  $\Delta_{\alpha\alpha'}$  is a Dirac delta function if both  $\alpha$  and  $\alpha'$  belong to the continuous spectrum.

The orthogonality relation (2.3) can be used for decomposition of the DNS data at  $x = x_0$  into normal modes. After applying the Fourier transform in  $z$ , the data can be presented in the form of a vector

$$\mathbf{A}_{\beta 0}(x_0, y) = \sum_{\alpha} C_{\alpha}(\beta) \mathbf{A}_{\alpha\beta}(x_0, y), \quad (2.4)$$

where  $\sum$  stands for summation and integration over the discrete and continuous spectra, respectively. Applying the orthogonality relation (2.3), one can find the coefficients  $C_{\alpha}(\beta)$  as follows:

$$C_{\alpha}(\beta) = \frac{\langle \mathbf{H}_2 \mathbf{A}_{\beta 0}(\mathbf{x}_0, \mathbf{y}), \mathbf{B}_{\alpha\beta} \rangle}{\Gamma}. \quad (2.5)$$

In the case of the transient growth phenomenon studied in experiments [Whi02, WE03, FBTC04, WRE05, DW08] and DNS [FC04, RV07, SAD<sup>+</sup>09], the flow perturbation is given only by modes of the continuous spectrum. The multimode decomposition has been applied by Denissen and White [DW09] to the analysis of the DNS data of Rizzetta and Visbal [RV07]. The authors demonstrated that the method can be utilized even when only partial information in vector  $\mathbf{A}_{\beta 0}(x_0, y)$  is available.

In a weakly nonparallel flow, one can employ the method of multiple scales (MMS) by introducing fast ( $x$ ) and slow ( $X = \varepsilon x, \varepsilon \ll 1$ ) scales. The mean flow profiles depend on  $y$  and  $X$  only, whereas the perturbation will depend on both length scales. In the case of a discrete mode, the solution of the linearized Navier-Stokes equation is presented in the form

$$\mathbf{A}_{\beta}(x, X, y) = \left[ D_{\nu}(X) \mathbf{A}_{\alpha\nu\beta}^{(0)}(X, y) e^{i \int \alpha_{\nu}(X) dx} + \varepsilon \mathbf{A}_{\alpha\nu\beta}^{(1)}(X, y) e^{i \int \alpha_{\nu}(X) dx} + \dots \right], \quad (2.6)$$

where the function  $D_{\nu}(X)$  must be determined. After substitution of Eq. (2.6) into Eq. (2.1), we arrive in order  $O(\varepsilon)$  at an inhomogeneous equation for  $\mathbf{A}_{\alpha\nu\beta}^{(1)}$ . The solvability condition of this equation allows for the finding of  $D_{\nu}(X)$  (details and relevant references can be found in Ref. [Tum08]).

## 2.3 Direct numerical simulation approach

In direct numerical simulation, the receptivity of hypersonic boundary layers over a flat plate and a sharp wedge to wall blowing-suction are considered by solving the two-dimensional compressible Navier-Stokes equations. Wall blowing-suction is introduced by a slot located near the leading edge. In the assumption of thermally and calorically perfect gas flows, the governing equations in conservative variables are given as

$$\frac{\partial \vec{U}}{\partial t} + \frac{\partial}{\partial x}(\vec{F}_{1i} + \vec{F}_{1v}) + \frac{\partial}{\partial y}(\vec{F}_{2i} + \vec{F}_{2v}) = 0, \quad (2.7)$$

where  $\vec{U}$  is a column vector containing the conservative variables,

$$\vec{U} = \{\rho, \rho u, \rho v, e\}^T. \quad (2.8)$$

The flux vectors in (2.7) are divided into their inviscid and viscous components due to the fact that the two components are discretized with different schemes. The components,  $\vec{F}_{1i}$  and  $\vec{F}_{2i}$ , are inviscid flux whereas  $\vec{F}_{1v}$  and  $\vec{F}_{2v}$  are viscous flux components,

$$\vec{F}_{ji} = \begin{bmatrix} \rho u_j \\ \rho u u_j + p \Delta_{1j} \\ \rho v u_j + p \Delta_{2j} \\ u_j(e + p) \end{bmatrix}, \quad (2.9)$$

$$\vec{F}_{jv} = \begin{bmatrix} 0 \\ -\tau_{xxj} \\ -\tau_{yxj} \\ -\tau_{x_k x_j} u_k - K \frac{\partial T}{\partial x_j} \end{bmatrix}, \quad (2.10)$$

with  $j, k \in (1, 2)$ . In Cartesian coordinates,  $x_1$  and  $u_1$  are defined in the streamwise direction ( $x$  and  $u$ ) whereas  $x_2$  and  $u_2$  are defined in the wall-normal direction ( $y$  and  $v$ ).

Under the perfect gas assumption, pressure and energy are given by

$$p = \rho R T, \quad (2.11)$$

$$e = \rho c_v T + \frac{\rho}{2}(u^2 + v^2), \quad (2.12)$$

where  $c_v$  is the specific heat at constant volume. In the simulation, the viscosity coefficient,  $\mu$ , and the heat conductivity,  $K$ , are calculated using Sutherland's law together with a constant Prandtl number,  $Pr$ . They are both functions of temperature only.

$$\mu = \mu_r \left( \frac{T}{T_r} \right)^{3/2} \frac{T_r + T_s}{T + T_s}, \quad (2.13)$$

$$K = \frac{\mu c_p}{Pr}, \quad (2.14)$$

where  $\mu_r = 1.7894 \times 10^{-5}$  Ns/m<sup>2</sup>,  $T_r = 288.0$  K,  $T_s = 110.33$  K, and  $c_p$  is the specific heat at constant pressure.

The scales of velocity and length are the free-stream velocity  $U_\infty$  and the Blasius length scale,  $L = (\mu_\infty x / \rho_\infty U_\infty)^{1/2}$ . Since the length scale is changing along the flat plate, it is not convenient to scale the frequency in terms of  $L/U_\infty$ . Instead, the frequency is scaled as follows:

$$F = \frac{2\pi f \mu_\infty}{\rho_\infty U_\infty^2} = \frac{\omega \mu_\infty}{\rho_\infty U_\infty^2}. \quad (2.15)$$

In boundary layer analysis, the Reynolds number based on the Blasius length scale is generally used,

$$R = \frac{\rho_\infty U_\infty L}{\mu_\infty}. \quad (2.16)$$

In the present work, the fifth-order shock-fitting finite difference method of Zhong [Zho98] is used to solve the governing equations in a domain bounded by the bow shock and the flat plate (or wedge). In other words, the bow shock is treated as a boundary of the computational domain. The Rankine-Hugoniot relations across the shock and a characteristic compatibility relation coming from the downstream flow field are combined to solve for the flow variables behind the shock. The shock-fitting method makes it possible for the Navier-Stokes equations to be spatially discretized by high-order finite difference methods. Specifically, a fifth-order upwind scheme is applied to discretize the inviscid flux derivatives. By using the shock-fitting method, the interaction between the bow shock and the wall blowing-suction induced perturbations is solved as a part of the solutions with the position and velocity of the shock front being solved as dependent variables. Both of the cases correspond to an adiabatic wall boundary condition.

The numerical simulations in the current paper have been well validated. For the flow over the flat plate, three sets of grid structures are used to check the grid independence of numerical simulation results near the leading edge. The steady flow is compared with the experimental measurements of Maslov et al. [MSSA01]. At three different locations,  $x = 96$  mm, 121 mm, and 138 mm ( $R = 1134.46, 1254.19, 1329.66$ ), the distributions of the dimensionless streamwise velocity and normalized Mach number in the wall-normal direction are in good agreement with those measured in experiments. Two sets of the grid structures are used to check grid independence of unsteady numerical simulations. The comparison of pressure perturbation amplitudes calculated using the two grid structures shows that the grid structure used for the simulation is sufficient. Details of the validations are presented in Ref. [WZ09]. In Ref. [TWZ07], validations of the numerical simulation results on the sharp wedge were carried out for both steady and unsteady flows. Furthermore, the numerical perturbation field just downstream of the blowing-suction slot was decomposed into boundary-layer waves. The amplitudes of the decomposed waves were in good agreement with those obtained from a theoretical receptivity model.

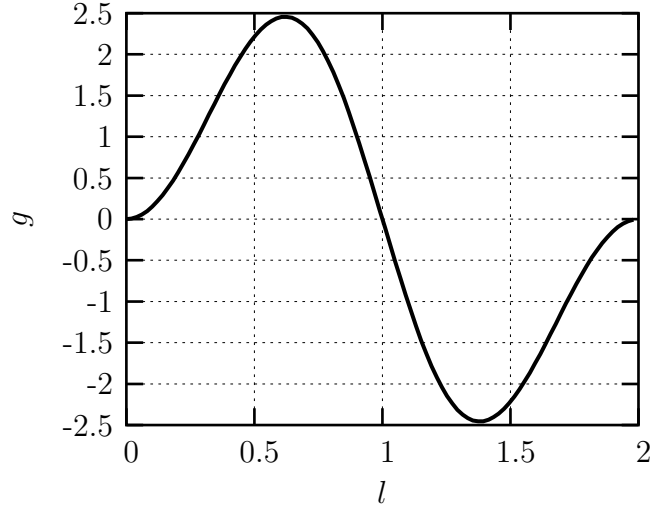


Figure 2.1: Amplitude distribution of the blowing-suction through the slot.

## 2.4 Results

### 2.4.1 Flat plate

The free-stream flow conditions that we consider are: Mach number  $M_\infty = 5.92$ , temperature  $T_\infty = 48.69$  K, pressure  $p_\infty = 742.76$  Pa. The Prandtl number and the specific heat ratio are 0.72 and 1.4, respectively. The free stream flow parameters are the same as those of Maslov *et al.* [MSSA01].

The viscosity coefficient is calculated by Sutherland's law. The dimensionless blowing-suction of mass flux at the wall is expressed as

$$\begin{aligned}
 (\rho v)' &= \epsilon g(l) S(t), \quad \epsilon = 0.405 \times 10^{-5}, \\
 g(l) &= \begin{cases} 20.25l^5 - 35.4375l^4 + 15.1875l^2, & (l \leq 1); \\ -20.25(2-l)^5 + 35.4375(2-l)^4 - 15.1875(2-l)^2, & (l > 1), \end{cases} \\
 l(x) &= \frac{2(x - x_i)}{(x_e - x_i)}, \quad x_i \leq x \leq x_e,
 \end{aligned} \tag{2.17}$$

where  $x_i = 33$  mm and  $x_e = 37$  mm are the coordinates of the leading and the trailing edges of the slot, respectively. The amplitude distribution,  $g(l)$ , is shown in Fig. 2.1.

The function of time  $S(t)$  in (2.17) is defined as

$$S(t) = \begin{cases} 1, & \text{mod}(t, 20\mu s) \leq 2\mu s; \\ 0, & \text{mod}(t, 20\mu s) > 2\mu s. \end{cases} \tag{2.18}$$

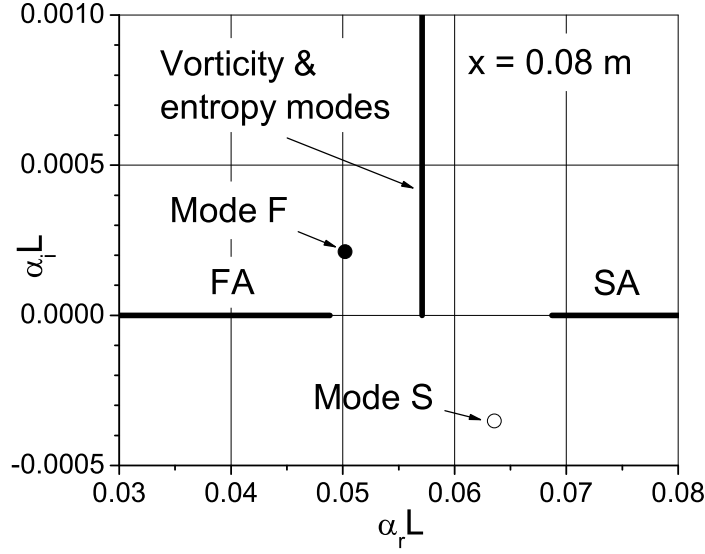


Figure 2.2: Discrete modes and the continuous spectrum.

The function  $S(t)$  can be expressed as a Fourier series.

Analyses of the mean flow velocity, temperature profiles and their derivatives have shown that they agree well with the self-similar solution for a boundary layer over a flat plate (see Appendix A.1). Only the second derivatives of the velocity and temperature profiles demonstrate some differences between the DNS results and the self-similar solution. Because of the viscous-inviscid interaction, the edge velocity,  $U_e$ , and temperature,  $T_e$ , are slightly different from the free-stream values  $U_\infty$  and  $T_\infty$ , respectively. Therefore, the local edge Mach number  $M_e$  also is different from the free stream Mach number. However, the viscous-inviscid interaction is weak at the considered flow parameters. For example, we consider the flow parameters outside the boundary layer at  $y/L \approx 50$ , where the length scale  $L$  is defined as  $(\mu_\infty x / \rho_\infty U_\infty)^{1/2}$ . At  $x = 0.099$  m,  $0.359$  m, and  $0.659$  m, the dimensionless velocities and the local Mach numbers are equal to  $U/U_\infty = 0.9983, 0.9992, 0.9994$ , and  $M_e = 5.845, 5.882, 5.892$ , respectively. Therefore, we neglect these small variations in the local Mach number  $M_e$ , in the edge velocity,  $U_e$ , and temperature,  $T_e$ , and consider them to be equal to the free-stream parameters.

Comparison of the eigenvalues  $\alpha$  obtained using the self-similar and DNS profiles is shown in Appendix A.1. There is a difference in  $\alpha_i$  at high frequencies. In the analysis of the flat plate data, the self-similar profiles have been used in the stability equations. The analysis of the perturbations is limited to the DNS data corresponding to perturbations of 100 kHz only. The corresponding dimensionless frequency is  $55.02939 \times 10^{-6}$ . In order to deal with the two-dimensional perturbations within the solver of Refs. [Tum07, Tum08], the spanwise wave number  $\beta$  scaled with the Blasius length scale,  $L$ , was chosen equal to  $10^{-5}$ .

In order to illustrate further analysis of DNS results, features of the spectrum should

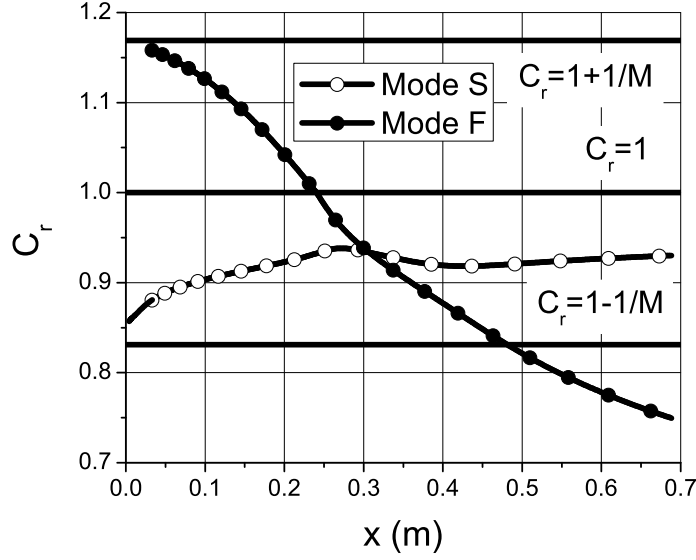


Figure 2.3: Real parts of the phase velocities of the discrete modes F and S scaled with the free-stream velocity  $U_\infty$ .

be introduced. Figure 2.2 shows the branches of the continuous spectrum and two discrete modes at  $x = 0.08$  m ( $R = 1063.02$ ). One of the discrete modes is labeled mode F (fast); the other is labeled mode S (slow). The mode names stem from their phase velocity features in the vicinity of the leading edge. One can see in Fig. 2.3 that mode S is synchronized with the slow acoustic wave ( $c_r = 1 - 1/M_\infty$ ), whereas mode F is synchronized with the fast acoustic wave ( $c_r = 1 + 1/M_\infty$ ). At the chosen flow parameters, mode F is always stable, and mode S is the unstable mode. One can see that mode F is synchronized with the vorticity/entropy modes having dimensionless phase velocity  $c_r = 1$  at  $x \approx 0.25$  m ( $R = 1879.17$ ). The significance of the decaying mode F stems from its synchronization with mode S, where the decaying mode can give rise to the unstable mode (switching of the modes), which may lead to transition [FK01].

Mode S.

Figure 2.4 shows the pressure perturbation on the wall (scaled with the free-stream pressure) obtained in the DNS and projections onto the discrete mode S. Amplification of the discrete mode evaluated with and without the nonparallel flow effects (MMS and LST, respectively) is also presented in Fig. 2.4. One can see that the nonparallel flow effect is significant in this example. The DNS data for the wall pressure perturbation have wiggles near the actuator region due to input from the various modes presented in the signal (Fig. 2.5). The filtered out amplitude of the unstable mode S is smooth, and it is in good agreement with the theoretical prediction on the whole interval.

Mode F

It is interesting to look at the filtered out decaying mode F on Fig 2.6. It is in good

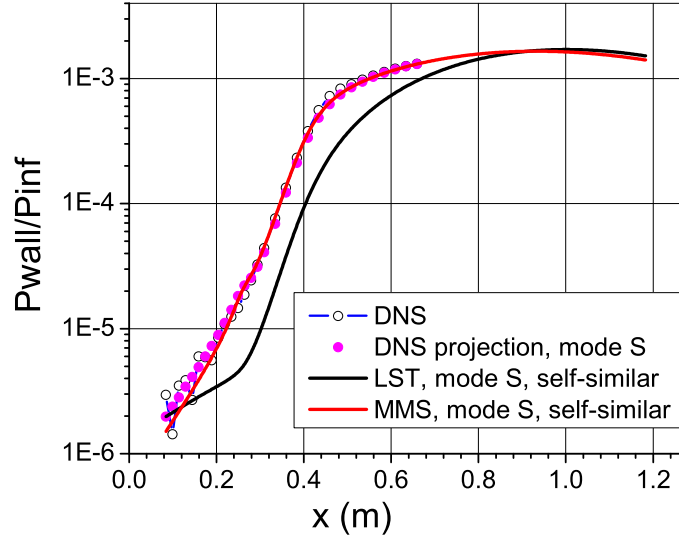


Figure 2.4: Projection of the DNS results onto the discrete mode S.

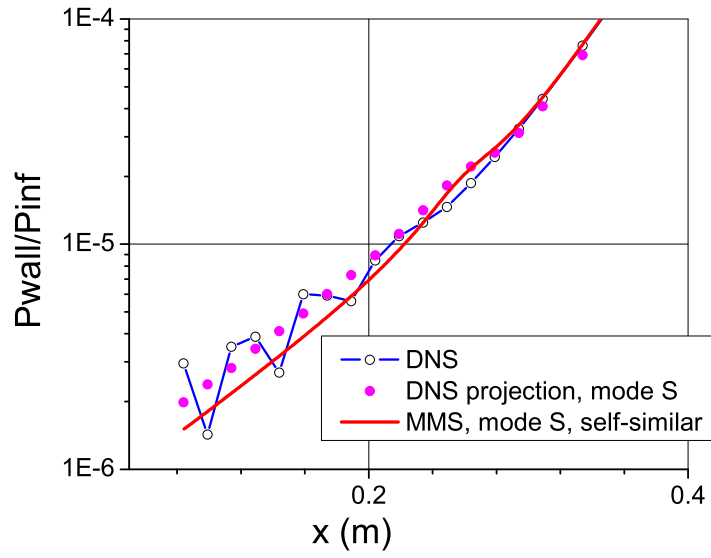


Figure 2.5: A closer view of the results in Fig. 2.4 in the vicinity of the actuator.

agreement with the theoretical prediction up to  $x \approx 0.25$  m. After that, it experiences a jump and the amplitude becomes comparable with the amplitude of mode S. The result can be attributed to the next term in the expansion (2.6). The second term,  $\mathbf{A}_{\alpha_S\beta}^{(1)}(X, y)$ , can be expanded into the eigenfunction system. It is the standard problem of finding eigenfunctions of a perturbed operator using the unperturbed basis [Fri90]. For the non-resonance case when eigenvalues of modes F and S are distinct ( $\alpha_S \neq \alpha_F$ ), it is straightforward to find a projection of  $\mathbf{A}_{\alpha_S\beta}^{(1)}(X, y)$  onto  $\mathbf{A}_{\alpha_F\beta}(X, y)$  (indices S and F indicate slow and fast discrete modes, respectively).

After applying of the Fourier transform to the linearized equations (2.1) with respect to coordinate  $z$  and substitution of  $\mathbf{A}_\beta(x, X, y)$ , one can derive the following equation for  $\mathbf{A}_{\alpha_S\beta}^{(1)}(X, y)$ :

$$\begin{aligned} \frac{\partial}{\partial y} \left( \mathbf{L}_0 \frac{\partial \mathbf{A}_S^{(1)}}{\partial y} \right) + \mathbf{L}_1 \frac{\partial \mathbf{A}_S^{(1)}}{\partial y} - \mathbf{H}_1 \mathbf{A}_S^{(1)} - i\alpha_S \mathbf{H}_2 \mathbf{A}_S^{(1)} - i\beta \mathbf{H}_3 \mathbf{A}_S^{(1)} &= \Phi, \\ \Phi \equiv \frac{dD_S(X)}{dX} \mathbf{H}_2 \mathbf{A}_S^{(0)} + D_S(X) \mathbf{H}_2 \frac{\partial \mathbf{A}_S^{(0)}}{\partial X} + D_S(X) \bar{\mathbf{H}}_4 \mathbf{A}_S^{(0)}, \end{aligned} \quad (2.19)$$

where  $\bar{\mathbf{H}}_4 = \varepsilon^{-1} \mathbf{H}_4$ . For the purpose of brevity, we use subscript  $S$  to indicate the slow discrete mode having wave numbers  $\alpha_S$ . One can represent the solution for  $\mathbf{A}_S^{(1)}$  as an expansion into the eigenfunctions of the undisturbed operator. In symbolic form, we write

$$\mathbf{A}_S^{(1)} = \sum_{\alpha_k \neq \alpha_S} C_k(X) \mathbf{A}_k^{(0)}. \quad (2.20)$$

The symbolic form of the expansion (2.20) means that we include expansion into the discrete modes and continuous spectrum as well. Assuming that there is no resonance ( $\alpha_k \neq \alpha_S$ ), one can substitute  $\mathbf{A}_S^{(1)}$  from Eq. (2.20) into Eq. (2.19). Using the dot product with the adjoint eigenvector  $\mathbf{B}_F^{(0)}$ , we arrive at the coefficient  $C_F$ :

$$C_F(X) = \frac{D_S(X)}{i(\alpha_F - \alpha_S)} \frac{\left\langle \mathbf{H}_2 \frac{\partial \mathbf{A}_S^{(0)}}{\partial X}, \mathbf{B}_F^{(0)} \right\rangle + \left\langle \bar{\mathbf{H}}_4 \mathbf{A}_S^{(0)}, \mathbf{B}_F^{(0)} \right\rangle}{\left\langle \mathbf{H}_2 \mathbf{A}_F^{(0)}, \mathbf{B}_F^{(0)} \right\rangle}. \quad (2.21)$$

The input of mode F into the second term of Eq. (2.6) has a wave number (and phase speed) corresponding to mode S. We refer to this contribution of the mode F as ‘‘S2F centaur’’ in order to emphasize the two-fold character of the term. The wall pressure perturbation associated with S2F centaur is shown in Fig. 2.7. Although the theoretical result for mode F downstream from the point of synchronism demonstrates qualitatively the same qualitative behavior as the amplitude of the DNS projection onto the mode F, there is a quantitative discrepancy that has yet to be understood.

Velocity profiles of modes S and F

Having found the coefficients in the projection of the DNS results onto modes  $S$  and  $F$ , we can compare the velocity profiles of the modes with the DNS results in order to evaluate their significance at different distances from the actuator.



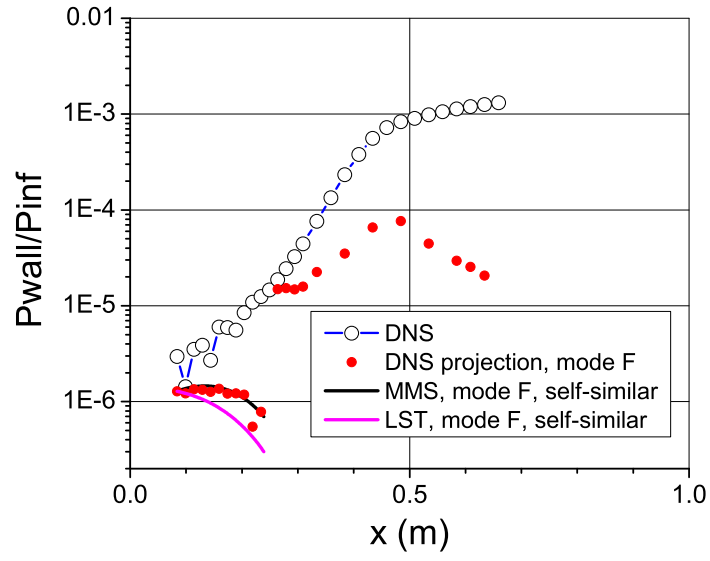


Figure 2.6: Projection of the DNS results onto the discrete mode F.

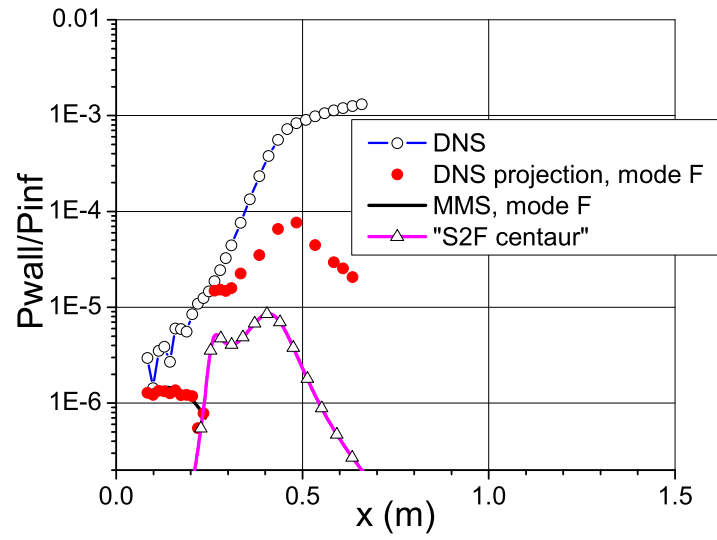


Figure 2.7: Projection of the DNS results onto the discrete mode F, and amplitude of S2F centaur.

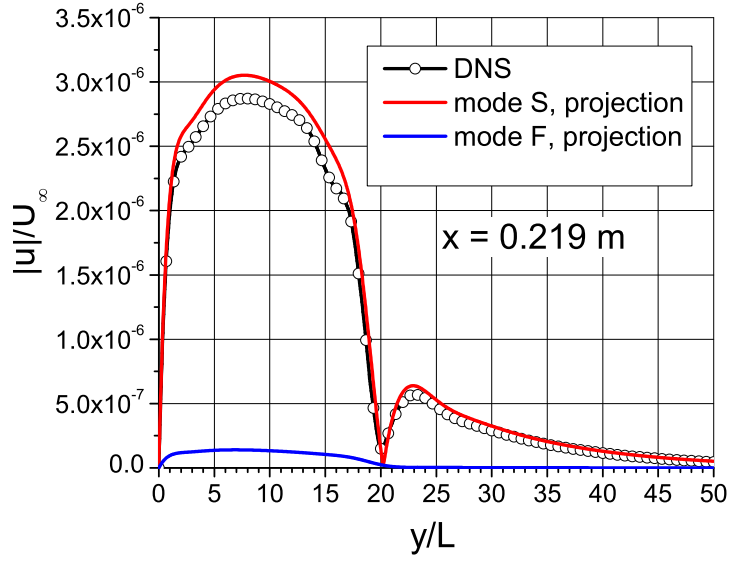


Figure 2.8: Streamwise velocity perturbation at  $x = 0.219$  m.

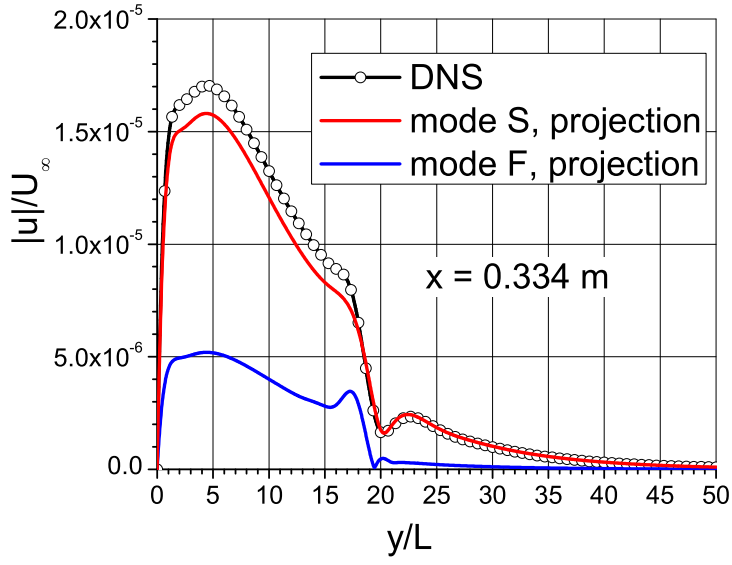


Figure 2.9: Streamwise velocity perturbation at  $x = 0.334$  m.

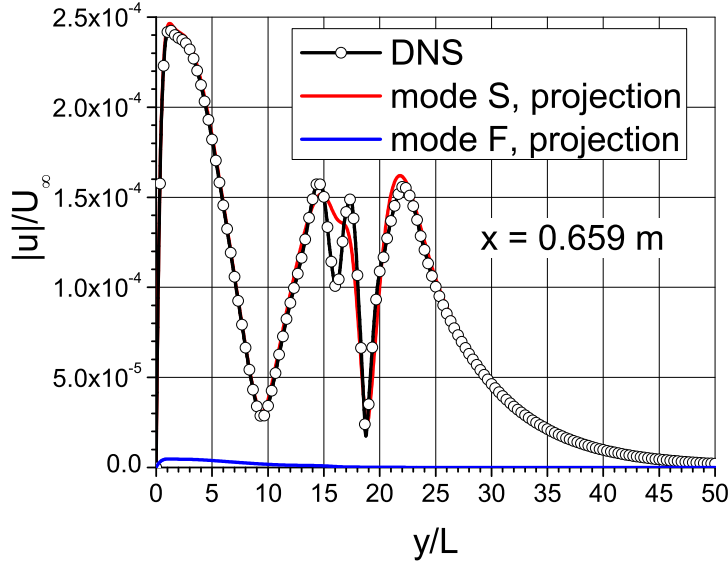


Figure 2.10: Streamwise velocity perturbation at  $x = 0.659$  m.

One can see that the main input into the velocity perturbation stems from mode S. In the vicinity of the modes' synchronism, the amplitude of mode F is higher as expected from results presented in Fig. 2.7. The receptivity studies in Ref. [TWZ07] showed that the amplitude of mode F in the vicinity of the actuator is higher than the amplitude of mode S. In the present work, we consider perturbations far downstream from the actuator, and mode S has a larger amplitude than mode F.

### 2.4.2 Sharp wedge

In this example, periodic-in-time wall blowing-suction was introduced into the boundary layer over a wedge of half-angle 5.3 degrees. The free-stream flow conditions were: Mach number  $M_\infty = 8$ , temperature  $T_\infty = 54.8$  K, pressure  $p_\infty = 389$  Pa. The Prandtl number and the specific heats ratio are 0.72 and 1.4, respectively. The viscosity coefficient is calculated by Sutherland's law. The flow parameters are the same as in the work by Malik *et al.* [MLS99]. Results of Ref. [MLS99] were used for the validation of the code used in the present work (see Ref. [TWZ07]).

The periodic-in-time blowing-suction slot has coordinates of the leading and trailing edges at  $x_i = 51.84$  mm and  $x_e = 63.84$  mm, respectively. These flow parameters and the actuator location correspond to Case 3 considered in Ref. [TWZ07]. The dimensionless wall blowing-suction of mass flux at the wall is expressed as

$$(\rho v)' = q_0 g(l) \sum_{n=1}^{15} \sin(\omega_n t), \quad (2.22)$$

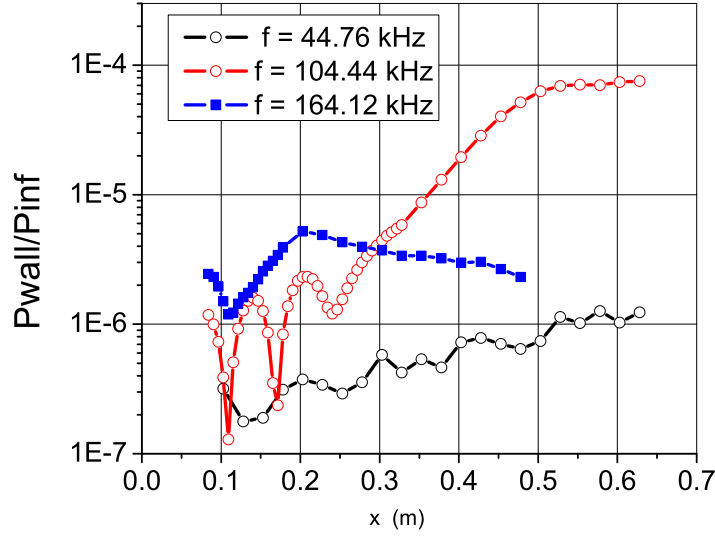


Figure 2.11: Pressure perturbations ( $p_{wall}/p_{\infty}$ ) on the wedge at three frequencies.

where  $q_0 = 0.734 \times 10^{-7}$  is a dimensionless amplitude parameter, scaled by the free-stream streamwise mass flux; function  $g(l)$  is defined in Eq. (2.17), and  $\omega_n$  is the circular frequency of the multi-frequency perturbations.

Figure 2.11 illustrates the pressure perturbations on the wedge at three frequencies: 44.76 kHz, 104.44 kHz, and 164.12 kHz (the dimensionless frequencies  $\omega \mu_e / (\rho_e U_e^2)$  scaled with the local boundary-layer edge parameters are approximately  $21.4 \times 10^{-6}$ ,  $50.0 \times 10^{-6}$ , and  $78.6 \times 10^{-6}$ , respectively). Figure 2.12 shows the local Reynolds number  $R = (\rho_e x / \mu_e U_e)^{1/2}$  versus coordinate  $x$ .

In the following examples, analysis of the flow stability was based on the velocity and temperature profiles obtained from the computations without an assumption about the self-similar character of the boundary layer flow. In order to compare the projected amplitudes with those predicted using the method of multiple scales, we need derivatives  $\partial/\partial x$  of the streamwise velocity and temperature profiles of the mean flow. These derivatives were derived using the computational profiles together with the assumption that the profiles locally are self-similar.

Figure 2.13 shows the imaginary part of the wave number  $\alpha$  scaled with  $L = (\mu_{\infty} x / \rho_{\infty} U_{\infty})^{1/2}$  obtained using the quasi-parallel approximation (LST) and using the method of multiple scales (MMS) for perturbations of  $F = 44.6$  kHz. Figure 2.14 shows wall pressure perturbations in DNS results and in their projection onto mode S together with the theoretical prediction when the nonparallel flow effects are included. Figures 2.15 and 2.16 show similar results corresponding to frequency  $f = 104.44$  kHz. Figs. 2.17 and 2.18 demonstrate the results at frequency  $f = 164.12$  kHz. It is interesting that the nonparallel flow effect on  $\alpha_i L$  has a different character at low and high local Reynolds numbers (see Figs. 2.15 and

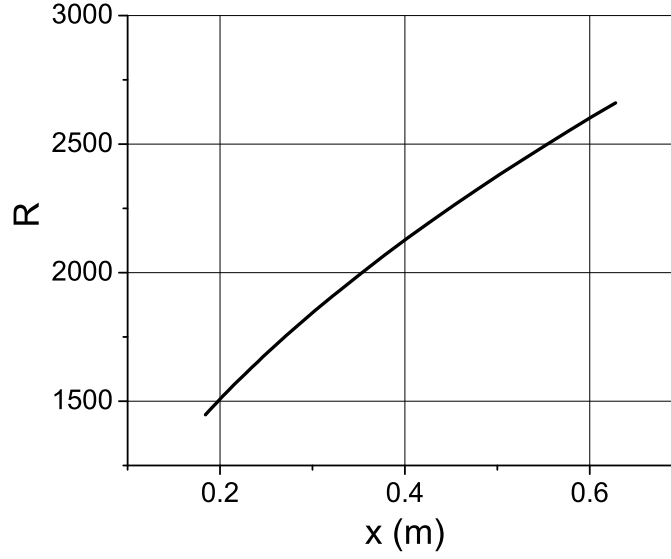


Figure 2.12: The local Reynolds number versus coordinate  $x$ .

2.17). Using Mack's terminology [Mac69], mode  $S$  is associated with the "first Mack's mode" and the "second Mack's mode" at low and high local Reynolds numbers, respectively (see clarification of the terminology in Ref. [FT10]). The nonparallel flow effects destabilize the first mode and stabilize the second mode. The same observation was reported by Chang and Malik [CM93]. Appearance of the strong hump in  $\alpha_i L$  at low Reynolds numbers as seen in Figs. 2.15 and 2.17 is attributed to the transformation of the first mode into the second one [CM93].

## 2.5 Discussion of the results

The presented results illustrate how the multimode decomposition technique may serve as a tool for gaining insight into the flow dynamics in the presence of perturbations belonging to different modes. In the past, one could compare DNS results with theoretical prediction for the unstable mode only far downstream from an actuator where the unstable mode dominates the total signal. Using the biorthogonal eigenfunction system, one can compare DNS results with theoretical predictions for the unstable and stable modes in the vicinity of the actuator as well.

In Ref. [TWZ07] and in the present work, we have found that the multimode decomposition requires a more elaborate analysis within the point of synchronism of mode F with the continuous spectrum. Therefore, an extension of the theoretical model of Ref. [FK01] to the case of continuous spectrum is required.

Analysis of the growth rates using the method of multiple scales revealed that they have

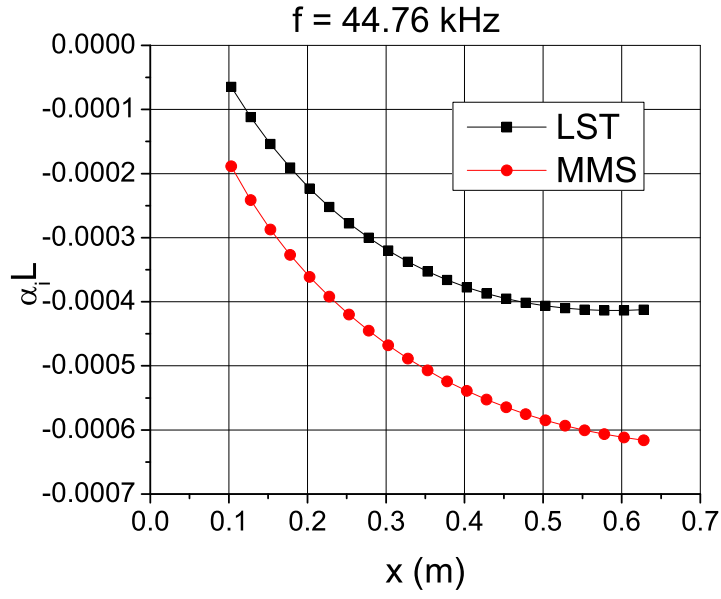


Figure 2.13:  $Im(\alpha_i)$  versus  $x$  at frequency  $f = 44.76$  kHz.

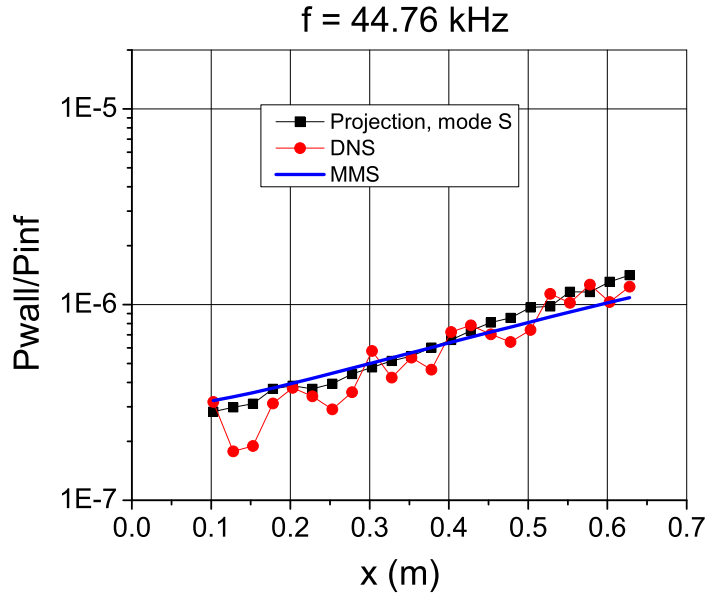


Figure 2.14: Projection of the DNS results onto the discrete mode S and comparison with the theoretical prediction using the method of multiple scales (MMS).  $f = 44.76$  kHz.

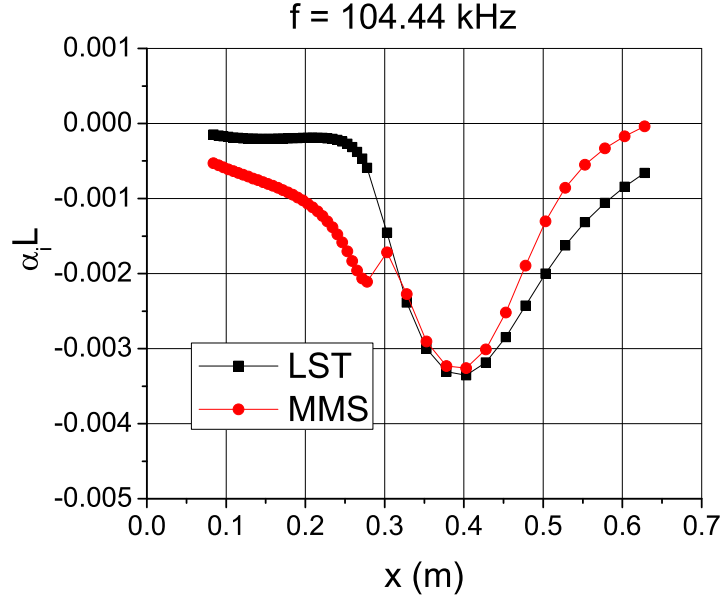


Figure 2.15:  $Im(\alpha_i)$  versus  $x$  at frequency  $f = 104.44$  kHz.

a non-monotonic character in the region where the first Mack's mode is transformed into the second one (the terminology regarding Mack's modes is clarified in Ref. [FT10]). This observation is in agreement with studies in Ref. [CM93]. The nonparallel flow effects in the boundary layer over an adiabatic wall destabilize the first mode and stabilize the second one.

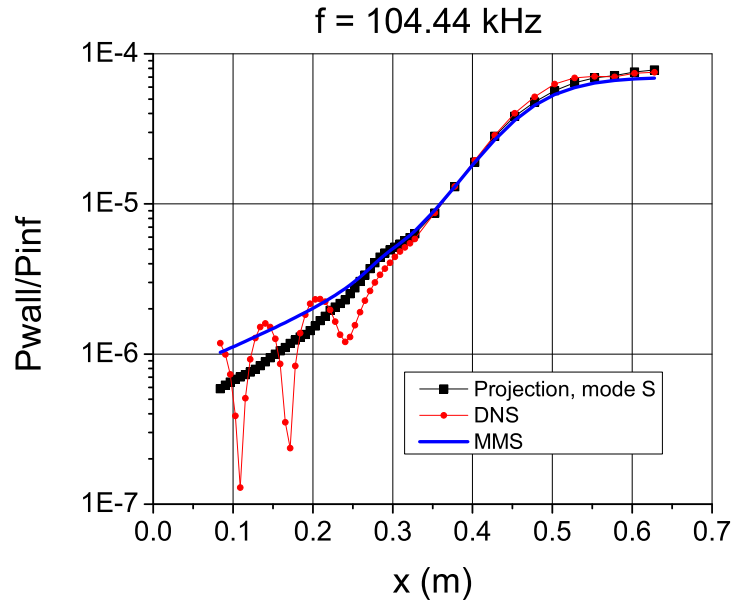


Figure 2.16: Projection of the DNS results onto the discrete mode S and comparison with the theoretical prediction using the method of multiple scales (MMS).  $f = 104.44$  kHz.

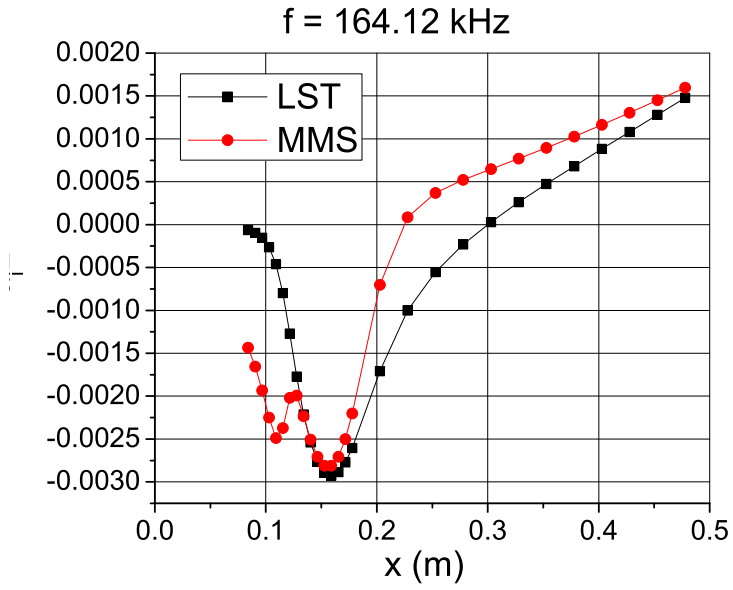


Figure 2.17:  $Im(\alpha_i)$  versus  $x$  at frequency  $f = 164.12$  kHz.



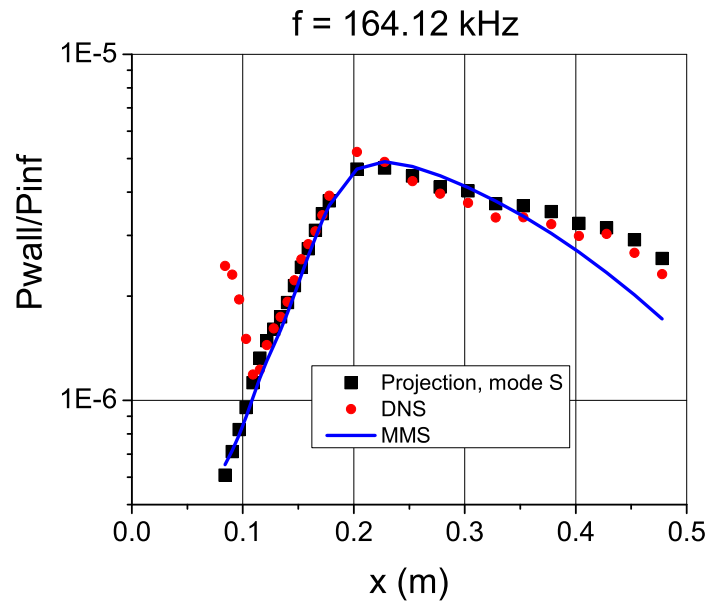


Figure 2.18: Projection of the DNS results onto the discrete mode S and comparison with the theoretical prediction using the method of multiple scales (MMS).  $f = 164.12 \text{ kHz}$ .

# Chapter 3

## High-speed boundary-layer instability: Old terminology and a new framework

This section is based on the paper published in collaboration with A. Fedorov in Refs. [FT11] and [FT10]

### 3.1 Introduction

In hydrodynamic stability analysis, the normal mode concept suggests considering simple wave-like solutions of the linearized Navier-Stokes equations in the form  $q'(x, y, t) = q(y) \exp(i\alpha x - i\omega t)$ , where  $q(y)$  is a complex amplitude function. This form assumes that the mean flow is parallel or quasi-parallel; i.e. the mean flow velocity and temperature profiles are functions of  $y$  only. The underlying idea of the normal mode concept is that instead of solving a specific physical initial boundary-value problem, we consider normal modes of the wave system, expecting that a solution of the initial boundary-value problem for the partial differential equations (PDE) can be presented as a sum of the normal modes. If there is an unstable mode, it is expected that this mode will be present in the solution of a specific physical problem (realized experimentally or solved numerically) and it can be dominant after sufficient amplification in space and/or time. Because the continuum medium has an infinite number of degrees of freedom, the disturbance field has a numerable discrete spectrum or a continuous spectrum, or a combination of both [CJJ67, Mik74].

In general, we may consider the wave number,  $\alpha = \alpha_r + i\alpha_i$ , and frequency,  $\omega = \omega_r + i\omega_i$ , as complex quantities. Very often two formulations are mentioned: temporal and spatial theories. In the temporal stability theory,  $\alpha_i = 0$  and  $\alpha_r$  is considered as a parameter, while  $\omega$  is the complex frequency determined from the dispersion relation  $\omega = \omega(\alpha, R, M, \dots)$ . According to the normal mode treatment, the solution depends on time as  $\exp(-i\omega t) = \exp(-i\omega_r t + \omega_i t)$ . It is unstable (grows exponentially with  $t$ ) if  $\omega_i > 0$ , stable if  $\omega_i < 0$ , and neutral if  $\omega_i = 0$ . In the spatial stability theory,  $\omega_i = 0$  and  $\omega_r$  is the real frequency considered as a parameter, while the complex wavenumber  $\alpha$  is determined from the dispersion relation  $\alpha = \alpha(\omega, R, M, \dots)$ . Now, the disturbance amplitude depends on the streamwise

coordinate as  $\exp(i\alpha x) = \exp(i\alpha_r x - \alpha_i x)$ . Propagating downstream, the disturbance grows exponentially with  $x$  if  $\alpha_i < 0$ , and decays if  $\alpha_i > 0$ .

One can find in the literature an ambiguity with the choice between temporal or spatial formulations of stability problems. The ambiguity has its origin at the step when partial solutions of PDE are suggested in the form of normal modes. At this point, the link with the initial boundary-value problem for a specific setup is lost, and we have an artificial dilemma of spatial versus temporal formulations.

Gustavsson [Gus79] solved an initial value problem for perturbations in the incompressible boundary layer. Salwen and Grosch [SG81] proved that Gustavsson solution is an expansion into the modes of discrete and continuous spectra of the temporal stability problem. The difference between the discrete spectrum and the continuous spectrum is their behavior outside the boundary layer ( $y \rightarrow \infty$ ). The discrete spectrum is required to vanish as  $y \rightarrow \infty$ , while the continuous part is only required to be bounded. Ashpis and Reshotko [AR90] considered the signaling problem when a periodic-in-time point source introduces perturbations through the wall starting at  $t = 0$ . They showed that the solution of this problem can be presented (after a sufficiently long time when the transient effect is smeared out) as an expansion into modes of the discrete and continuous spectra resulted from the spatial stability theory. Therefore, the analysis of a specific initial boundary-value problem for PDE leads to the unique expansion of a solution into the normal modes without any ambiguity. In compressible boundary layers, there are seven branches of continuous spectrum [TF83, BM92]: three branches correspond to waves propagating upstream with rapid decay, two branches correspond to slow and fast acoustic waves propagating downstream, and two branches correspond to vorticity and entropy waves propagating downstream.

Mack [Mac69] discovered new unstable modes of the discrete spectrum in high-speed boundary layers. He first considered the temporal stability problem for inviscid perturbations and computed the eigenvalue dependencies  $\omega(\alpha)$  for the flat-plate boundary layer at various free-stream parameters. In discussion of these dependencies, Mack used the terms modes and families. However, his usage of the term modes is inconsistent with the mathematical definition of modes as eigenfunctions that can be used for expansion of PDE solutions. Mack definition of families is what mathematicians would normally call modes. Moreover, Mack subdivided a family representing one dependency of  $\omega(\alpha)$  into different pieces giving them different labels of modes. To illustrate Mack terminology, we refer to Fig. 3.1 showing the phase speed diagram  $c_i(\alpha) = \omega_i(\alpha)/\alpha$  for the boundary layer on a thermally insulated (adiabatic) flat plate at the Mach number  $M = 3.8$ . One may compare Fig. 3.1 with Fig. 11.6a of [Mac69]. Note that because we conduct computations at constant Prandtl number,  $Pr = 0.72$ , and in some cases at different stagnation temperature, there are some differences between our results and the results of [Mac69]. Hereafter, dimensionless parameters are obtained using the Blasius length scale  $\sqrt{\nu_e^* x^* / U_e^*}$  (asterisk denotes a dimensional quantity). Following Mack notation, the wavenumbers  $\alpha_{sn}$  ( $n = 1, 2, \dots$ ) are associated with the generalized inflection point at which  $d((dU/dy)/T)/dy = 0$ , and the wavenumbers  $\alpha_{1n}$  ( $n = 1, 2, \dots$ ) are associated with regular neutral solutions.

Mack wrote (page 11-21, [Mac69]): The eigenvalues for  $c_i \neq 0$  lie on two separate curves

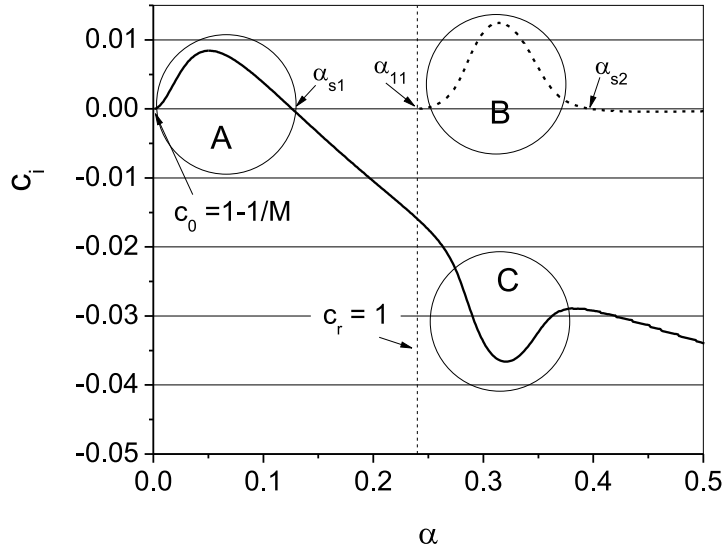


Figure 3.1: Eigenvalue diagram.  $M = 3.8$ ,  $T_0 = 300\text{K}$ ,  $\gamma = 1.4$ ,  $\text{Pr} = 0.72$ , adiabatic wall. Inviscid theory. Region A corresponds to first-mode amplified solutions. Region B corresponds to second-mode amplified solutions. Region C corresponds to second-mode damped solutions.

in Fig. 11.6 and form distinct families of solutions. One family starts at the neutral sonic solution; the other starts at the first-mode regular neutral solutions. It is easier to discuss the inviscid solutions in terms of these families rather than in terms of the modes. The mode identification changes along the eigenvalue curves, and is often not well defined. Further down the same page, Mack introduces his definitions: In Fig. 11.6 the solutions of the  $c_0$  family between  $(0, c_0)$  and  $(\alpha_{s1}, c_s)$  are amplified, and there is almost no phase change across the boundary layer in the pressure fluctuations. These solutions will be called first-mode amplified solutions. The solutions of the  $\alpha_{11}$  family between  $(\alpha_{11}, 1)$  and  $(\alpha_{s2}, c_s)$  are also amplified, but except near  $(\alpha_{11}, 1)$  there is a sizable phase change in the pressure fluctuations. These solutions will be called second-mode amplified solutions. In the next paragraph on the same page, Mack introduces a definition of the other part of the  $c_0$  family: It is of interest that there is a local maximum in the damping rate of the  $c_0$  family of solutions at almost the same wave number for which the amplification rate of the solution of the  $\alpha_{11}$  family is a maximum. Since the pressure-fluctuation phase change is large for the damped solutions near this wave number, those solutions will be called second-mode damped solutions. Thus, Mack uses two different mode labels for one family curve.

The spectrum structure becomes more complicated at higher Mach numbers. For example, Figure 3.2 shows  $c_i(\alpha)$  at  $M = 7$  (it is similar to Fig. 11.8a of [Mac69]). In connection with this, Mack wrote on page 11-23 of [Mac69]: As shown in Fig. 11.8a for  $M = 7$ , the  $c_0$  family of solutions no longer contains the first-mode neutral subsonic solution  $(\alpha_{s1}, c_s)$

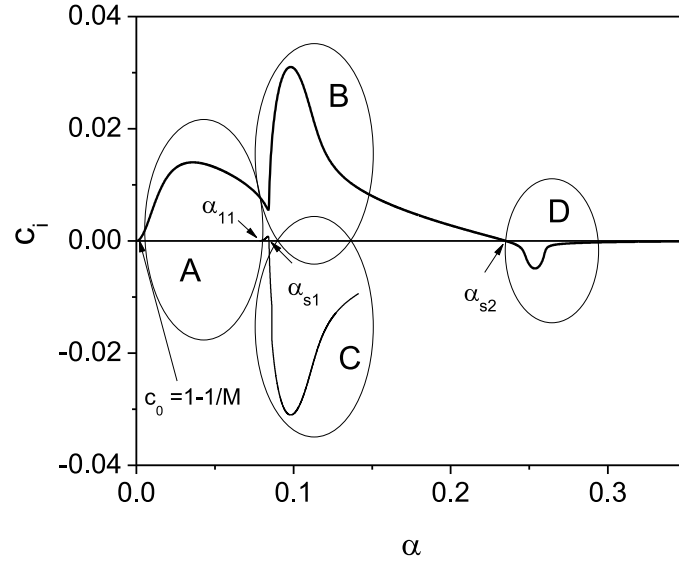


Figure 3.2: Eigenvalue diagram.  $M = 7$ ,  $T_0 = 540\text{K}$ ,  $\gamma = 1.4$ ,  $\text{Pr} = 0.72$ , and  $T_e = 50\text{K}$ . Region A corresponds to first-mode amplified solutions. Region B corresponds to second-mode amplified solutions. Region C corresponds to second-mode damped solutions. Region D corresponds to third-mode damped solutions.

and the second-mode damped solutions, but instead contains the second-mode amplified solutions, the second-mode neutral subsonic solution  $(\alpha_{s2}, c_s)$ , and the third-mode damped solutions. These examples illustrate that Mack definitions of modes are inconsistent with conventional usage of the term normal modes. In Figs. 3.1 and 3.2, two distinct normal modes correspond to the  $c_0$  and  $(\alpha_{11}, 1)$  families.

Mack then considered viscous perturbations and compared the dependencies of  $c(\alpha)$  at finite Reynolds numbers with the inviscid ones. For one of Macks choices of parameters, there were two separate inviscid amplification rate curves for the first and second modes ([Mac69], page. 12-24) (i.e., two inviscid normal modes), but only a single amplification rate curve at the finite Reynolds number shown (i.e., one viscous normal mode). This example illustrates that the spectrum structure can be drastically changed by the viscous effects.

Receptivity studies in 1980s-2000s, which are summarized in [Fed03, Tum06a], indicated that excitation of instabilities predominantly occurs upstream from the unstable region. This motivated Fedorov and Khokhlov [FK01] to investigate the disturbance spectrum in the region located upstream from the lower neutral branch. The spatial stability analysis [FK01] of 2D unstable modes in hypersonic flows revealed the following features (Fig. 3.3): (1) in the leading-edge region, two discrete modes (fast and slow) are synchronized with the fast and slow acoustic waves of the continuous spectrum, respectively; (2) further downstream, the fast discrete mode is synchronized with the entropy and vorticity waves of the continuous spectrum; (3) further downstream, the fast discrete mode is synchronized with the slow discrete mode. The latter synchronization leads to a branching of the discrete spectrum [GF, GF90]. As shown in [FK01], the normal mode decomposition is not valid in the branch-point vicinity and should be replaced by a local solution accounting for the coupling of discrete modes. Consequences of these findings for modeling of high-speed transition are recently discussed by Fedorov [Fed11].

The aforementioned shortcomings of Mack terminology motivated Fedorov [Fed03] to categorize the discrete modes using their asymptotic behavior near the leading edge. As shown in [FK01] for 2D disturbances, the phase speed of one mode tends to  $c = 1 - 1/M$  of slow acoustic wave, whereas the phase speed of the other tends to  $c = 1 + 1/M$  of fast acoustic wave. Fedorov [Fed03] called the former mode slow mode (mode S) and the latter fast mode (mode F). This terminology came to be used for the interpretation of DNS results [EFS06, TWZ07, WZ23, EFS08] on the receptivity and stability of high-speed boundary-layer flows.

The temporal stability analyses [FA03, FT05] revealed similar features of the spectral curves  $\omega(\alpha)$  at fixed Reynolds number  $R$ . Namely, the fast (or slow) mode is synchronized with the fast (or slow) acoustic wave in the long-wave limit  $\alpha \rightarrow 0$ . As  $\alpha$  increases, the fast mode is synchronized with the entropy/vorticity waves, and then it is synchronized with the slow mode that leads to branching of the discrete spectrum. The branching causes instability of what is called the second mode (according to Mack terminology). This similarity is not surprising because the spectrum behavior depends on the product  $\alpha^* \delta$ . The case of  $\alpha^* = \text{fixed}$  and  $\delta \rightarrow 0$  is treated as a leading-edge limit, while the case of  $\delta = \text{fixed}$  and  $\alpha^* \rightarrow 0$  is treated as a long-wave limit.

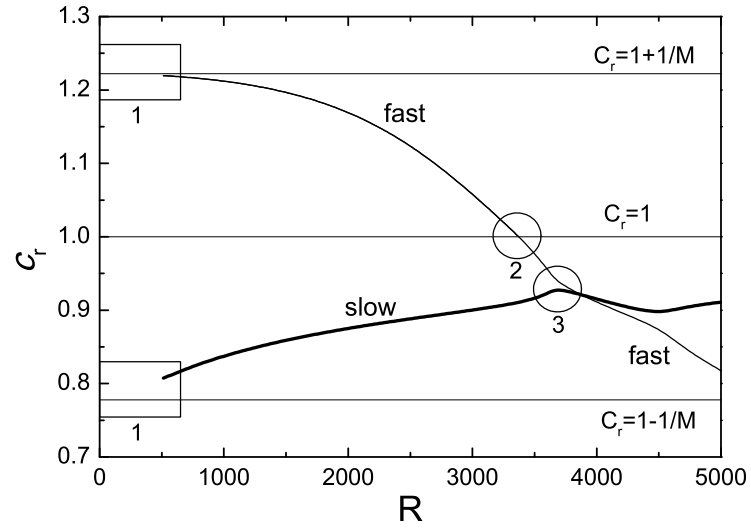
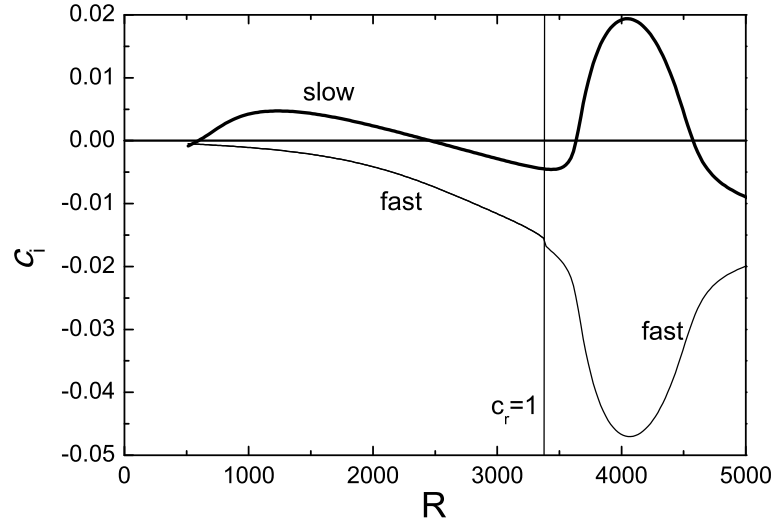


Figure 3.3: Imaginary and real parts of the phase speeds for slow and fast modes.  $M = 4.5$ ,  $T_w = T_{ad}$ ,  $F = 5 \times 10^{-5}$ , spatial stability analysis.

Mack [Mac69] introduced the viscous and inviscid families of solutions when the receptivity problem was not understood, and the decomposition of the solutions of the linearized Navier-Stokes equations had not been developed. A loose usage of the first mode and the second mode terminology has not been an obstacle in discussion of LST applications to transition prediction (e.g. using the  $e^N$ -method) even in the cases when only one unstable normal mode exists at finite Reynolds numbers. However, one has to be aware of the meaning of this imprecise terminology when transition prediction is based on consideration of the first and/or second mode. On the other hand, the usage of the mode F and mode S terminology has not yet been discussed properly in connection with the inviscid stability theory. In this paper, we consider the discrete spectrum of disturbances in high-speed boundary layers in order to clarify the contemporary terminologies and their interrelations. In addition, a model of discrete spectrum branching is outlined in order to explain different behaviors of the aforementioned discrete modes.

## 3.2 Discussion of discrete spectrum in high-speed boundary layers

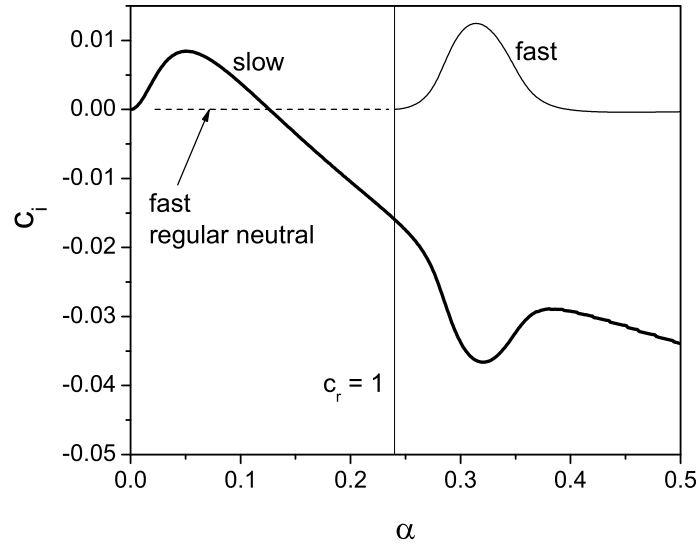
This section illustrates examples of discrete normal modes resulted from numerical solutions of the temporal and spatial stability problems for the locally parallel boundary-layer flow on a flat plate. All computations were conducted for perfect gas of constant Prandtl number  $Pr = 0.72$  and specific heat ratio  $\gamma = 1.4$ . Viscosity is calculated using the Sutherland law with a constant of 110.4K and the bulk viscosity is zero. The mean flow profiles correspond to the compressible Blasius solution; i.e., the viscos-inviscid interaction is neglected. The discrete spectrum structures for viscous (at finite Reynolds number) and inviscid ( $R \rightarrow \infty$ ) disturbances are compared.

### 3.2.1 Temporal stability theory

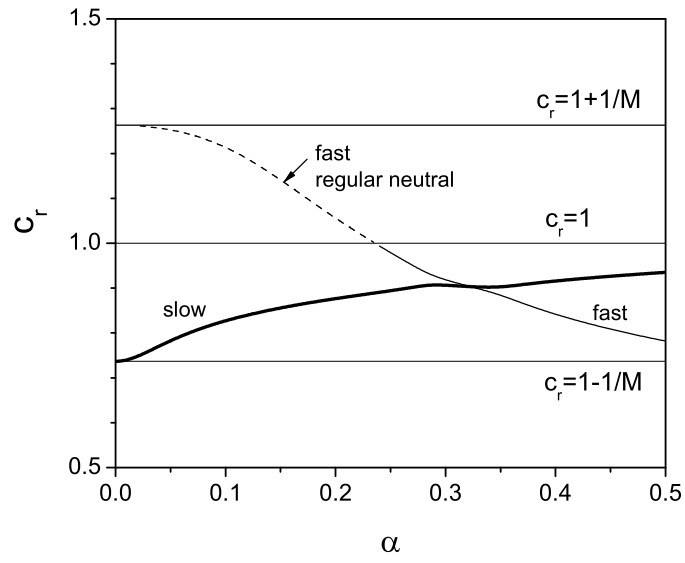
In order to show the link between discrete modes at finite and infinite Reynolds numbers, we have to consider the regular neutral modes. The inviscid stability equations have neutral ( $c_i = 0$ ) discrete solutions with the phase speed  $1 \leq c_r \leq 1 + 1/M$ . Figures 3.4a and 3.4b illustrate  $c_i(\alpha)$  and  $c_r(\alpha)$  for the boundary layer on an adiabatic flat plate at  $M = 3.8$  and  $R \rightarrow \infty$ , while figures 3.5a and 3.5b show  $c_i(\alpha)$  and  $c_r(\alpha)$  at finite  $R = 2000$ . In the viscous case, the fast discrete mode, which is synchronized with fast acoustic wave of  $c = 1 + 1/M$  as  $\alpha \rightarrow 0$ , has a small jump of  $c_i(\alpha)$  at the point where  $c_r = 1$ . Actually, we should treat the fast mode as two discrete modes. One of them has  $c_r > 1$  and coalescences with the continuous spectrum branch corresponding to vorticity and entropy waves ( $c_r \rightarrow 1 + 0$ ).

The other mode departs from this branch with  $c_r \rightarrow 1 - 0$  and has  $c_r < 1$ . The coalescence and departure occur at slightly different values of  $c_i$ . Because the jump of  $c_i$  is small, it is usually ignored in stability analyses. However, the eigenfunctions are substantially different on different sides of  $c_r = 1$ . Their outer asymptotic forms contain different eigenvectors, which are proportional to  $\exp(i\alpha x \pm i\lambda y - i\omega t)$  as  $c_r \rightarrow 1 \mp 0$  and  $y \rightarrow \infty$ . This difference



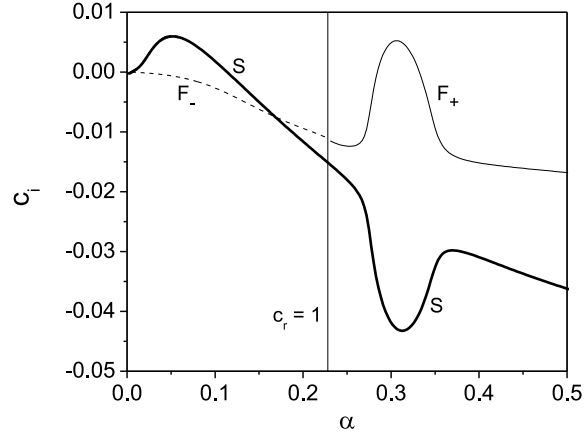


a)

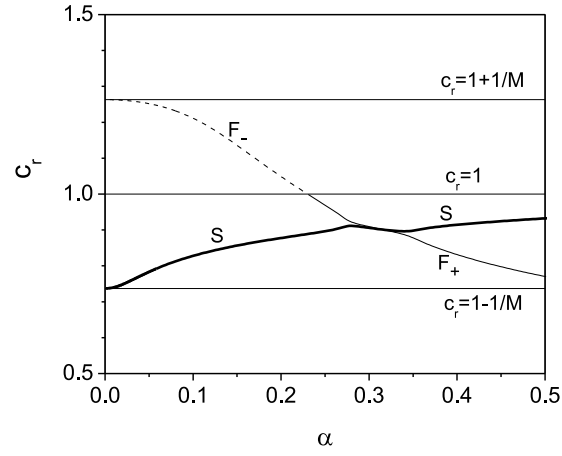


b)

Figure 3.4:  $c_i$  (a) and  $c_r$  (b) versus  $\alpha$ .  $M = 3.8$ ,  $T_0 = 300\text{K}$ . Inviscid theory.

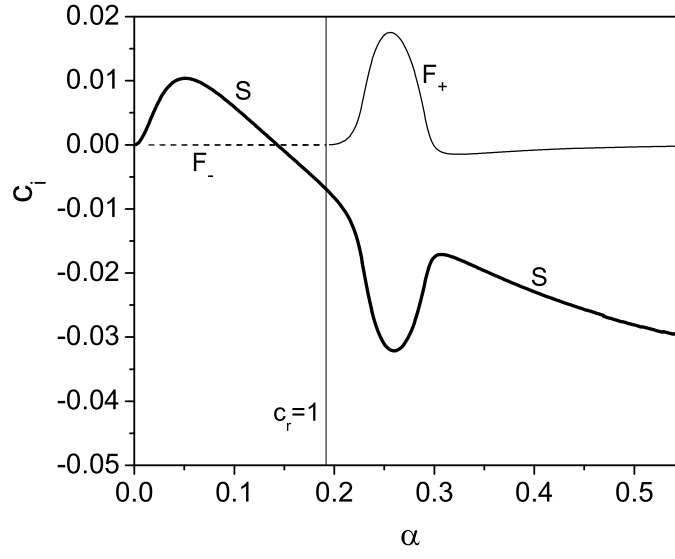


a)

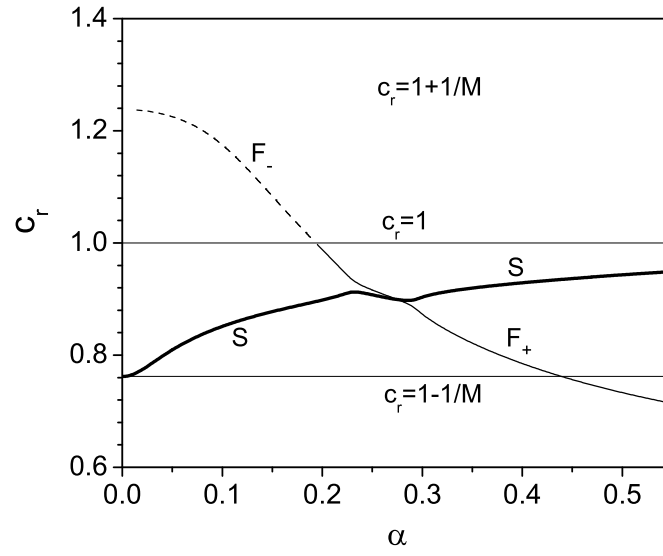


b)

Figure 3.5:  $c_i$  (a) and  $c_r$  (b) versus  $\alpha$ .  $M = 3.8$ ,  $T_0 = 300\text{K}$ ,  $R = 2000$ .

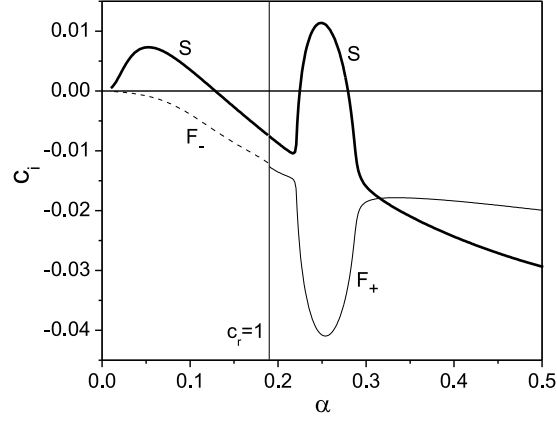


a)

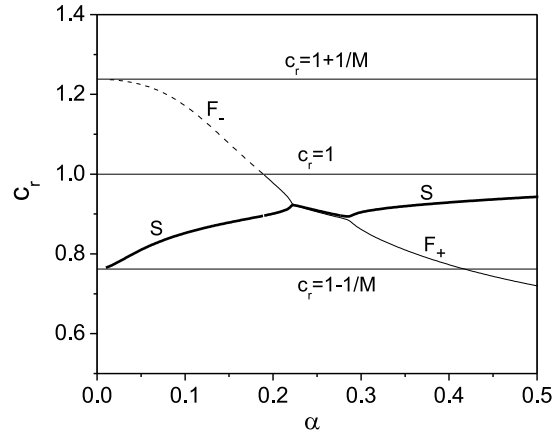


b)

Figure 3.6:  $c_i$  (a) and  $c_r$  (b) versus  $\alpha$ .  $M = 4.2$ ,  $T_0 = 300\text{K}$ . Inviscid theory.

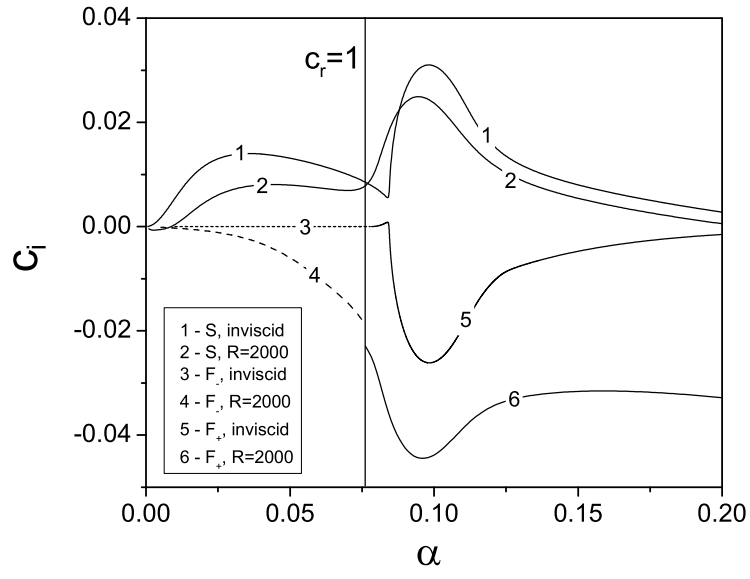


a)

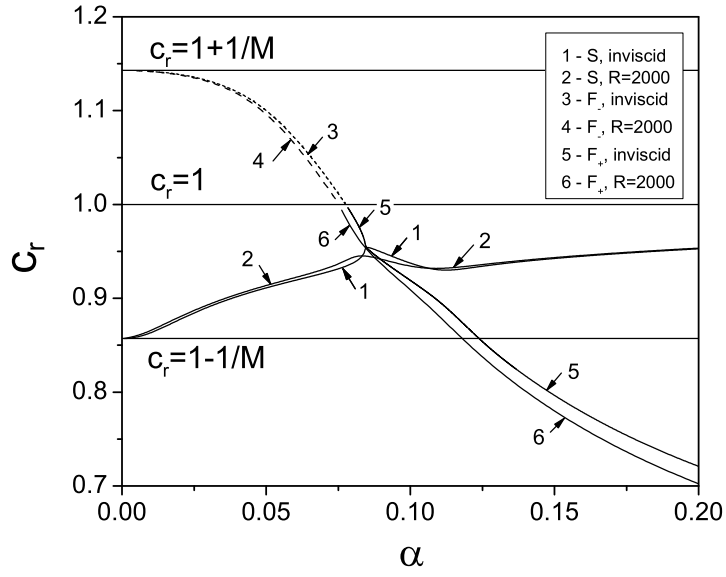


b)

Figure 3.7:  $c_i$  (a) and  $c_r$  (b) versus  $\alpha$ .  $M = 4.2$ ,  $T_0 = 300\text{K}$ ,  $R = 2000$ .



a)



b)

Figure 3.8:  $c_i$  (a) and  $c_r$  (b) versus  $\alpha$  in inviscid and viscous ( $R = 2000$ ) analyses,  $M = 7$ ,  $T_e = 50K$ .

is important for analysis of the initial value problem [FA03] describing receptivity to vorticity/entropy disturbances. Hereafter we call these modes as mode F- and mode F+. As shown in figure 3.5, mode F- is associated with the regular neutral solutions in the inviscid limit. Mode S, which is synchronized with the slow acoustic wave of phase speed  $c = 1 - 1/M$  as  $\alpha \rightarrow 0$ , corresponds to the inviscid slow mode shown in Figs. 3.4a and 3.4b. Mode F+ is unstable at the range of relatively large relevant to the second-mode instability. Mode S is unstable in the range of small relevant to the first-mode instability.

Figures 3.6a and 3.6b illustrate  $c_i(\alpha)$  and  $c_r(\alpha)$  for the boundary layer on an adiabatic flat plate at  $M = 4.2$  in the inviscid limit  $R \rightarrow \infty$ . The spectrum behavior is qualitatively the same as in the case of  $M = 3.8$  (Figs. 3.4a and 3.4b). However, it is drastically different at the finite Reynolds number  $R = 2000$  (Figs. 3.7a and 3.7b). Now, there is only one unstable mode (mode S) that has two maxima of  $c_i$  associated with the two unstable regions. This is similar to Mack observation in the cases of  $M = 5.8$  and  $M = 7$  ([Mac69], page 12-24). Comparing the cases shown in Figs 3.5a,b and Figs. 3.5a,b we conclude that increasing of Mach number from 3.8 to 4.2 (at fixed  $R = 2000$ ) leads to a qualitative change in the discrete spectrum pattern.

Figures 3.8a and 3.8b shows  $c_i$  and  $c_r$  versus  $\alpha$  for the inviscid and viscous cases at  $M = 7$ . Comparison of these data with that shown in Figs. 3.6a and 3.6b indicates that in the limit of  $R \rightarrow \infty$  the discrete spectrum pattern switches over to a different topology somewhere in the range  $4.2 < M < 7$ . This change is similar to that observed for viscous disturbances in the Mach number range from 3.8 to 4.2.

### 3.2.2 Spatial stability theory

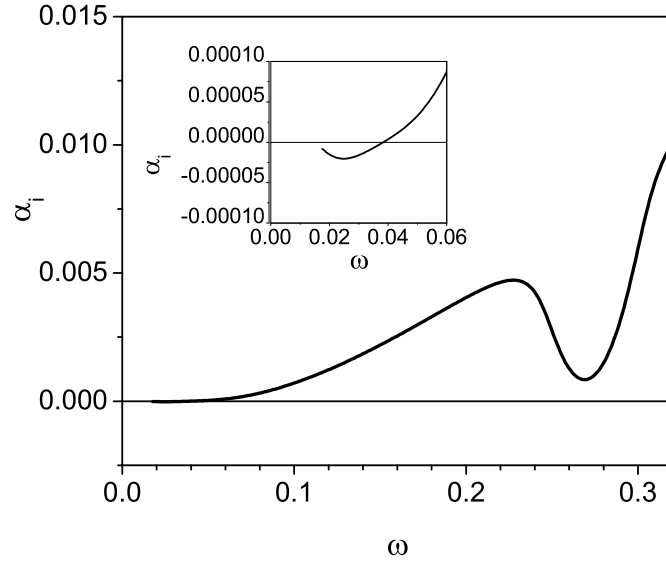
#### Adiabatic wall

In the case of an adiabatic wall in the spatial theory, available numerical results indicate that there is only one unstable mode (mode S). Figures 3.9a and 3.9b show  $\alpha_i$  versus frequency at  $M = 3.8$  and fixed Reynolds numbers. One can see that there are two minima in  $\alpha_i(\omega)$ . At  $R = 600$ , only the first minimum represents spatially unstable solutions. At  $R = 2000$ , unstable perturbations can be found in two bands of frequencies. Plotting the neutral curves in the  $\omega - R$  plane shows two unstable regions, but both of them are associated with mode S.

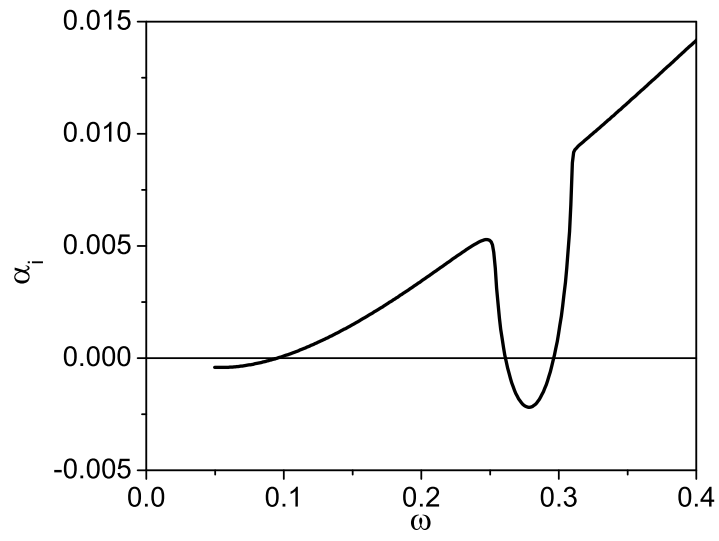
Another example is shown in Fig. 3.10 for the case of  $M = 4.2$  and  $R = 2000$ . Again, mode S is unstable in the low-frequency band relevant to the first-mode instability, and in the high-frequency band relevant to the second-mode instability.

#### Cold wall

It was shown in [FK01] that mode F+ can be unstable as well. In order to illustrate the spectral pattern, we consider perturbations at a fixed frequency parameter  $F = \omega^* \nu_e^* / U_e^{*2}$ . The dimensionless angular frequency is  $\omega = F \times R$ , the eigenvalues and phase speeds are expressed as  $\alpha = \alpha(R)$ ,  $c(R) = \omega / \alpha(R)$ .

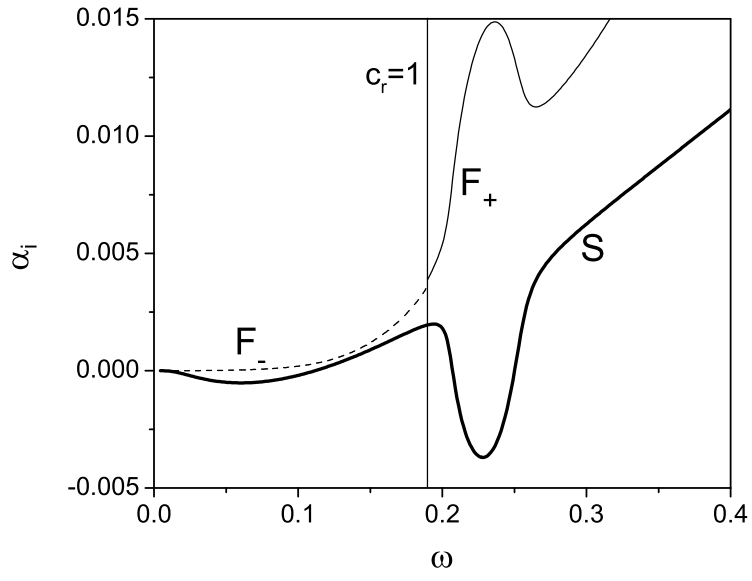


a)

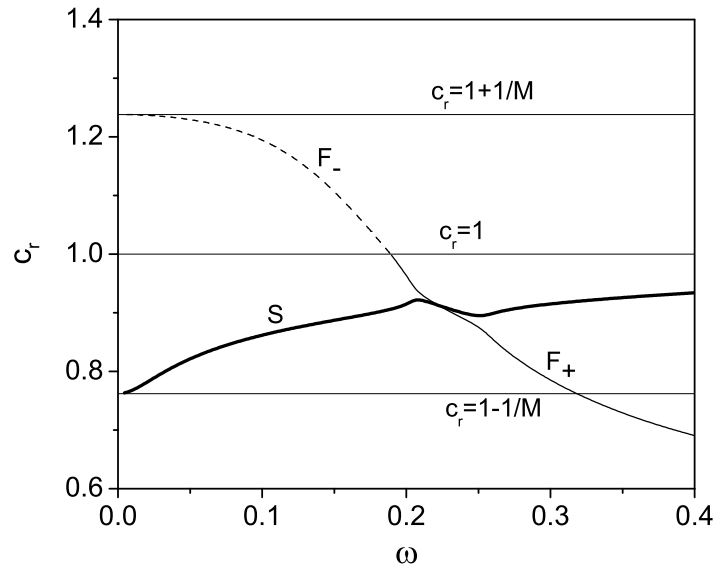


b)

Figure 3.9:  $\alpha_i$  versus  $\omega$  at  $R = 600$  (a) and  $R = 2000$  (b),  $M = 3.8$ . Adiabatic wall.



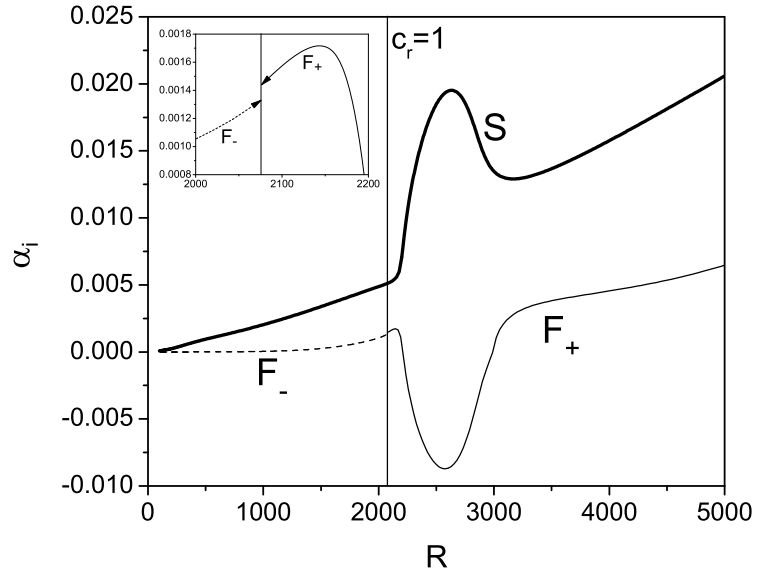
a)



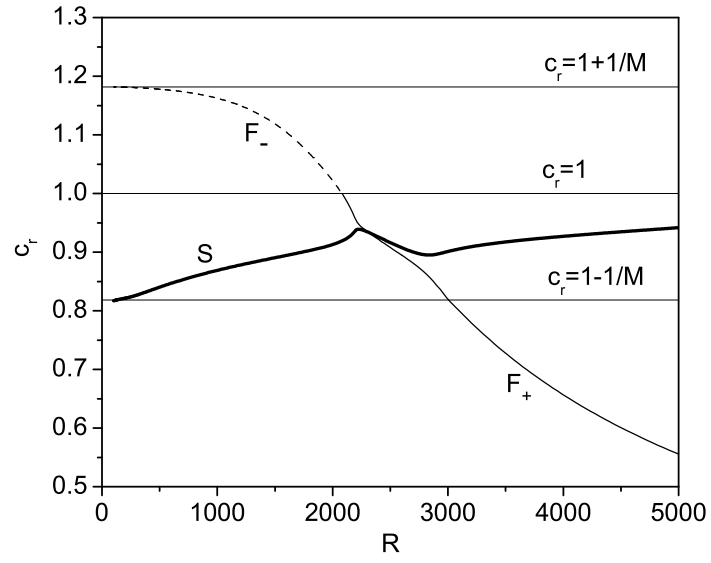
b)

Figure 3.10:  $\alpha_i$  (a) and  $c_r$  (b) versus  $\omega$ .  $M = 4.2$ ,  $T_0 = 300\text{K}$ ,  $R = 2000$ . Adiabatic wall.



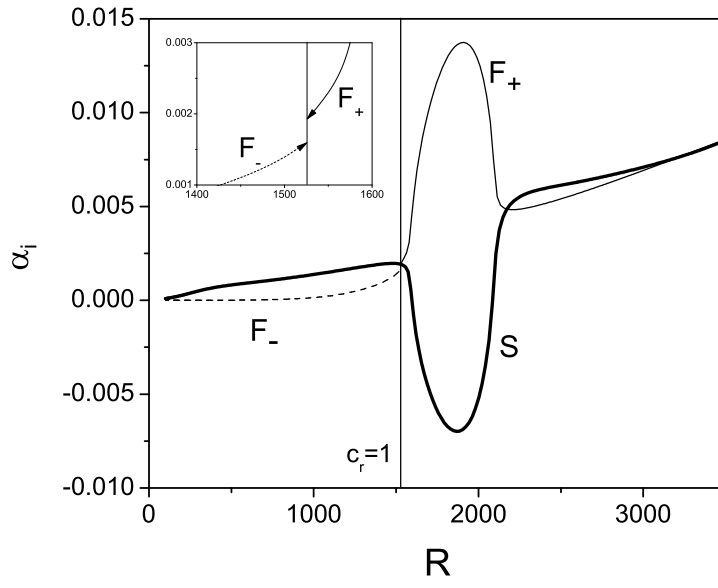


a)

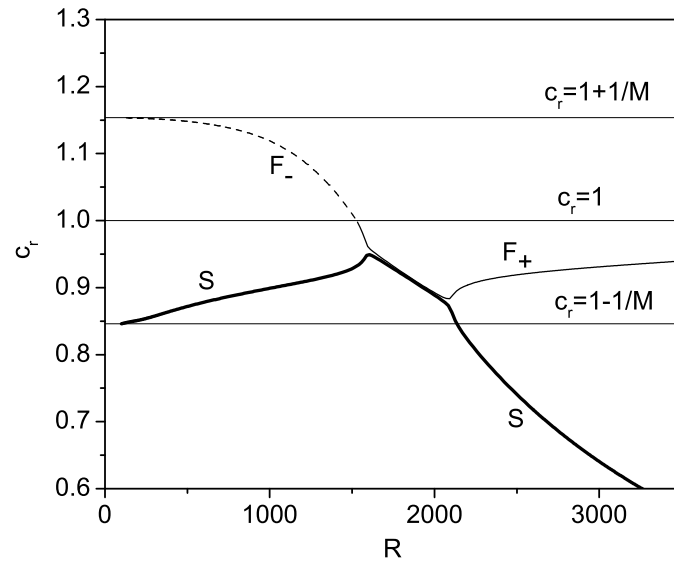


b)

Figure 3.11:  $\alpha_i$  (a) and  $c_r$  (b) versus  $R$ .  $M = 5.5$ ,  $T_e = 70\text{K}$ ,  $T_w/T_{ad} = 0.1$ ,  $F = 10^{-4}$ .



a)



b)

Figure 3.12:  $\alpha_i$  (a) and  $c_r$  (b) versus  $R$ .  $M = 6.5$ ,  $T_e = 70\text{K}$ ,  $T_w/T_{ad} = 0.1$ ,  $F = 10^{-4}$ .

Figures 3.11 and 3.12 show  $\alpha_i(R)$  and  $c_r(R)$  of modes S, F- and F+ for the boundary-layer flow at  $M = 5.5$  and  $M = 6.5$ , respectively. In the both cases, the mean-flow temperature at the upper boundary-layer edge is  $T_e^* = 70\text{K}$ , the wall temperature is  $T_w = 0.1T_{ad}$ , and the frequency parameter is  $F = 10^{-4}$ . Similar to the temporal stability cases discussed in Section A, mode F- (or mode S) is synchronized with the fast (or slow) acoustic wave in the leading-edge region corresponding to the long-wave limit. Then mode F- is synchronized with vorticity/entropy waves of the continuous spectrum at the station where  $c_r = 1$ . As the fast-mode eigenvalue crosses the vorticity/entropy branch, its imaginary part jumps by a small value  $\Delta\alpha_i$ . Further downstream mode F+ is synchronized with mode S and the dispersion curves branch out.

In the case of  $M = 5.5$  (Figs. 3.11a and 3.11b), the branching leads to destabilization of mode F+ and stabilization of mode S in the range of relevant to instability of Mack second mode. As contrasted to the adiabatic wall cases, there is no instability of the slow mode at relatively small because this instability (associated with Mack first mode) is suppressed by the wall cooling. In the case of  $M = 6.5$  (Figs. 3.12a and 3.12b), the branching is qualitatively different. Now mode S is unstable and mode F+ is stable. Detailed computations showed that the switching from one topology to the other occurs at  $M \approx 6$ .

### 3.3 A model of the discrete spectrum branching

Guschin and Fedorov [GF, GF90] have realized that the aforesaid branching of discrete spectrum is similar to the branching of weakly coupled waves that is typical for wave systems in the physics of plasmas Fedorchenko (see also 64 of [LP81]). Herein we outline an analytical model describing this branching.

Consider the temporal spectrum  $\omega(\alpha)$  and assume that the eigenvalues  $\omega_1(\alpha)$  and  $\omega_2(\alpha)$  (in our case, they are relevant to modes F+ and S) are synchronized in the vicinity of a certain point  $\alpha_0$ :  $\omega_1(\alpha_0) \approx \omega_2(\alpha_0) \approx \omega_0$ . The other modes of the discrete and continuous spectra are assumed to be sufficiently far from the synchronization region. Then, the dispersion relation in the vicinity of  $(\alpha_0, \omega_0)$  can be approximated as

$$(\bar{\omega} - a_1\bar{\alpha})(\bar{\omega} - a_2\bar{\alpha}) = \varepsilon_t, \quad (3.1)$$

where  $\bar{\omega} = \omega - \omega_0$  and  $\bar{\alpha} = \alpha - \alpha_0$  are local variables,  $\varepsilon_t$  is a small parameter characterizing weak coupling between the modes, and  $a_1 > a_2 > 0$  are the group velocities of the decoupled modes (at  $\varepsilon_t = 0$ ) schematically shown in Fig. 3.13. The dispersion curves branch out in the vicinity of the synchronization point as

$$\bar{\omega}_{1,2} = \frac{a_1 + a_2}{2}\bar{\alpha} \pm \sqrt{\frac{1}{4}\bar{\alpha}^2(a_1 - a_2)^2 + \varepsilon_t}. \quad (3.2)$$

The branching pattern depends on the locations of the branch points  $\bar{\alpha}_{br1,2} = \mp 2\sqrt{-\varepsilon_t}/(a_1 - a_2)$  in the complex  $\alpha$ -plane. If  $\varepsilon_t > 0$ , then  $\bar{\alpha}_{br1,2}$  are pure imaginary and the dispersion curves branch out as shown schematically in Fig. 3.14. In this case, the coupling does not cause

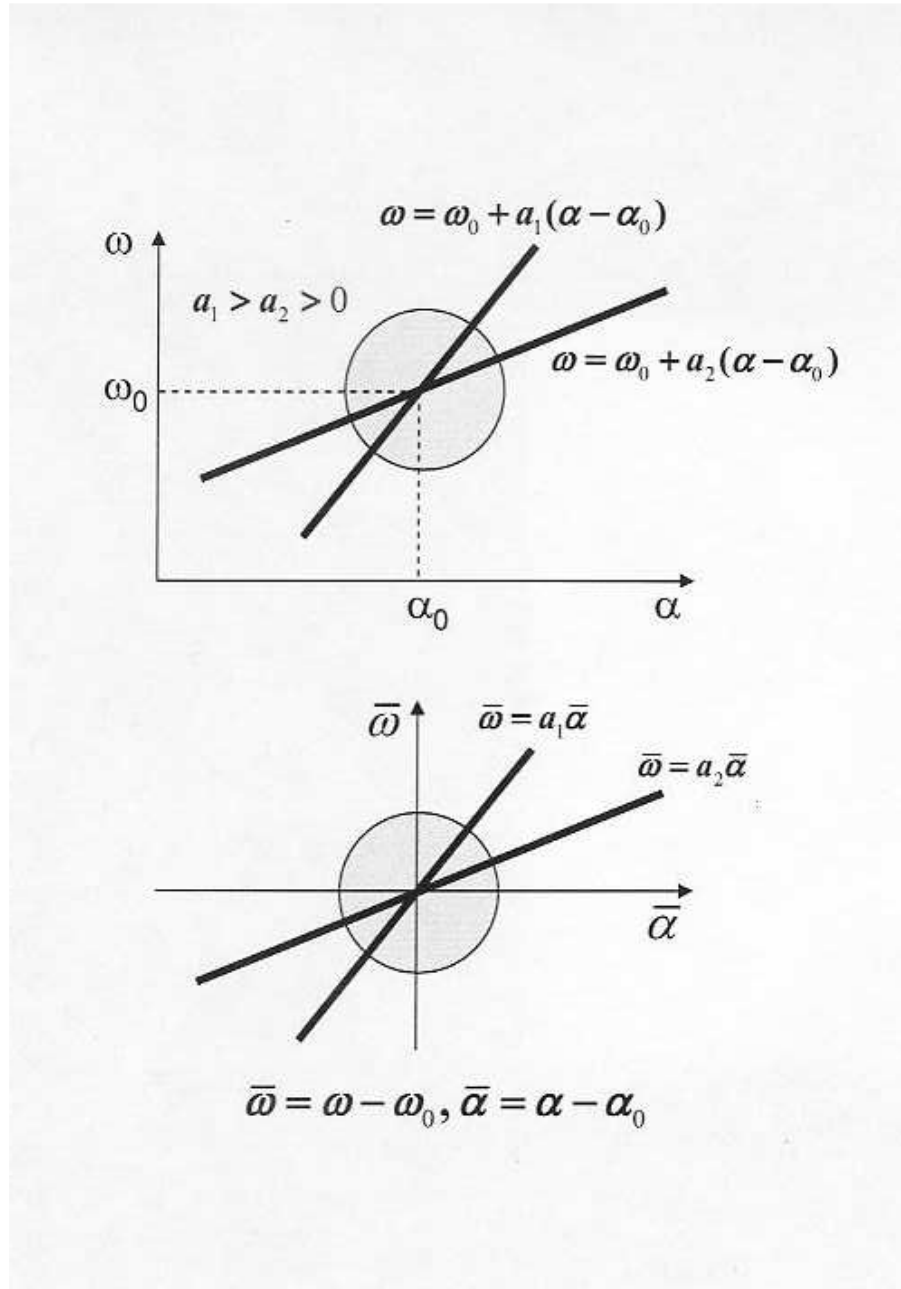


Figure 3.13: Synchronization of two uncoupled modes in the vicinity of  $(\alpha_0, \omega_0)$ .

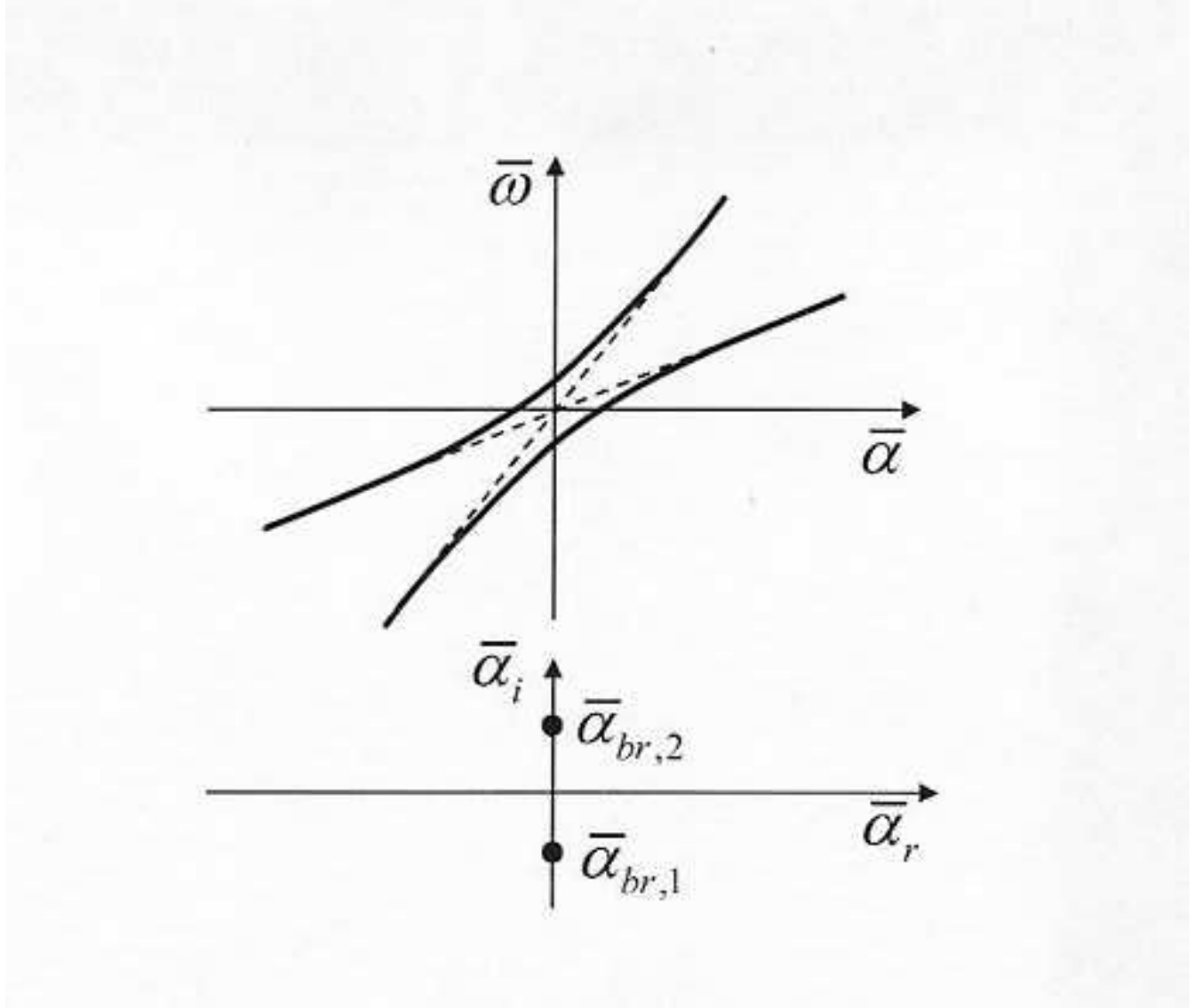


Figure 3.14: Neutral branching at  $\varepsilon_t > 0$ .

instability. If  $\varepsilon_t < 0$ , the branch points are real while  $\bar{\omega}_{1,2}$  are complex values in the range  $\bar{\alpha}_{br1} < \bar{\alpha} < \bar{\alpha}_{br2}$ . In this case, one mode becomes stable and the other unstable. Depending on bypasses of the branch points, there are four patterns of dispersion curves as shown schematically in Fig. 3.15.

For the temporal spectra of the boundary-layer flow discussed in Section IIA, the branching of modes  $F_+$  and  $S$  is topologically identical with one of the patterns shown in Fig. 3.15. The branch points were determined numerically from the condition  $|\partial\omega/\partial\alpha|^{-1} = 0$ . Computations showed that  $\alpha_{br1,2}$  are slightly shifted from the real axis to the lower or upper half-plane of complex  $\alpha$  depending on the basic flow parameters. As one marches along real  $\alpha$ , the branch points are bypassed from above or below, leading to a particular branching pattern.

The branch points move in the  $\alpha$ -plane with variations of the flow parameters, say the Mach number. As soon as  $\alpha_{br}$  crosses the real axis, the branching pattern switches over from one to another. For example, Figure 3.16 shows such switching from the branching A to the branching B due to a slight increase of Mach number from 4 to 4.2.

By computing the trajectories of the branch points and determining the parameters at which  $\alpha_{br1,2}$  crosses the real axis one can identify domains relevant to different branching patterns. As an example, Figure 3.17 shows the boundary between the branching A and the branching B in the Mach number-wall temperature plane. Below this boundary (at the relatively cold wall condition) there are two unstable modes: mode  $S$  is unstable in the range of small  $\alpha$  and mode  $F_+$  is unstable in the range of large  $\alpha$ . Above this boundary, there is only one unstable mode—the slow mode.

Similar analysis can be conducted for the spatial stability problem [FK01]. The dispersion relation is analytically continued to the complex plane of  $\bar{\alpha}$ . In the vicinity of synchronization point  $(R_0, \alpha_0)$ , Equation (1) is written in the form

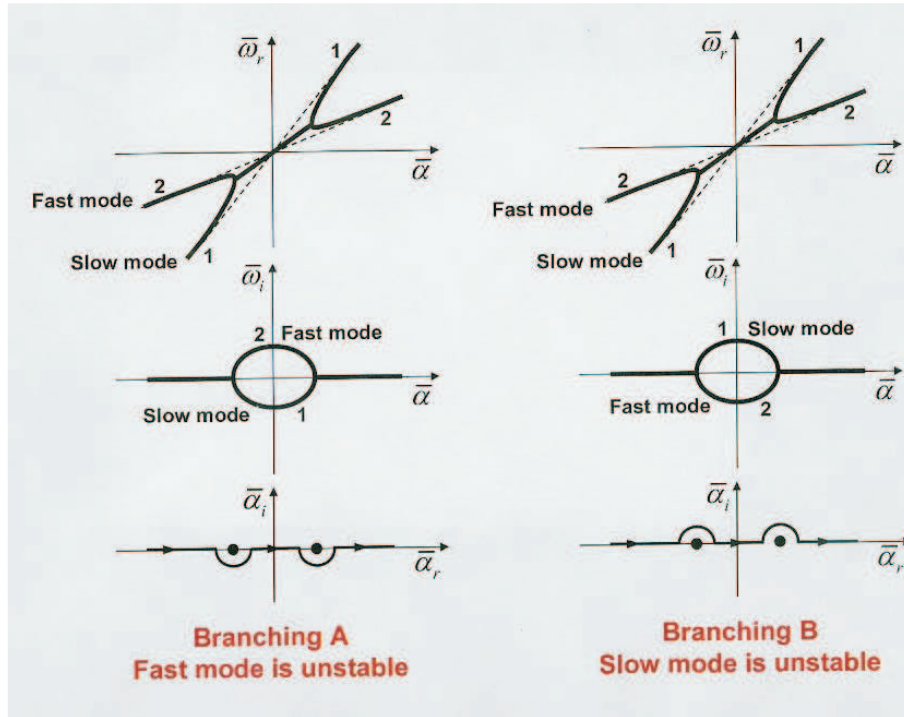
$$(\bar{\alpha} - b_1\bar{\omega})(\bar{\alpha} - b_2\bar{\omega}) = \varepsilon_s, \quad (3.3)$$

where  $\bar{\alpha} = \alpha - \alpha_0$ ,  $\bar{\omega} = F(R - R_0) = F\bar{R}$ ,  $b_1 = a_2^{-1}$  and  $b_2 = a_1^{-1}$  are constants,  $b_1 > b_2 > 0$ , a small parameter  $\varepsilon_s = \varepsilon_t/(a_1a_2)$  characterizes the coupling between synchronized modes. The solution has two branches

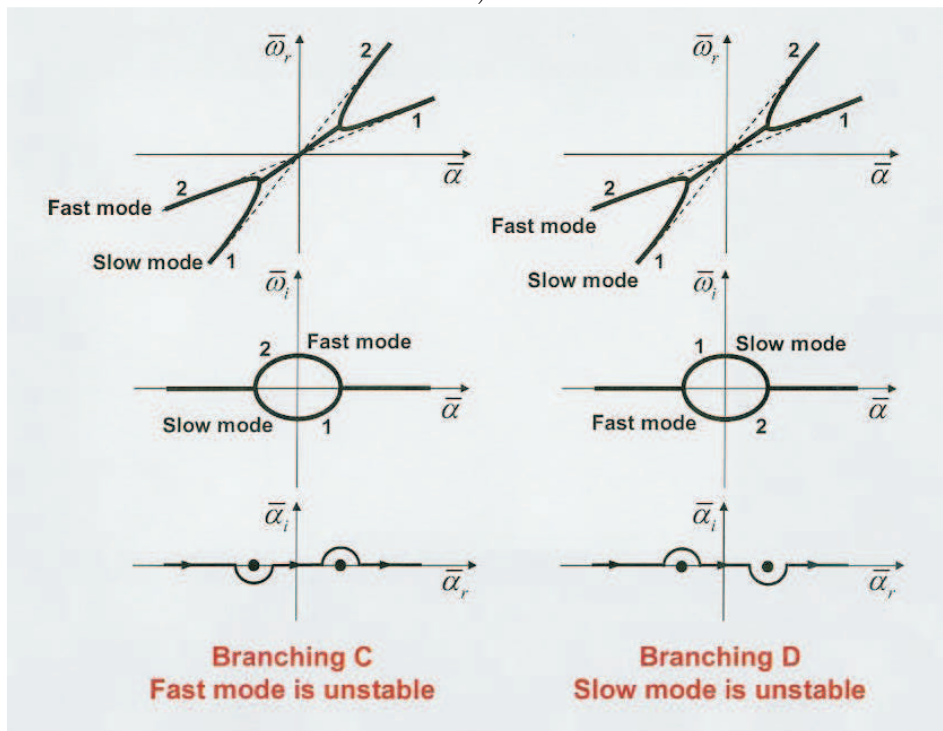
$$\bar{\alpha}_{1,2} = \frac{b_1 + b_2}{2}F\bar{R} \mp \sqrt{\frac{1}{4}(b_1 - b_2)^2F^2\bar{R}^2 + \varepsilon_s}. \quad (3.4)$$

The branch points  $\bar{R}_{br1,2} = \mp 2\sqrt{\varepsilon_s}/[F(b_1 - b_2)]$  are located in different half-planes of complex  $R$  depending on the basic flow parameters. With marching downstream along real  $R$ , the branch points are bypassed from above or below that leads to different branching patterns of  $\alpha(R)$ . For instance, in the case of  $M = 5.5$  (Fig. 3.11), the both branch points lie below the real axis of complex  $R$ -plane that gives the branching B shown in Fig. 3.15. In the case of  $M = 6.5$  (Fig. 3.12), the first branch point is above the real axis while the second is below. This gives the branching D.

Thus, the analytical model of weakly coupled synchronized modes helps to interpret intricate behaviors of disturbance spectrums that are observed in high-speed boundary layer

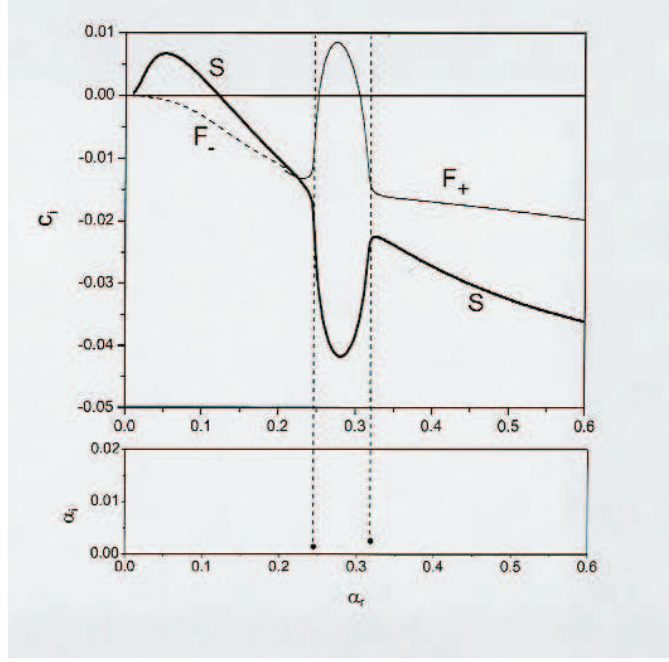


a)

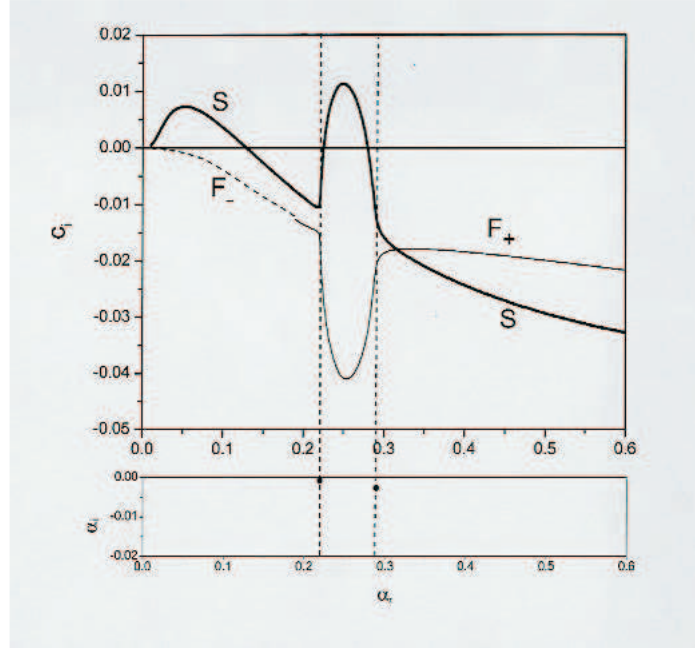


b)

Figure 3.15: Branching patterns for two weakly coupled modes.



a)



b)

Figure 3.16: Different branching patterns at small variation of Mach number at  $T_0 = 300\text{K}$ ,  $R = 2000$ . Branch points are shown by black circles in the complex  $\alpha$ -plane. (a)  $M = 4$ , branch points are bypassed from below – branching A, (b)  $M = 4.2$ , branch points are bypassed above – branching B.



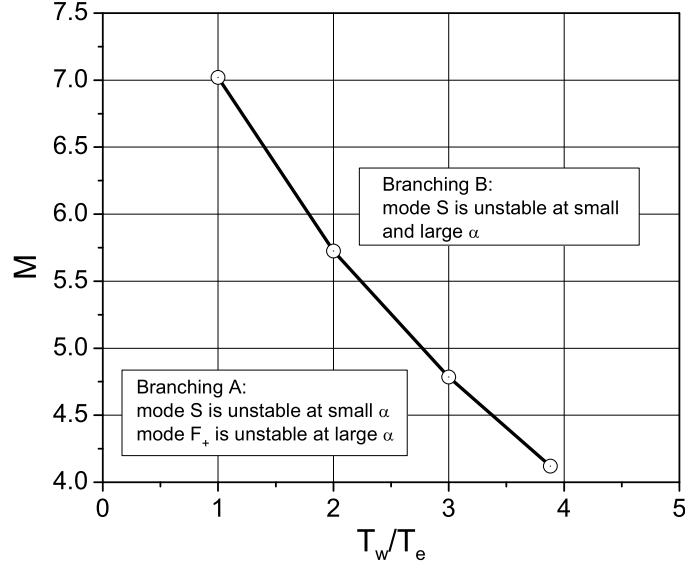
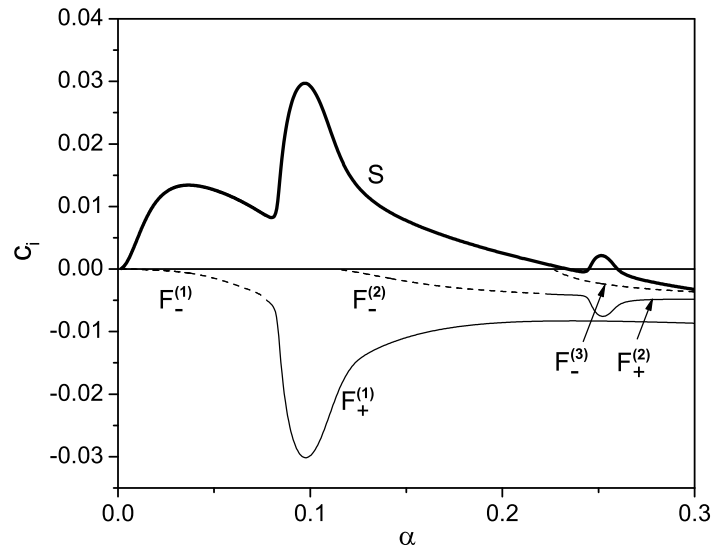


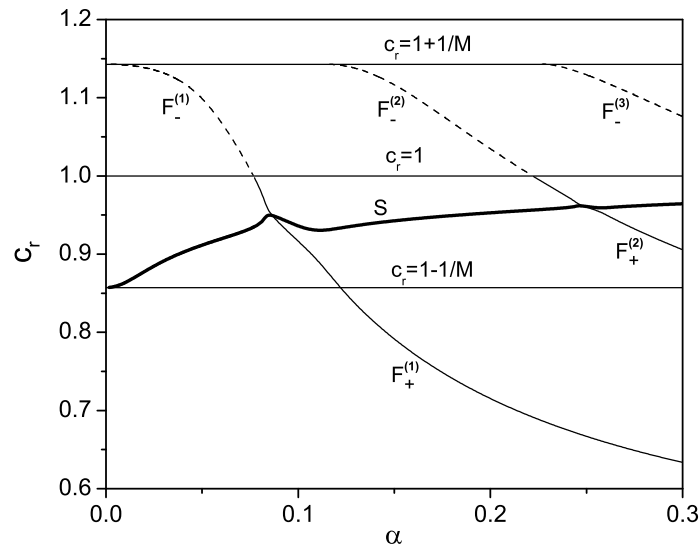
Figure 3.17:  $\alpha_i$  (a) and  $c_r$  (b) versus  $R$ .  $M = 6.5$ ,  $T_e = 70\text{K}$ ,  $T_w/T_{ad} = 0.1$ ,  $F = 10^{-4}$ .

flows. This model clearly shows that the second-mode instability is due to synchronization of modes S and  $F_+$ . Similar mechanism is responsible for the third- and higher-mode instabilities in hypersonic boundary layers [GF90], as well as short-wave instabilities in a thin shock layer [GF89]. As an example, figures 3.18 and 3.19 show the discrete spectrum at  $M = 7$ ,  $T_e = 50\text{ K}$  and  $R = 20000$  in the case of adiabatic wall ( $T_w = T_{ad}$ ) and cold wall ( $T_w = 1.2T_e$ ), respectively. In both cases, there are fast modes  $F_{\pm}^{(1)}$ ,  $F_{\pm}^{(2)}$ , ..., and the slow mode S. On an adiabatic wall, the Mack's second, third etc. instabilities correspond to mode S. These instabilities are associated with the branching B between modes  $F_+^{(k)}$  and mode S. In the cold-wall case, the Mack's second, third etc. instabilities correspond to modes  $F_+^{(1)}$ ,  $F_+^{(2)}$  etc. These instabilities are associated with the branching A. As the number  $k$  of mode  $F_+^{(k)}$  increases, the growth rates quickly decreases. E.g. the mode  $F_+^{(3)}$  in figure 3.19a is almost neutral. Ma and Zhong [MZ03a, MZ03b] showed that the fast modes  $F_-^{(1)}$ ,  $F_-^{(2)}$  etc. (named mode I, II, etc in [MZ03b]) are effectively excited by fast acoustic waves.

Fedorov and Khokhlov [FK01] showed that the normal mode decomposition is not valid near the branch point of discrete spectrum. Using asymptotic methods they obtained a local solution providing coupling between input and output amplitudes of the branching modes. It turned out that this coupling is governed by the intermodal exchange rule, which, in the leading-order approximation, does not depend on the mean-flow profiles. However, this result may be not valid when the branch point is too close to the branch cut of continuous spectrum. E.g. figure 3.16 shows that the relative distance between the first branch point  $\alpha_{b1} = 0.2199 - i0.00075$  and the vorticity/entropy branch cut is  $\Delta\alpha/\alpha \approx 5\%$ . In this case the vorticity/entropy waves may significantly affect the intermodal exchange. This issue

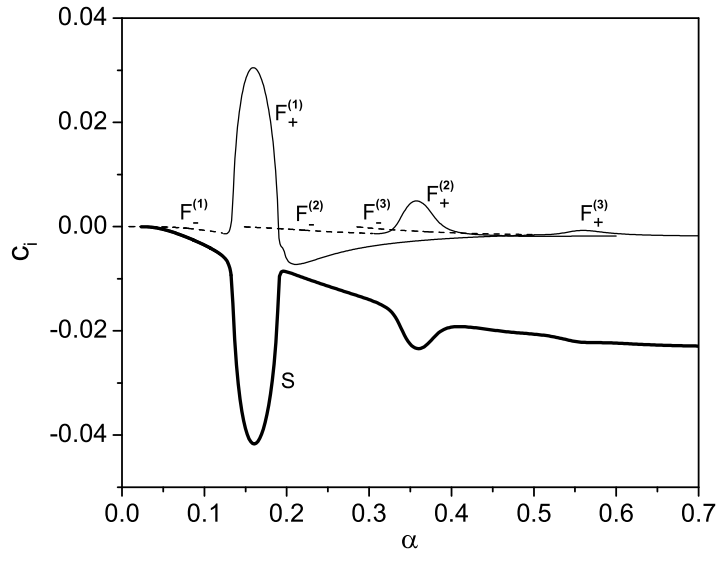


a)

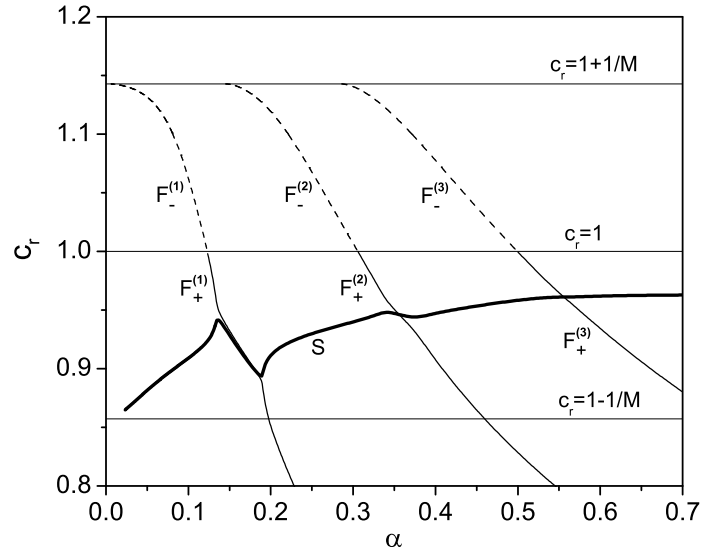


b)

Figure 3.18:  $c_i$  (a) and  $c_r$  (b) versus  $\alpha$ .  $M = 7$ ,  $T_e = 50\text{K}$ ,  $R = 2000$ . Adiabatic wall.



a)



b)

Figure 3.19:  $c_i$  (a) and  $c_r$  (b) versus  $\alpha$ .  $M = 7$ ,  $T_e = 50\text{K}$ ,  $R = 2000$ . Cold wall,  $T_w = 1.2T_e$ .

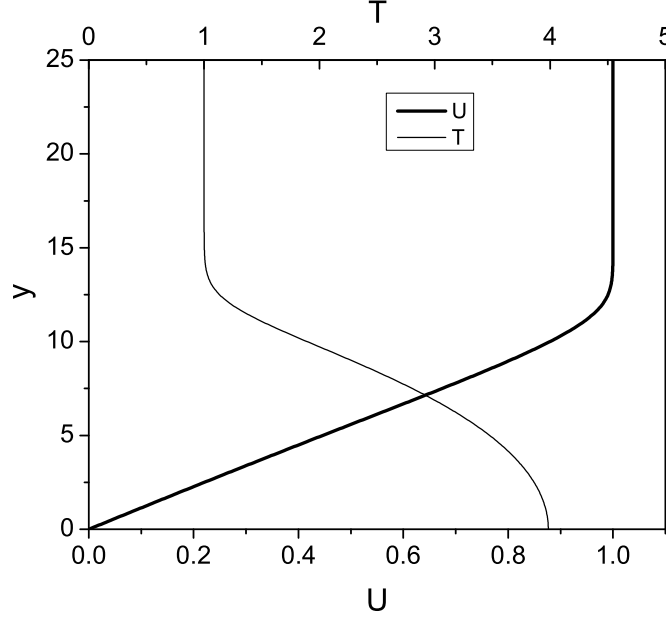


Figure 3.20: Mean-flow profiles at  $M = 4.2$ ,  $T_0 = 300\text{K}$  and  $T_w = T_{ad}$ .

should be clarified by further theoretical studies.

### 3.4 Eigenfunctions of slow and fast modes

Now we consider the eigenfunctions of the slow and fast modes for the boundary-layer flow at  $M = 4.2$ ,  $R = 2000$  and  $T_w = T_{ad}$  (see Figs. 3.7a,b). In all cases discussed herein, the eigenfunctions are normalized to the absolute value of the pressure amplitude on the wall. Perturbations of pressure  $p$ , streamwise velocity  $u$  and temperature  $\theta$  are made nondimensional using  $\rho_e^* U_e^{*2}$ ,  $U_e^*$  and  $T_e^*$ , respectively. Figure 3.20 shows the mean-flow profiles  $U(y)$  and  $T(y)$ , where the boundary-layer thickness is  $\delta = 12.5$  ( $U(\delta) = 0.99$ ) and the displacement thickness is  $\delta_1 = 9.34$ .

At  $\alpha = 0.05$  relevant to the first instability maximum, the eigenfunction of mode  $F_-$  typifies regular disturbances of the phase speed  $c_r > 1$  (thin lines in Fig. 3.21). The slow mode (thick lines) of  $c_r = 0.81$  has the critical layer in the vicinity of  $y_c \approx 10$ . Here the -velocity distribution has a phase jump and the temperature amplitude  $|\theta|$  has a strong maximum. The pressure amplitude  $|p|$  is almost constant across the boundary layer as typical for long-wave disturbances. Near the wall ( $0 < y < 1.2$ ) there is a well distinguished viscous sublayer (Stokes layer) for both fast and slow modes.

Figure 3.22 shows eigenfunctions of modes  $F_-$  and  $F_+$ , which are synchronized with the entropy and vorticity waves at  $c_r \rightarrow 1 \pm 0$ . These functions are almost identical inside the boundary layer, while the tails for the  $u$ -velocity and temperature are essentially different outside the boundary layer. This clearly shows that mode  $F_-$  with  $c_r > 1$  and mode  $F_+$  with

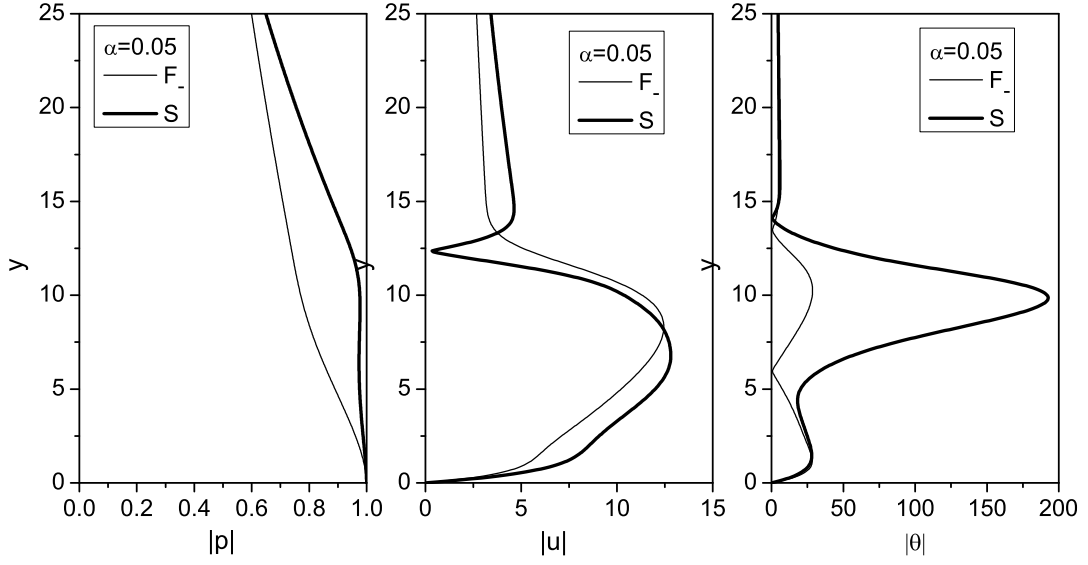


Figure 3.21: Eigenfunctions of the fast and slow modes at  $\alpha = 0.05$ ,  $M = 4.2$ ,  $T_0 = 300\text{K}$ ,  $T_w = T_{ad}$ ,  $R = 2000$ .

$c_r < 1$  are different normal modes of the discrete spectrum. The oscillatory behavior of the outer tails is due to synchronization of the discrete modes with the entropy and vorticity waves, which oscillate in the outer flow. A detailed discussion of these spectrum features is given in [FA03].

Figure 3.23 shows eigenfunctions of modes  $S$  and  $F_+$  in the vicinity of the first branch point  $\alpha_{br1} = 0.2199 - i0.00075$  (see Branching B in Fig. 3.16). As expected, in this region both modes have similar distributions across the boundary layer. However, there are quantitative differences because the eigenfunctions were computed at  $\alpha = 0.219$  which is slightly shifted from the branch point.

Figure 3.24 illustrates eigenfunctions at  $\alpha = 0.25$  relevant to the second maximum of instability (see Fig. 3.7a). This point lies approximately in the middle of the branching region  $\alpha_{br1} < \alpha < \alpha_{br2}$ , where the coupling between modes  $F_+$  and  $S$  produces the most profound effect on the growth rates. Since the real frequencies of these modes are practically identical, their eigenfunctions are very close everywhere besides the critical layer, which is formed at the distance  $y_c \approx 10$ .

The foregoing examples show that the eigenfunctions of fast and slow modes are quite sensitive to singularities of the dispersion relation caused by spectrum branching and by coalescence with the continuous spectrum. This may significantly affect receptivity as well as the nonlinear interaction between the modes.

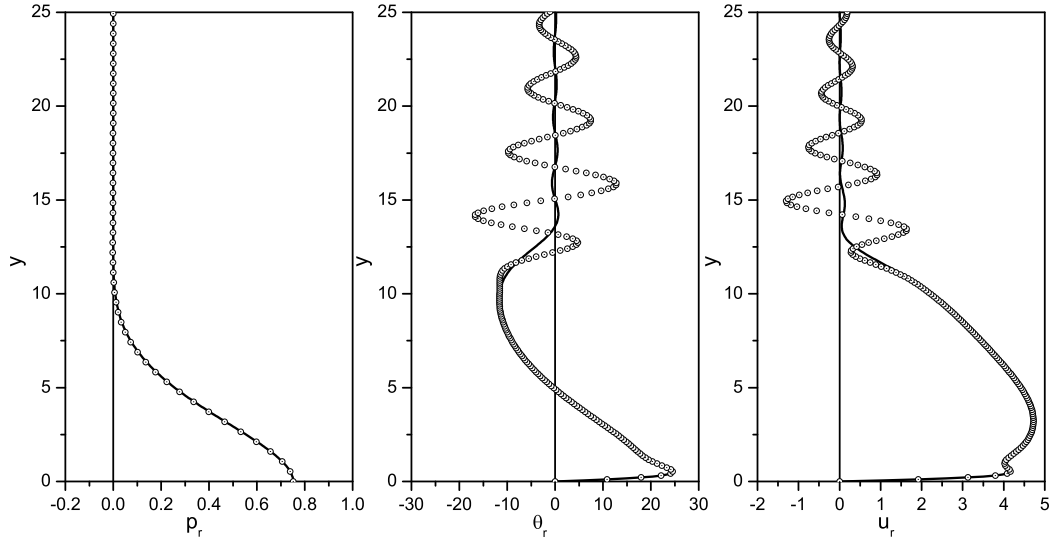


Figure 3.22: Eigenfunctions of fast modes in the vicinity of vorticity and entropy waves,  $M = 4.2$ ,  $T_0 = 300\text{K}$ ,  $T_w = T_{ad}$ ,  $R = 2000$ . Symbols – mode  $F_+$  at  $\alpha = 0.1899$ ,  $c_r \rightarrow 1 - 0$ ; black lines – mode  $F_-$  at  $\alpha = 0.1886$ ,  $c_r \rightarrow 1 + 0$ .

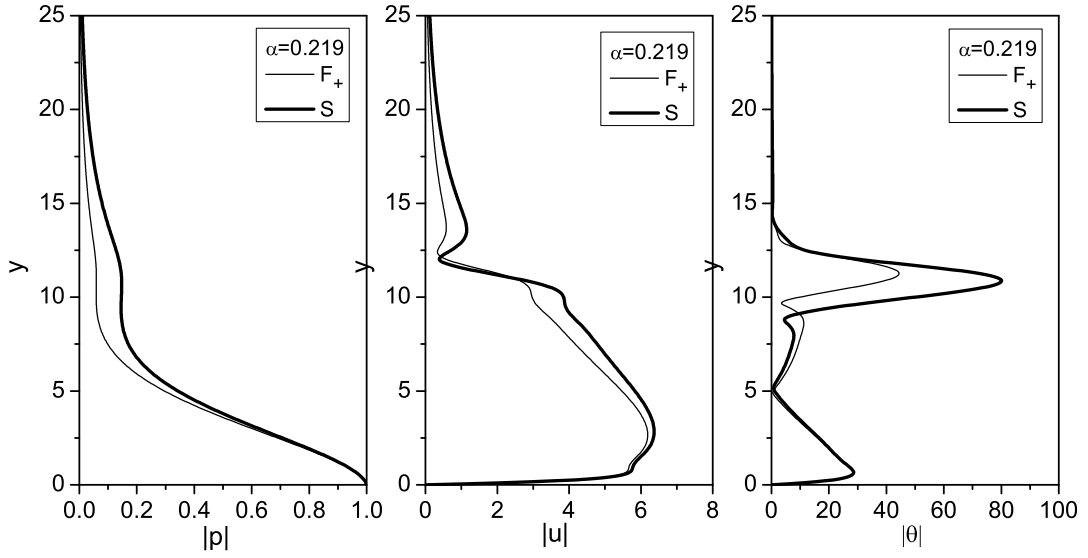


Figure 3.23: Eigenfunctions of modes  $F_+$  and  $S$  in the vicinity of the first branch point,  $M = 4.2$ ,  $T_0 = 300\text{K}$ ,  $T_w = T_{ad}$ ,  $R = 2000$ ,  $\alpha = 0.219$ .

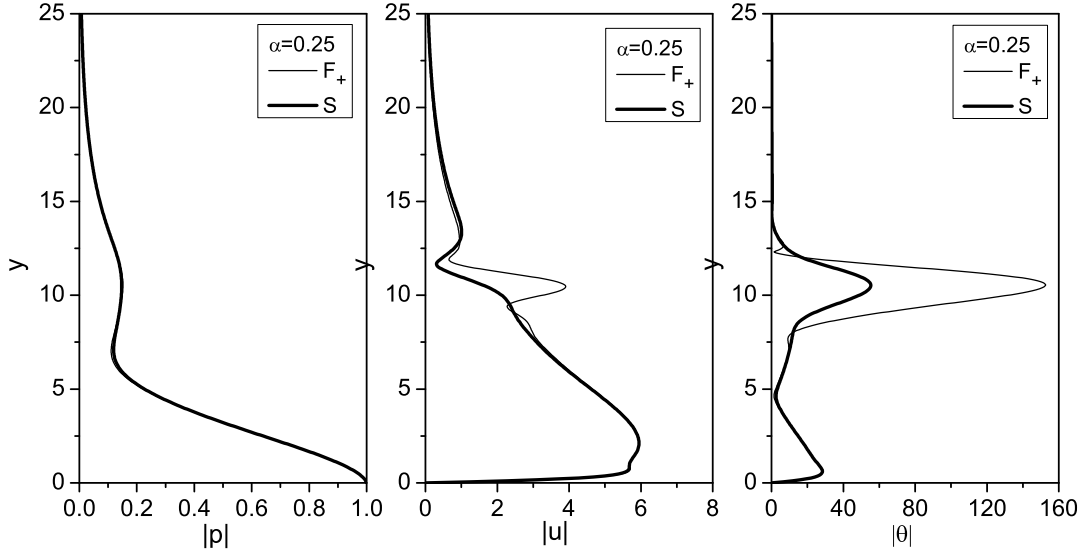


Figure 3.24: Eigenfunctions of fast and slow modes at  $\alpha = 0.25$ ,  $M = 4.2$ ,  $T_0 = 300\text{K}$ ,  $T_w = T_a d$ ,  $R = 2000$ .

### 3.5 Conclusions

The structure of the discrete spectrum in stability analysis of high-speed boundary layers depends on basic flow parameters such as the Mach number, Prandtl number, Reynolds number etc. The spectrum may have two unstable modes that are easily associated with inviscid instabilities of Macks first and second modes. With another choice of the basic parameters, the spectrum may have only one unstable mode having two maxima of the growth rate.

Terminology introduced by Mack [Mac69] using modes 1 and 2 (the well-known first and second modes) is inconsistent with a proper mathematical treatment of normal modes. Macks family of solutions is actually what should be called a normal mode, whereas his definitions of first-mode amplified solutions and second-mode amplified/damped solutions lead to confusion when normal modes are used to represent a solution of the linearized Navier-Stokes equations. The advances of the last decades have made necessary to develop new terminology to replace the old. In mathematical analysis of the initial value problems, it is more convenient to follow the terminology: fast (F) and slow (S) modes. According to this terminology discrete modes  $F_-^{(k)}$  ( $k = 1, 2, \dots$ ) are synchronized with fast acoustic waves of the continuous spectrum at sufficiently small  $R$  in the spatial framework or at sufficiently small  $\alpha$  in the temporal framework. These modes have  $c_r > 1$  and correspond to the regular neutral solutions in the inviscid limit. The discrete mode S is synchronized with slow acoustic wave of the continuous spectrum as  $R \rightarrow 0$  in the spatial framework or as

$\alpha \rightarrow 0$  in the temporal framework. As  $R$  (or  $\alpha$ ) increases, the phase speed of  $F_-^{(k)}$  decreases, and ultimately these modes are absorbed by the continuous spectrum of vorticity/entropy waves at  $c_r = 1 + 0$ . Simultaneously modes  $F_+^{(k)}$  spring from the continuous spectrum at  $c_r = 1 - 0$ , with  $c_i$  being slightly different from  $c_i$  of corresponding modes  $F_-^{(k)}$ . Although the jump of  $c_i$  is very small and is usually ignored in stability computations, the eigenfunction of mode  $F_-^{(k)}$  at  $c_r = 1 + 0$  is essentially different from the eigenfunction of  $F_+^{(k)}$  mode at  $c_r = 1 - 0$ . This difference should be taken into account in solving the initial value problem associated with receptivity to vorticity/entropy waves.

Depending on the flow parameters, both mode S and modes  $F_+^{(k)}$  can be unstable (e.g. Fig. 19a) or only mode S is unstable having several maxima of the growth rate (e.g. Fig. 18a). The low-frequency (long-wavelength) maximum is associated with Macks first mode, whereas the higher-frequency (shorter-wavelength) maxima are associated with Macks second mode, third mode etc. The second-mode instability is due to the branching of modes S and  $F_+^{(1)}$  in the vicinity of their synchronization, the third-mode instability is due to the branching of modes S and  $F_+^{(2)}$  etc. Because this mechanism quickly weakens as the mode number increases, in many cases it is sufficient to consider the second-mode instability only. For weakly coupled modes, the local dispersion relation is expressed in a simple analytical form that allows us to explain the intricate branching patterns observed in numerical solutions. These patterns depend on the locations of branch points in the complex plane ( $\alpha$ -plane for the temporal problem or  $R$ -plane for the spatial stability problem describing propagation of disturbances in a weakly nonparallel boundary layer). Infinitesimal variations of a basic flow parameter (say, Mach number) can cause a jump from one branching pattern to another. Furthermore, in the branch-point vicinity, the modes are singular, e.g. their group velocities tend to infinity. Such unphysical behaviors indicate that instead of isolated normal modes one should consider an initial boundary-value problem formulated for a certain physical setup.

To avoid confusion in terminology we recommend that authors use the terms fast modes (modes  $F_-$  and  $F_+$ ) and slow mode (mode S) for both mathematical analyses and the interpretation of direct numerical simulations dealing with initial-value problems. For interpretation of experimental data and LST results focused on the characteristics of unstable disturbances, it is reasonable to continue to use Macks terminology with the terms Macks first mode and Macks second mode. If both terminologies are involved, the correspondence between fast (or slow) modes and Mack first (or second) modes should be established.

The aforementioned singularities of the discrete spectrum may cause difficulties in stability analyses based on traditional LST and PSE methods. Multiple-mode considerations are needed to clarify this issue. This could be done using approximate theoretical models such as those developed in [FK01], or by solving the linearized Navier-Stokes equations. Direct numerical simulations are also needed to validate predictions of the reduced-order models.



# Chapter 4

## Stability of boundary layers in binary mixtures of oxygen and nitrogen

This section is based on the paper published in collaboration with J. Klentzman and E. Ulker [UKT11]

### NOMENCLATURE FOR CHAPTER 4

- $c$  = complex phase velocity,  $\omega/\alpha = c_r + ic_i$   
 $c_s$  = mass fraction of species  $s$   
 $C_{pf}$  = frozen specific heat,  $cal/g\text{-mole-K}$   
 $C_{p,s}$  = specific heat at constant pressure of species  $s$ ,  $cal/g\text{-mole}$   
 $D_{ij}$  = binary diffusion coefficient,  $cm^2/sec$   
 $\bar{D}_{ij} = pD_{ij}$ ,  $cm^2 atm/sec$   
 $h$  = enthalpy of mixture,  $cal/g\text{-mole-K}$   
 $h_s$  = enthalpy of species  $s$ ,  $cal/g\text{-mole-K}$   
 $(\Delta h_s^f)_{T_{ref}}$  = standard heat of formation of species  $s$  at temperature  $T_{ref}$ ,  $cal/g\text{-mole}$   
 $I$  = total enthalpy,  $h + u^2/2$   
 $K_f$  = frozen thermal conductivity of mixture in thermodynamic equilibrium,  $K_f = K_{tr} + K_{int}$ ,  $cal/cm\text{-sec-K}$   
 $K_{int}$  = internal component of frozen thermal conductivity of a mixture in thermodynamic equilibrium,  
 $K_{tr}$  = translational thermal conductivity of mixture from first Chapman-Enskog approximation,  $cal/cm\text{-sec-K}$   
 $k$  = Boltzmann's constant  
 $k_b^{(r)}$  = forward reaction-rate coefficient for reaction  $r$ ,  $cm^6/mole^2\text{-sec}$   
 $k_f^{(r)}$  = backward reaction-rate coefficient for reaction  $r$ ,  $cm^3/mole\text{-sec}$   
 $Le$  = frozen binary Lewis number,  $\rho C_{pf} D_{ij}/K_f$   
 $M$  = Mach number  
 $M_s$  = molecular weight of species  $s$ ,  $g/g\text{-mole}$   
 $N_A$  = Avogadro's number,  $molecules/g\text{-mole}$

$p$  = pressure, *atm*  
 $Pr$  = frozen Prandtl number,  $\mu C_{pf}/K_f$   
 $R$  = the mixture gas constant  
 $R_s = R_{univ}/M_s$ , gas constant of species  $s$   
 $R_{univ}$  = universal gas constant, *cal/g – mole-K*  
 $Sm$  = Schmidt number,  $\mu/\rho D_{12}$   
 $T$  = temperature, *K*  
 $t$  = time, *sec*  
 $u$  =  $x$ -component of the velocity  
 $v$  =  $y$ -component of the velocity  
 $w$  =  $z$ -component of the velocity  
 $\dot{W}_s$  = net mass rate of production of species  $s$   
 $x$  = coordinate along the surface  
 $X_s$  = molar fraction of species  $s$   
 $y$  = distance from the wall  
 $z$  = spanwise coordinate  
 $\alpha$  =  $x$ -component of the wave number  
 $\beta$  =  $z$ -component of the wave number  
 $\delta$  = boundary layer length scale  
 $\Delta_{ij}^{(1)}$  = defined by Eq. (4.4), *cm-sec*  
 $\Delta_{ij}^{(1)}$  = defined by Eq. (4.2), *cm-sec*  
 $\mu$  = viscosity of mixture from first Chapman-Enskog approximation, *g/cm-sec*  
 $\rho$  = density of mixture, *g/cm<sup>3</sup>*  
 $\rho_s$  = density of species  $s$ , *g/cm<sup>3</sup>*  
 $\omega$  = complex frequency of a perturbation  
 $\bar{\Omega}_{ij}^{(1,1)}$  = average collision cross section for collisions between species  $i$  and  $j$ , *angstrom<sup>2</sup>*  
 $\bar{\Omega}_{ij}^{(2,2)}$  = average collision cross section for collisions between species  $i$  and  $j$ , *angstrom<sup>2</sup>*

## Subscripts

$b$  = backward reaction  
 $e$  = edge condition  
 $f$  = forward reaction  
 $w$  = wall condition

## 4.1 Introduction

Stability theory of compressible boundary layers has been established by theoretical studies by Lees and Lin [LL46], Lees and Reshotko [LR62], and Mack [Mac65, Mac69, Mac75, Mac]. More recent progress in the understanding of stability and receptivity of hypersonic

boundary layers has demonstrated the importance of instability prehistory analysis [FK01, FK02, Fed03]. For example, hypersonic instability prehistory reveals the following features:

1. In the leading edge region, discrete modes can be synchronized with fast and slow acoustic modes. This synchronization provides an efficient channel for the generation of discrete modes by acoustic perturbations;
2. Further downstream, a decaying discrete mode can be synchronized with free-stream entropy and vorticity perturbations. This indicates that entropy and vorticity perturbations can generate a slightly decaying mode;
3. The decaying mode also can be synchronized with an unstable discrete mode (second Mack's mode) leading to the following channel: vorticity/entropy decaying discrete mode second mode.

These spectral features define the physics of boundary layer instabilities, and one must explore the spectral properties in detail in order to understand the receptivity and instability of high-speed boundary layers.

Almost all theoretical and computational studies of the stability of high-speed boundary layers have used the calorically perfect gas model. Real gas effects and surface chemistry bring many other parameters into consideration that can have a strong impact on the spectrum topology. There are a limited number of publications on the stability of boundary layers including real gas effects [MA91, Stu91, SR94, CVM97, HCC97, JSC98, Ber98, Lyt03, LR05]. These studies provide insight into real gas effects in boundary layers of high-speed air.

Malik and Anderson [MA91] considered chemical equilibrium boundary layers in chemical equilibrium high-speed air flow past a flat plate. Real gas effects were introduced through mean flow gas properties, while the stability equations remained basically the same as in the case of a perfect gas. They showed that real gas effects lead to thinner boundary layers with a significantly lower maximum temperature than in the calorically perfect gas model. The stability analysis indicated that real gas effects stabilize the first mode and destabilize the second one. It was found that in real gases the peak of the second mode is shifted to lower frequencies. Stuckert [Stu91] and Stuckert and Reed [SR94] explored the effects of nonequilibrium chemical reactions in air on the stability of the boundary layer over a cone at high Mach numbers. They also observed the frequency shift in the second mode in both equilibrium and nonequilibrium air calculations. Chang et al. [CVM97] considered flows in chemical equilibrium and nonequilibrium using the parabolized stability equations. Hudson, Chokani, and Candler [HCC97] extended the stability analysis to flows in chemical and thermal nonequilibrium. They found that thermal nonequilibrium may destabilize the most unstable oblique first mode. In the considered examples, they did not observe a significant difference in the second mode computations using models of chemical equilibrium or nonequilibrium flows. Johnson, Seipp, and Candler [JSC98] explored the effect of the free stream total enthalpy on the stability of chemical and thermal nonequilibrium flows of air and nitrogen. They showed that perturbations of concentrations have a significant impact on

the stability of high enthalpy air. For the considered cases, they suggested that the total enthalpy effect in air is due to oxygen dissociation and that the dissociation leads to absorption of the perturbation energy. Bertolotti [Ber98] studied the influence of rotational and vibrational energy relaxation on boundary-layer stability. He showed that rotational relaxation has a damping effect on high-frequency perturbations, whereas vibrational relaxation affects the growth rates of perturbations by changing the mean flow. Lyttle [Lyt03] and Lyttle and Reed [LR05] addressed the sensitivity of the stability analysis to the thermodynamic models, reaction rates, and transport models. They found that the growth rate of the second mode can be significantly affected by the chosen model of the chemically reacting air.

In order to assess the impact of real gas effects on stability and receptivity, we suggest building simple knowledge blocks based on the analysis of such gases as nitrogen and oxygen before moving on to the analysis of air. In the present work we consider the inviscid stability of high-speed boundary layers in binary mixtures of oxygen and nitrogen.

## 4.2 The real gas model

We consider binary mixtures of oxygen and nitrogen assuming that they are in local thermal equilibrium; that is, the translational, rotational and vibrational degrees of freedom are associated with a single temperature. The reaction rates, thermodynamic properties and transport properties are modeled following [GYTL90]. The mixtures are considered to be mixtures of perfect gases. The enthalpy,  $h$ , and frozen specific heat at constant pressure,  $C_{pf}$ , of a gas mixture can be determined if the molar fraction of each species,  $X_i$ , is known:

$$\begin{aligned} h &= \sum_i X_i h_i, \\ h_i &= \int_{T_{ref}}^T C_{p,i} dT + \left( \Delta h_i^f \right)_{T_{ref}}, \\ C_{pf} &= \sum_i X_i C_{p,i}, \\ C_{p,i} &= \left( \frac{\partial h_i}{\partial T} \right)_p. \end{aligned} \tag{4.1}$$

Here,  $h_i$  and  $C_{p,i}$  are the enthalpy and specific heat of species  $i$ , respectively, and  $(\Delta h_i^f)_{T_{ref}}$  is the heat of formation of species  $i$  at temperature  $T_{ref}$ . Units of the thermodynamic and transport properties presented in this section are specified in the nomenclature. [GYTL90] provides curve fits for  $h_i$  and  $C_{p,i}$  as functions of the local temperature  $T$ .

The viscosity of the gas mixture is determined by the approximate formula

$$\mu = \sum_i \left( \frac{\frac{M_i}{N_A} X_i}{\sum_j X_j \Delta_{ij}^{(2)}} \right), \tag{4.2}$$

$$\Delta_{ij}^{(2)} = \frac{16}{5} (1.5460 \times 10^{-20}) \left[ \frac{2M_i M_j}{\pi R_{univ} T (M_i + M_j)} \right]^{1/2} \pi \bar{\Omega}_{ij}^{(2,2)},$$

where  $M_i$  is the molecular weight of species  $i$ ,  $N_A$  is Avogadro's number, and  $R_{univ}$  is the universal gas constant. The average collision cross section  $\bar{\Omega}_{ij}^{(2,2)}$  is a function of temperature (the curve fit is given in [GYTL90]).

The frozen thermal conductivity  $K_f$  of the mixture is calculated according to

$$K_f = K_{tr} + K_{int} \quad (4.3)$$

where  $K_{tr}$  is the translational component of the thermal conductivity and  $K_{int}$  is the component of thermal conductivity associated with the internal excitation energy of the molecules. They are given by

$$\begin{aligned} K_{tr} &= 2.3901 \times 10^{-8} \frac{15}{4} k \sum_i \left( \frac{X_i}{\sum_j \alpha_{ij} X_j \Delta_{ij}^{(2)}} \right), \\ K_{int} &= 2.3901 \times 10^{-8} k \sum_i \left( \frac{X_i}{\sum_j X_j \Delta_{ij}^{(1)}} \left( \frac{C_{p,i}}{R_{univ}} - \frac{5}{2} \right) \right), \\ \alpha_{ij} &= 1 + \frac{[1 - (M_i/M_j)] [0.45 - 2.54 (M_i/M_j)]}{[1 + (M_i/M_j)]^2}, \\ \Delta_{ij}^{(1)} &= \frac{8}{3} (1.5460 \times 10^{-20}) \left[ \frac{2M_i M_j}{\pi R_{univ} T (M_i + M_j)} \right]^{1/2} \pi \bar{\Omega}_{ij}^{(1,1)}, \end{aligned} \quad (4.4)$$

where  $k$  is the Boltzmann constant. Quantities  $\bar{\Omega}_{ij}^{(1,1)}$  and  $\Delta_{ij}^{(1)}$  are functions of temperature. Their curve fits are given in [GYTL90].

The binary diffusion coefficient  $D_{ij}$  is evaluated according to the following equation:

$$D_{ij} = \frac{\bar{D}_{ij}}{p} = \frac{kT}{p \Delta_{ij}^{(1)}} \quad (4.5)$$

where  $\Delta_{ij}^{(1)}$  is defined in Eq. (4.4).

The rate of oxygen dissociation is independent of the third body  $M_{cat}$  participating in the collision. The oxygen dissociation reaction  $O_2 + M_{cat} \rightleftharpoons 2O + M_{cat}$  is associated with the following forward and backward reaction rates  $k_f^{(1)}$  and  $k_b^{(1)}$ , respectively:

$$\begin{aligned} k_f^{(1)} &= 3.61 \times 10^{18} T^{-1.0} \exp(-5.94 \times 10^4 / T), \\ k_b^{(1)} &= 3.01 \times 10^{15} T^{-0.5}. \end{aligned} \quad (4.6)$$

The nitrogen dissociation rate depends on the third body. The reaction  $N_2 + N_2 \rightleftharpoons 2N + N_2$  has the reaction rates

$$k_f^{(2)} = 1.92 \times 10^{17} T^{-0.5} \exp(-1.131 \times 10^5/T), \quad (4.7)$$

$$k_b^{(2)} = 1.09 \times 10^{16} T^{-0.5},$$

while the reaction  $N_2 + N \rightleftharpoons 2N + N$  has the reaction rates

$$\begin{aligned} k_f^{(3)} &= 4.15 \times 10^{22} T^{-1.5} \exp(-1.131 \times 10^5/T), \\ k_b^{(3)} &= 2.32 \times 10^{21} T^{-1.5} \times K_{cor}, \\ K_{cor} &= 1.0155. \end{aligned} \quad (4.8)$$

We introduce the correction factor,  $K_{cor}$ , in Eq. (4.8) in order to have the same equilibrium constant for nitrogen dissociation when the third body is  $N_2$  or  $N$ , whereas the reaction rates for nitrogen in [GYTL90] give different ratios  $k_f^{(2)}/k_b^{(2)}$  and  $k_f^{(3)}/k_b^{(3)}$ .

## 4.3 The mean flow problem

### 4.3.1 Governing equations

The two-dimensional mean flow profiles have been found numerically by solving the boundary-layer equations for a reacting gas mixture [Dor62]:

$$\begin{aligned} \frac{\partial \rho u}{\partial x} + \frac{\partial \rho v}{\partial y} &= 0, \\ \rho u \frac{\partial u}{\partial x} + \rho v \frac{\partial u}{\partial y} &= -\frac{dp_e}{dx} + \frac{\partial}{\partial y} \left( \mu \frac{\partial u}{\partial y} \right), \\ \rho u \frac{\partial I}{\partial x} + \rho v \frac{\partial I}{\partial y} &= \frac{\partial}{\partial y} \left[ \frac{\mu}{Pr} \frac{\partial I}{\partial y} + \mu \left( 1 - \frac{1}{Pr} \right) u \frac{\partial u}{\partial y} \right] - \frac{\partial}{\partial y} \left[ \left( \frac{1}{Le} - 1 \right) \rho D_{12} \sum_i h_i \frac{\partial c_i}{\partial y} \right], \\ \rho u \frac{\partial c_i}{\partial x} + \rho v \frac{\partial c_i}{\partial y} &= \frac{\partial}{\partial y} \left( \rho D_{12} \frac{\partial c_i}{\partial y} \right) + \dot{W}_i. \end{aligned} \quad (4.9)$$

Here,  $p_e$  is the pressure at the edge of the boundary layer;  $I = h + u^2/2$  is the total enthalpy;  $Pr$  and  $Le$  are the Prandtl and Lewis numbers, respectively;  $D_{12}$  is the binary diffusion coefficient;  $c_i$  is the mass fraction of species  $i$ ; and  $\dot{W}_i$  is the net mass rate of production of species  $i$ . The equation of state for the gas mixture is

$$p = \sum_i c_i R_i \rho T \quad (4.10)$$

where  $R_i = R_{univ}/M_i$  is the gas constant of species  $i$ .

In the case of a binary mixture of oxygen, the net mass production rate  $\dot{W}_i$  in Eq. (4.10) is given by

$$\begin{aligned}\dot{W}_1 &= -k_f^{(1)} \rho^2 M_1 \frac{c_1}{M_1} \left( \frac{c_1}{M_1} + \frac{c_2}{M_2} \right) + k_b^{(1)} \rho^3 M_1 \frac{c_2^2}{M_2^2} \left( \frac{c_1}{M_1} + \frac{c_2}{M_2} \right), \\ \dot{W}_2 &= 2k_f^{(1)} \rho^2 M_2 \frac{c_1}{M_1} \left( \frac{c_1}{M_1} + \frac{c_2}{M_2} \right) - 2k_b^{(1)} \rho^3 M_2 \frac{c_2^2}{M_2^2} \left( \frac{c_1}{M_1} + \frac{c_2}{M_2} \right).\end{aligned}\quad (4.11)$$

In Eq. (4.11) and what follows, we use subscripts 1 and 2 for molecules and atoms, respectively. For a binary mixture of nitrogen we have

$$\begin{aligned}\dot{W}_1 &= -\rho^2 c_1 \left( k_f^{(2)} \frac{c_1}{M_1} + k_f^{(3)} \frac{c_2}{M_2} \right) + M_1 \left( \frac{c_2}{M_2} \right)^2 \rho^3 \left( k_b^{(2)} \frac{c_1}{M_1} + k_b^{(3)} \frac{c_2}{M_2} \right), \\ \dot{W}_2 &= 2M_2 \frac{c_1}{M_1} \rho^2 \left( k_f^{(2)} \frac{c_1}{M_1} + k_f^{(3)} \frac{c_2}{M_2} \right) - 2M_2 \left( \frac{c_2}{M_2} \right)^2 \rho^3 \left( k_b^{(2)} \frac{c_1}{M_1} + k_b^{(3)} \frac{c_2}{M_2} \right).\end{aligned}\quad (4.12)$$

Rather than using the continuity equations for both species, we apply the total mass conservation law and use only the continuity equation for atoms (or molecules).

The equations are transformed using the Levy-Lees-Dorodnitsyn transformation [Dor62]:

$$\begin{aligned}\psi(\xi, \eta) &= \frac{\sqrt{2\xi}}{p_e} f(\eta, \xi), \\ \xi &= \int_0^x \rho_e u_e \mu_e dx, \eta = \frac{\rho_e u_e}{\sqrt{2\xi}} \int_0^y \frac{\rho}{\rho_e} dy,\end{aligned}\quad (4.13)$$

where subscript  $e$  indicates the value at the edge of the boundary layer. Using the stream function  $\psi(\xi, \eta)$ , one can find the streamwise velocity component

$$u = u_e f'(\xi, \eta), \quad (4.14)$$

where 'prime' indicates the partial derivative with respect to  $\eta$ .

The transformed boundary layer equations are written as

$$\begin{aligned}(Cf'')' + ff'' + \beta_H \left[ \frac{\rho_e}{\rho} - (f')^2 \right] &= 2\xi \left( f' \frac{\partial f'}{\partial \xi} - f'' \frac{\partial f}{\partial \xi} \right), \\ \left( \frac{C}{Pr} g' \right)' + fg' &= \frac{2\xi}{I_e} \frac{dI_e}{d\xi} gf' + \left[ \frac{C}{Sm} \left( \frac{1}{Le} - 1 \right) \sum_i \frac{h_i c_{ie}}{I_e} q_i' \right]' + \frac{u_e^2}{I_e} \left[ \left( \frac{1}{Pr} - 1 \right) Cf'f'' \right]' \\ &\quad + 2\xi \left( f' \frac{\partial g}{\partial \xi} - g' \frac{\partial f}{\partial \xi} \right), \\ 2\xi \left( \frac{\partial q_i}{\partial \xi} f' - q_i' \frac{\partial f}{\partial \xi} \right) &= \left( \frac{C}{Sm} q_i' \right)' + q_i' f - \frac{2\xi}{c_{ie}} \frac{dc_{ie}}{d\xi} f' + \frac{2\xi \dot{W}_i}{\rho \rho_e u_e^2 \mu_e c_{ie}},\end{aligned}\quad (4.15)$$

$$\beta_H = \frac{2\xi}{u_e} \frac{du_e}{d\xi}, g(\xi, \eta) = I/I_e, q_i = c_i/c_{ie}, C = \frac{\rho\mu}{\rho_e\mu_e},$$

where  $Sm = \mu/\rho D_{12}$  is the Schmidt number. Equations (4.15) are to be solved subject the following boundary conditions:

$$\begin{aligned} \eta = 0 : f = f' = 0; \\ \eta \rightarrow \infty : f' \rightarrow 1, g \rightarrow 1, q_i \rightarrow 1. \end{aligned} \quad (4.16)$$

In addition to (4.16), we have to formulate boundary conditions at the wall for the species mass fraction,  $c_i$ , and the enthalpy (or temperature),  $g$ . The boundary condition on the species mass fraction depends on the recombination rate at the wall [Dor62]. The boundary condition on the enthalpy depends on the specific case under consideration. It can be determined by specifying the wall temperature or the heat flux. In the case of the wall heat flux being specified, one must take into account that the heat flux has contributions from thermal conductivity and the species diffusion toward the wall [GYTL90, Dor62].

### 4.3.2 Numerical method

The computational domain in  $\xi$  and  $\eta$  is discretized, and a second-order finite-difference approximation for Eqs. (4.15) similar to that found in [Ceb99] is utilized. The grid points are defined as

$$\begin{aligned} \xi^0 = 0, \xi^n = \xi^{n-1} + k_n, n = 1, 2, \dots, N; \\ \eta_0 = 0, \eta_j = \eta_{j-1} + h_j, j = 1, 2, \dots, J, \end{aligned} \quad (4.17)$$

where  $h_j$  stands for the grid step size (not to be confused with enthalpy in sections 2 and 3).

For the binary mixture, we use

$$c_{1e}q_1 + c_{2e}q_2 = 1$$

Introducing the new dependent variables

$$q_1 = Q_1, q'_1 = Q_2, f = F_1, f' = F_2, f'' = F_3, g = G_1, g' = G_2, \quad (4.18)$$

the first-order equations are discretized and written for the midpoint  $(\xi^n, \eta_{j-1/2})$  :

$$\begin{aligned} \frac{Q_{1j}^n - Q_{1j-1}^n}{h_j} = \frac{Q_{2j}^n + Q_{2j-1}^n}{2} \equiv Q_{2j-1/2}^n, \frac{F_{1j}^n - F_{1j-1}^n}{h_j} = \frac{F_{2j}^n + F_{2j-1}^n}{2} \equiv F_{2j-1/2}^n, \\ \frac{F_{2j}^n - F_{2j-1}^n}{h_j} = \frac{F_{3j}^n + F_{3j-1}^n}{2} \equiv F_{3j-1/2}^n, \frac{G_{1j}^n - G_{1j-1}^n}{h_j} = \frac{G_{2j}^n + G_{2j-1}^n}{2} \equiv G_{2j-1/2}^n. \end{aligned} \quad (4.19)$$

Equations (4.15) are also discretized at the midpoint  $(\xi^{n-1/2}, \eta_{j-1/2})$ . The numerical algorithm is organized by solving the momentum equation and the equation of species conservation separately from the energy equation. That is, initial values for  $G_1$  and  $G_2$  are chosen



and the five equations representing momentum and mass conservation are solved to obtain  $F_1, F_2, F_3, Q_1$ , and  $Q_2$  based on the given  $G_1$  and  $G_2$ . New values  $G_1$  and  $G_2$  are then found by solving the two equations representing energy conservation based on the values for  $F_1, F_2, F_3, Q_1$ , and  $Q_2$  generated in the previous step. The new  $G_1$  and  $G_2$  are then used to obtain updated values of  $F_1, F_2, F_3, Q_1$ , and  $Q_2$  from the momentum and mass conservation equations. This iterative process is continued until a solution within a certain tolerance is reached.

The nonlinear algebraic system of equations is solved using Newton's iterations that lead to a linear system of equations for the "perturbation" of each function  $\delta Q^{(i-1)}$  :

$$Q^{(i)} = Q^{(i-1)} + \delta Q^{(i-1)}, \quad (4.20)$$

where index  $i$  indicates the iteration number. The algorithm leads to a block tridiagonal structure of equations that can be expressed in matrix-vector form

$$A\vec{\delta} = \vec{r}, \quad (4.21)$$

where the coefficient matrix  $\mathbf{A}$  and the vector  $\vec{r}$  are known. For example, Newton's iterations for the discretized equations for  $\delta F_1, \delta F_2, \delta F_3, \delta Q_1$ , and  $\delta Q_2$  lead to the following structure of the algebraic system:

$$A = \begin{pmatrix} A_0 & C_0 & & & \\ B_1 & A_1 & C_1 & & \\ & & \ddots & \ddots & \ddots \\ & & & B_j & A_j & C_j \\ & & & & B_{J-1} & A_{J-1} & C_{J-1} \\ & & & & & B_J & A_J \end{pmatrix}; \quad (4.22)$$

$$\vec{\delta}_j = \begin{pmatrix} \delta F_1 \\ \delta F_2 \\ \delta F_3 \\ \delta Q_1 \\ \delta Q_2 \end{pmatrix}; \quad \vec{r}_j = \begin{pmatrix} (r_1)_j \\ (r_2)_j \\ (r_3)_j \\ (r_4)_j \\ (r_5)_j \end{pmatrix};$$

where the vector  $\vec{r}$  is known from the previous iteration. Matrices  $A_j, B_j$ , and  $C_j$  are  $5 \times 5$  matrices. Their explicit form is given in [Ulk10]. The linear set of equations (4.21) is solved using the block elimination method [Ceb99].

### 4.3.3 Some examples of the mean flow profiles

For the purpose of testing the boundary layer solver, we have considered examples corresponding to the first and second Probstein's integrals [Dor62].

If  $dI_e/dx = 0$ ,  $dc_{ie}/d\xi = 0$ ,  $Pr = Sm = 1$ , and  $\dot{W} = 0$  (frozen flow), the first Probstein's integral is

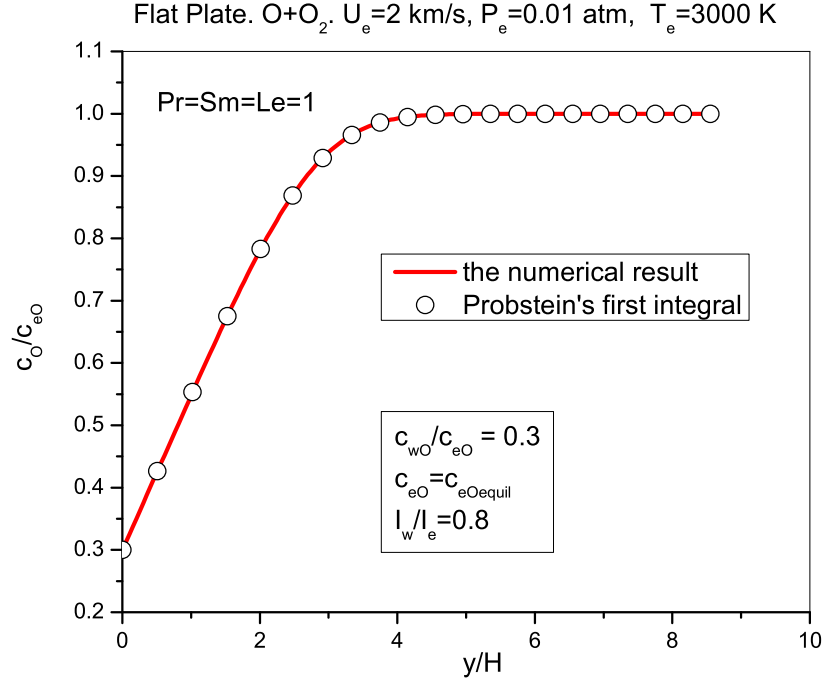


Figure 4.1: Comparison of numerical results for mass fraction with the first Probstein integral.

$$q_i = (q_i)_w + \frac{1 - (q_i)_w}{1 - g_w} (g - g_w), \quad (4.23)$$

where subscript  $w$  stands for values at the wall. Figure 4.1 shows a comparison of the numerical results with the solution given by Eq. (4.23) for a binary mixture of oxygen in the boundary layer past a flat plate at the edge velocity, pressure and temperature of  $u_e = 2\text{km/s}$ ,  $p_e = 0.01\text{atm}$ , and  $T_e = 3000\text{K}$ , respectively. The edge mass fractions were chosen according to the equilibrium state of the mixture, and  $g_w = 0.8$ . The length scale is  $H = \sqrt{2\xi}/(\rho_e u_e)$ .

If  $du_e/dx = 0$ ,  $dc_{ie}/d\xi = 0$ ,  $Sm = 1$ , and  $\dot{W} = 0$  (frozen flow), the second Probstein's integral is

$$q_i = (q_i)_w + [1 - (q_i)_w] f'. \quad (4.24)$$

A comparison of the numerical results with the second Probstein's integral is shown in Fig. 4.2. One can see good agreement between the numerical results and Probstein's integrals.

Another test is illustrated by Figs. 4.3 and 4.4, where the self-similar solution was computed by solving a system of ordinary differential equations (4.20) for a boundary layer past a flat plate at Mach number  $M = 2$ , edge temperature  $T_e = 300\text{K}$ , and Prandtl number

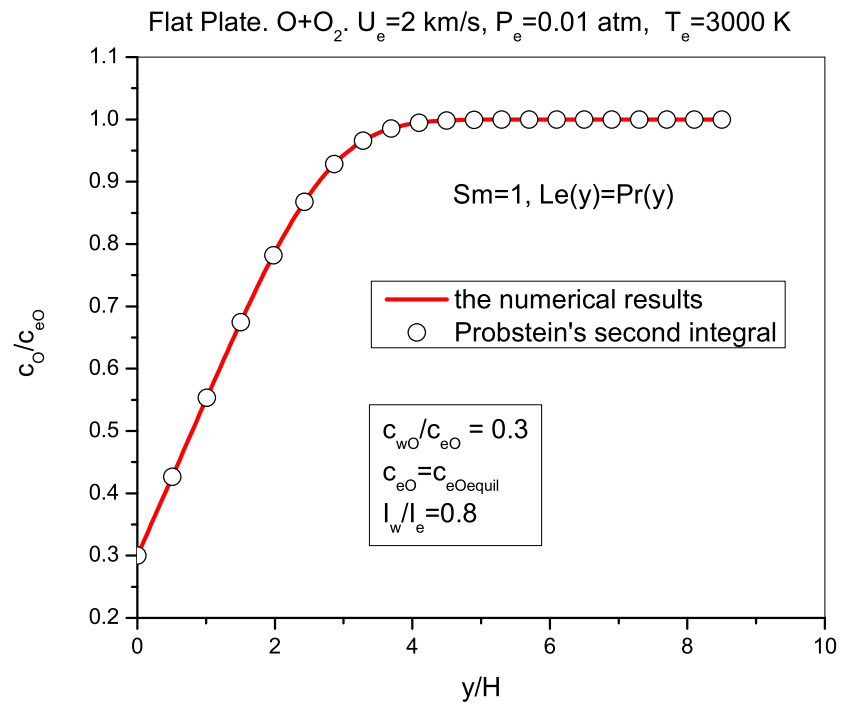


Figure 4.2: Comparison of numerical results for mass fraction and the second Probstein's integral.

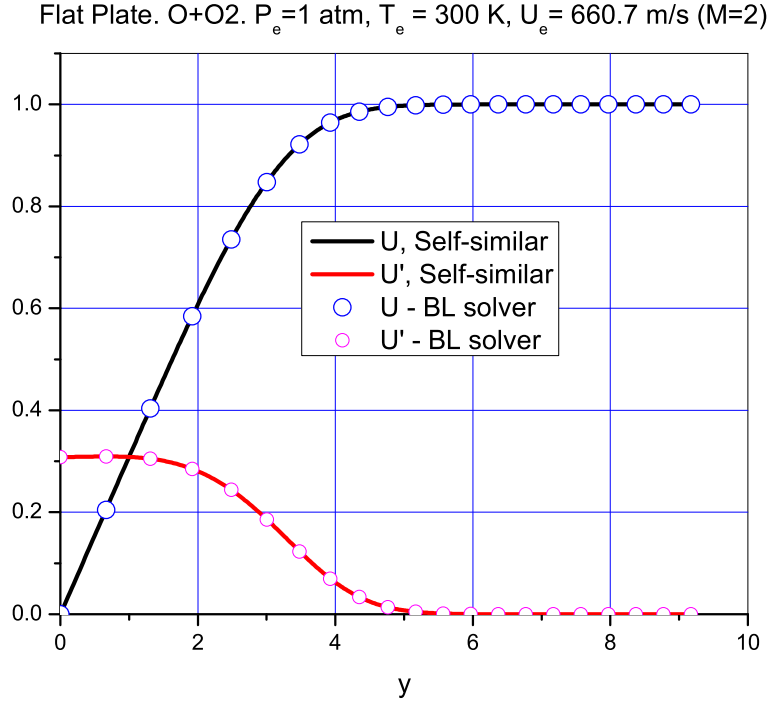


Figure 4.3: Comparison of the velocity profile with the self-similar solution.

$Pr = 0.7$ . In order to compare the results from the new solver with the self-similar solution for a non-reacting calorically perfect gas, we adjusted the formulation in the new solver to have a constant Prandtl number and to consider a gas with constant specific heat. Additionally, we let the viscosity be given by Sutherland's viscosity as a function of temperature.

## 4.4 Inviscid stability analysis. Governing equations and numerical method

### 4.4.1 Governing equations

We consider three-dimensional perturbations in a two-dimensional boundary layer flow using the quasi-parallel flow approximation. The linearized governing equations in the inviscid limit can be written as follows:

$$\rho \frac{\partial u'}{\partial t} + \rho u \frac{\partial u'}{\partial x} + \rho v' \frac{du}{dy} + \frac{\partial p'}{\partial x} = 0, \quad (4.25)$$

$$\rho \frac{\partial v'}{\partial t} + \rho u \frac{\partial v'}{\partial x} + \frac{\partial p'}{\partial y} = 0, \quad (4.26)$$

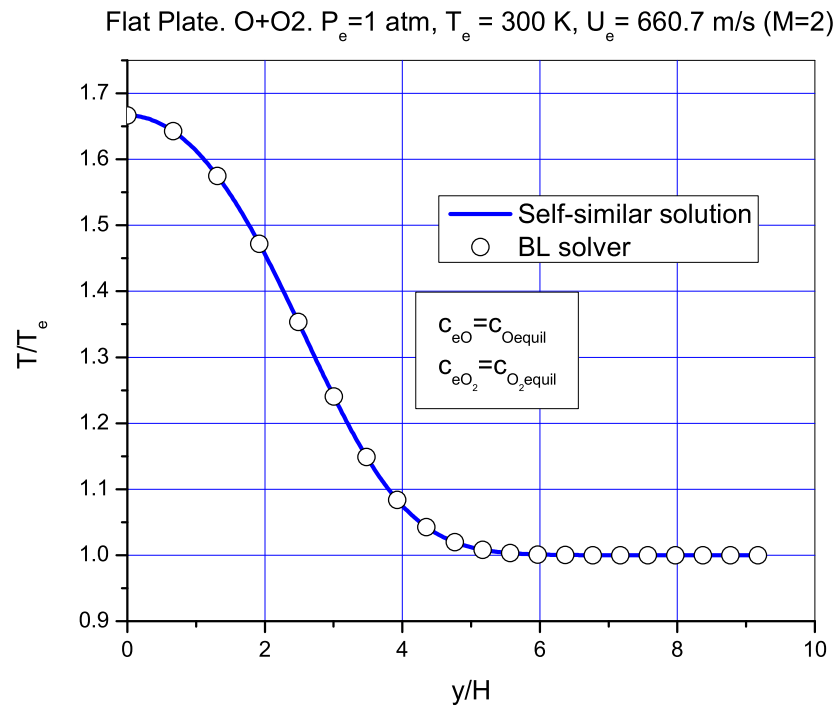


Figure 4.4: Comparison of the temperature profile with the self-similar solution.

$$\rho \frac{\partial w'}{\partial t} + \rho u \frac{\partial w'}{\partial x} + \frac{\partial p'}{\partial z} = 0, \quad (4.27)$$

$$\frac{\partial \rho'}{\partial t} + u \frac{\partial \rho'}{\partial x} + \rho \frac{\partial u'}{\partial x} + \rho \frac{\partial v'}{\partial y} + v' \frac{d\rho}{dy} + \rho \frac{\partial w'}{\partial z} = 0, \quad (4.28)$$

$$\rho \frac{\partial I'}{\partial t} - \frac{\partial p'}{\partial t} + \rho u \frac{\partial I'}{\partial x} + \rho v' \frac{dI}{dy} = 0, \quad (4.29)$$

$$\rho \frac{\partial c'_i}{\partial t} + \rho u \frac{\partial c'_i}{\partial x} + \rho v' \frac{dc_i}{dy} = \dot{W}'_i, \quad (i = 1, 2), \quad (4.30)$$

where ‘prime’ indicates a perturbation. For a binary mixture,  $c'_1 + c'_2 = 0$ , one can find

$$\dot{W}'_1 = \rho c'_1 \left( \frac{\partial \dot{W}_1}{\partial \rho_1} - \frac{\partial \dot{W}_1}{\partial \rho_2} \right) + \rho' \left( \frac{\partial \dot{W}_1}{\partial \rho_1} c_1 + \frac{\partial \dot{W}_1}{\partial \rho_2} c_2 \right) + \frac{\partial \dot{W}_1}{\partial T} T', \quad (4.31)$$

$$p' = c'_1 \rho T (R_1 - R_2) + \rho' RT + \rho RT', \quad (4.32)$$

$$I' = c'_1 (h_1 - h_2) + T' C_{pf} + uu', \quad (4.33)$$

$$C_{pf} = \left( c_1 \frac{dh_1}{dT} + c_2 \frac{dh_2}{dT} \right).$$

The solution of the linearized equations is considered in the form of normal modes

$$q'(x, y, z, t) = \hat{q}(y) \exp[i(\alpha x + \beta z - \omega t)], \quad (4.34)$$

and we arrive at the following system of ordinary differential equations:

$$i(\alpha u - \omega) \hat{\rho} + i\rho(\alpha \hat{u} + \beta \hat{w}) + \rho \frac{d\hat{v}}{dy} + \hat{v} \frac{d\rho}{dy} = 0, \quad (4.35)$$

$$i\rho(\alpha u - \omega) \hat{u} + \rho \hat{v} \frac{du}{dy} + i\alpha \hat{p} = 0, \quad (4.36)$$

$$i\rho(\alpha u - \omega) \hat{v} + \frac{d\hat{p}}{dy} = 0, \quad (4.37)$$

$$i\rho(\alpha u - \omega) \hat{w} + i\beta \hat{p} = 0, \quad (4.38)$$

$$i\rho(\alpha u - \omega) \hat{I} + i\omega \hat{p} + \rho \hat{v} \frac{dI}{dy} = 0, \quad (4.39)$$

$$i\rho(\alpha u - \omega) \hat{c}_1 + \rho \hat{v} \frac{dc_1}{dy} = \hat{c}_1 A_1 + \hat{\rho} B_1 + C_1 \hat{T}, \quad (4.40)$$

$$A_1 = \rho \left( \frac{\partial \dot{W}_1}{\partial \rho_1} - \frac{\partial \dot{W}_1}{\partial \rho_2} \right), B_1 = \left( \frac{\partial \dot{W}_1}{\partial \rho_1} c_1 + \frac{\partial \dot{W}_1}{\partial \rho_2} c_2 \right), C_1 = \frac{\partial \dot{W}_1}{\partial T}.$$

Similar to the inviscid stability analysis in non-reacting gases, one can derive from Eqs. (4.35) – (4.40) a single equation for the pressure perturbation:

$$F_1 \hat{p} - F_2 \frac{d\hat{p}}{dy} + \frac{d^2 \hat{p}}{dy^2} = 0, \quad (4.41)$$

$$F_1 = \frac{(\alpha u - \omega)^2}{RT} - (\alpha^2 + \beta^2) - \frac{(R_1 - R_2)}{R} \frac{\rho B_1}{RT} \frac{(\alpha u - \omega)^2}{D_1} -$$

$$\frac{\left[ \frac{(\alpha u - \omega)^2}{T} + \frac{(R_1 - R_2) G_1}{R} \frac{(\alpha u - \omega)^2}{D_1} \right] \left[ D_1 - \frac{\rho}{RT} B_1 (h_1 - h_2) \right]}{[(h_1 - h_2) G_1 + D_1 C_{pf}]},$$

$$F_2 = \frac{2\alpha}{(\alpha u - \omega)} \frac{du}{dy} - \frac{(R_1 - R_2)}{D_1 R} i \rho (\alpha u - \omega) \frac{dc_1}{dy}$$

$$- \left[ \frac{1}{T} - \frac{G_1 R_1}{D_1 R} \right] \frac{\left[ \left( \frac{dI}{dy} - u \frac{du}{dy} \right) D_1 - i \rho (\alpha u - \omega) (h_1 - h_2) \frac{dc_1}{dy} \right]}{[(h_1 - h_2) G_1 + D_1 C_{pf}]},$$

$$D_1 = i \rho (\alpha u - \omega) + \rho \frac{(R_1 - R_2)}{R} B_1 - A_1,$$

$$G_1 = C_1 - B_1 \frac{\rho}{T},$$

where  $A_1, B_1$ , and  $C_1$  are defined by Eq. (4.40).

Also similar to the stability analysis of non-reacting gases, for the numerical solving of the stability equations we use a system of two differential equations written in dimensionless form:

$$\frac{d\hat{p}}{d\bar{y}} = F_{12} \hat{v}, \quad (4.42)$$

$$\frac{d\hat{v}}{d\bar{y}} = F_{21} \hat{p} + F_{22} \hat{v},$$

where the pressure perturbation is scaled by  $\rho_e u_e^2$ , and the velocity perturbation is scaled by  $u_e$ . The dimensionless coordinate  $\bar{y} = y/\delta$  is defined with the help of a length scale  $\delta$  (usually we use the length scale  $\delta = H = \sqrt{2\xi}/(\rho_e u_e)$  or  $\delta = H_{bl} = \sqrt{\xi}/(\rho_e u_e)$ ). Coefficients  $F_{12}$ ,  $F_{21}$ , and  $F_{22}$  are given by

$$F_{12} = -i \frac{\rho}{\rho_e} \left( \alpha \delta \frac{u}{u_e} - \frac{\omega \delta}{u_e} \right),$$

$$\begin{aligned}
F_{21} &= -i \left( \alpha \delta \frac{u}{u_e} - \frac{\omega \delta}{u_e} \right) \left[ \frac{\rho_e u_e^2}{p_e} - \frac{(R_1 - R_2)}{R} Q_1 - \frac{T_e}{T} S_1 - \frac{\rho_e}{\rho} \frac{((\alpha \delta)^2 + (\beta \delta)^2)}{\left( \alpha \delta \frac{u}{u_e} - \frac{\omega \delta}{u_e} \right)^2} \right], \\
F_{22} &= i \left( \alpha \delta \frac{u}{u_e} - \frac{\omega \delta}{u_e} \right) \left[ \frac{(R_1 - R_2)}{R} Q_2 + \frac{T_e}{T} S_2 - \frac{i \alpha \delta}{\left( \alpha \delta \frac{u}{u_e} - \frac{\omega \delta}{u_e} \right)^2} \frac{du/u_e}{d\bar{y}} + i \frac{\frac{\rho_e}{\rho}}{\left( \alpha \delta \frac{u}{u_e} - \frac{\omega \delta}{u_e} \right)} \frac{d\rho/\rho_e}{d\bar{y}} \right], \\
Q_1 &= \frac{b_{11} a_{22} - a_{12} b_{21}}{a_{11} a_{22} - a_{12} a_{21}}, Q_2 = \frac{b_{12} a_{22} - a_{12} b_{22}}{a_{11} a_{22} - a_{12} a_{21}}, \\
S_1 &= \frac{b_{21} a_{11} - a_{21} b_{11}}{a_{11} a_{22} - a_{12} a_{21}}, S_2 = \frac{b_{22} a_{11} - a_{21} b_{12}}{a_{11} a_{22} - a_{12} a_{21}}, \\
a_{11} &= i \left( \alpha \delta \frac{u}{u_e} - \frac{\omega \delta}{u_e} \right) + \frac{\delta B_1}{u_e} \frac{(R_1 - R_2)}{R} - \frac{\rho_e}{\rho} \frac{\delta A_1}{u_e \rho_e}, \\
a_{12} &= -\frac{\rho_e}{\rho} \frac{\delta T_e C_1}{\rho_e u_e} + \frac{\delta B_1}{u_e} \frac{T_e}{T}, a_{21} = \left( \alpha \delta \frac{u}{u_e} - \frac{\omega \delta}{u_e} \right) \left( \frac{h_1}{I_e} - \frac{h_2}{I_e} \right), \\
a_{22} &= \left( \alpha \delta \frac{u}{u_e} - \frac{\omega \delta}{u_e} \right) \frac{T_e C_{pf}}{I_e}, \\
b_{11} &= \frac{\rho_e u_e^2}{p_e} \frac{\delta B_1}{u_e}, b_{12} = -\frac{dc_1}{d\bar{y}}, \\
b_{21} &= \left( \alpha \delta \frac{u}{u_e} - \frac{\omega \delta}{u_e} \right) \frac{\rho_e u_e^2}{\rho I_e}, b_{22} = i \left( \frac{d(I/I_e)}{d\bar{y}} - \frac{u_e^2}{I_e} \frac{u}{u_e} \frac{d\frac{u}{u_e}}{d\bar{y}} \right).
\end{aligned}$$

In order to arrive at the eigenvalue problem, one must formulate homogeneous boundary conditions for Eqs. (4.42)

$$\begin{aligned}
\bar{y} &\rightarrow \infty : \hat{p} \rightarrow 0; \\
\bar{y} &= 0 : \hat{v} = 0 \quad (\text{or} \quad d\hat{p}/d\bar{y} = 0).
\end{aligned} \tag{4.43}$$

#### 4.4.2 Numerical method

In the present work we consider the stability of boundary layers in the temporal framework. In this case,  $\alpha$  and  $\beta$  are real parameters and the complex frequency  $\omega$  is found as an eigenvalue. Inviscid analysis requires using a path of integration in the complex plane  $\bar{y}$  that is below the critical point  $y_c$  defined by the equation of the critical layer [Mac65]:

$$u(y_c) = c,$$



where  $c = \omega/\alpha$  is the complex phase velocity. In the numerical stability analysis of the inviscid equations for perturbations in non-reacting boundary layer flow, Mack [Mac65] used four terms in the Taylor series in order to determine the velocity and temperature profiles of the mean flow at complex  $y_c$ . The same approach was used in [FT10]. For the present analysis of reacting real gas flow, this approach is not realistic because of the complexity of the equations for the mean flow. In addition, many thermodynamic properties of the mixture are determined using curve fitting, which prevents finding higher derivatives with acceptable accuracy. Therefore, we restrict ourselves by considering only unstable perturbations ( $c_i = \text{Im}(c) > 0$ ) and using the integration path along the real axis  $\bar{y}$ .

We use the fourth-order Runge-Kutta method with a constant step size to solve Eqs. (4.42) starting outside the boundary layer at  $\bar{y}_{max}$  and integrating toward the wall. Outside the boundary layer, the coefficient  $F_{22}$  in Eqs. (4.42) is equal to zero, and one can find

$$\hat{p}(\bar{y}) \sim \exp(\lambda \bar{y}),$$

$$\lambda = \sqrt{F_{12}(\bar{y}_{max}) F_{21}(\bar{y}_{max})}, \text{Re}(\lambda) < 0.$$

For the purpose of code testing, we reproduce results from [FT10] for a non-reacting, calorically perfect gas. Figure 4.5 illustrates a comparison for a two-dimensional perturbation ( $\beta = 0$ ). In order to compare with the results of [FT10], we must enforce properties of a calorically perfect gas on the coefficients of Eqs. (4.42).

## 4.5 Inviscid stability analysis. Numerical examples for reacting binary mixtures

### 4.5.1 Oxygen

In the present work, we are interested in studying the impact of real gas effects on flows in thermal equilibrium. In this sense, the work is aligned with [MA91]. Rather than solving a complete set of ordinary differential equations including thermal conductivity, diffusivity, and viscosity for perturbations in a boundary layer of equilibrium air, we begin with an inviscid analysis and consider binary mixtures of chemically reacting boundary-layer flows. In all examples, we consider two-dimensional perturbations with  $\beta = 0$ .

The first example is the equilibrium free stream flow of oxygen at zero pressure gradient at pressure  $p_e = 0.01$  atm, edge velocity  $u_e = 4.273$  km/s, and edge temperature  $T_e = 2000$  K. The edge parameters in the binary mixture of oxygen correspond to the frozen Mach number  $M = 5.2$ . In this example, we consider an adiabatic and non-catalytic wall. The plate length is equal to 2 m, and the total enthalpy of the free-stream flow is 11 MJ/kg. The total enthalpy is approximately the same as in [JSC98] (9.31 MJ/kg) where the boundary-layer flow of air was considered and a total enthalpy effect was observed. Figures 4.6 and 4.7 illustrate a comparison of the velocity and temperature profiles of the reacting gas with the self-similar solution for non-reacting gas flow with specific heat ratio 1.4. In agreement

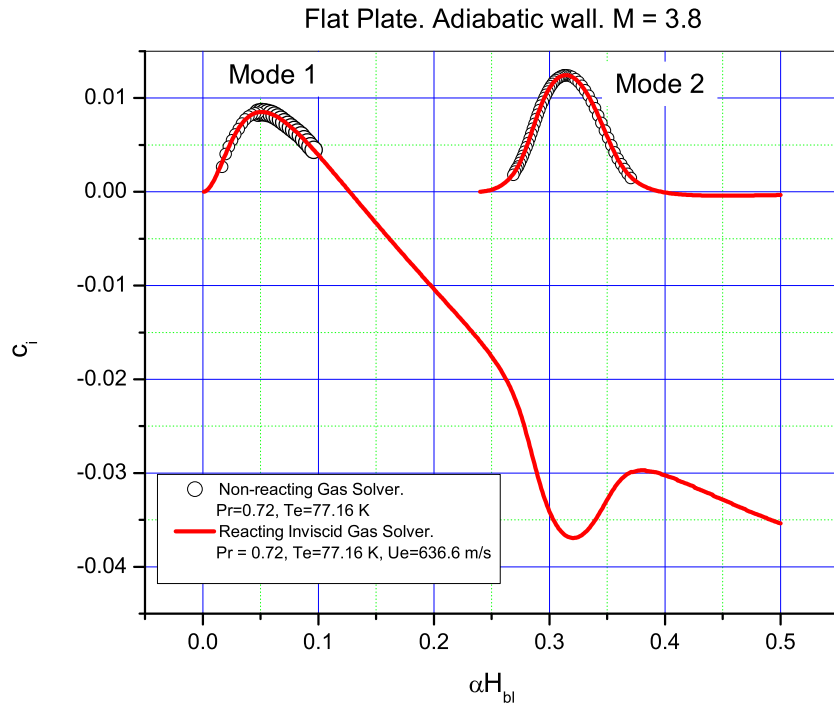


Figure 4.5: Comparison of the growth rates of the present work and Ref. [FT10] for a non-reacting calorically perfect gas.

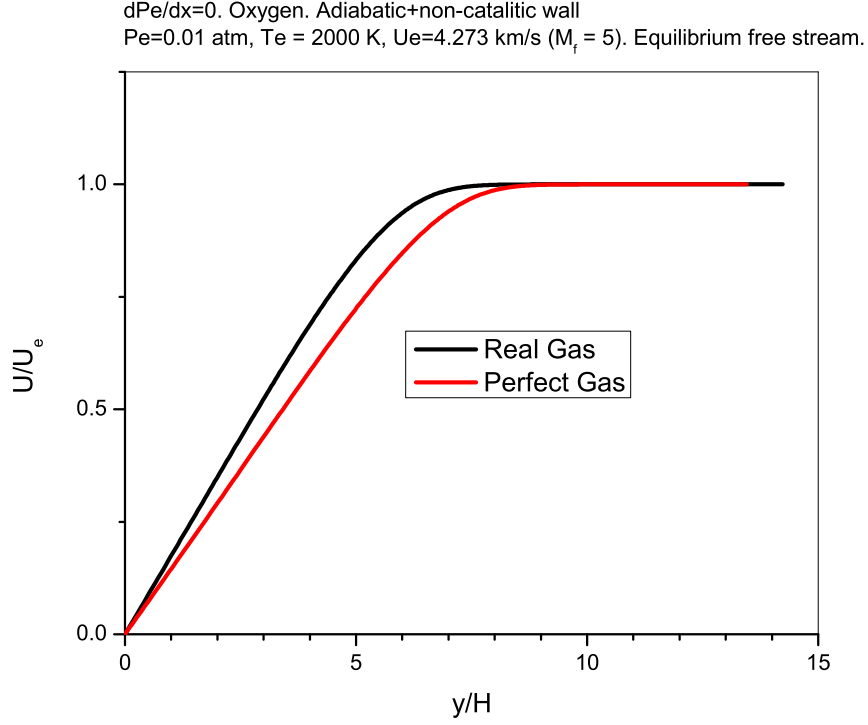


Figure 4.6: Comparison of the velocity profiles in real and perfect gases.

with observations of [MA91], one can see that the thickness of the boundary layer in a real gas is smaller and that there is a dramatic effect on the temperature profile.

In order to examine the influence of real gas effects on the stability equations, we consider coefficients  $F_1$  and  $F_2$  in Eq. (4.41). In the absence of a mass fraction perturbation and assuming a calorically perfect gas,  $F_1$  has the following limit:

$$F_1 = \frac{M^2(\bar{U} - c)^2}{\bar{T}} - 1, \quad (4.44)$$

where  $\bar{U} = u/u_e$  and  $\bar{T} = T/T_e$ . Figure 4.8 shows the real part of the coefficient  $F_1$  for a reacting gas, for a calorically perfect gas using Eq. (4.44) with the velocity and temperature profiles for the real gas mean flow, and according to Eq. (4.44) with the velocity and temperature profiles for a non-reacting gas. Although there are some differences depending on the gas model used for the coefficient  $F_1$ , the curves have the same qualitative behavior. To evaluate the impact of real gas effects on the coefficient  $F_2$  in Eq. (4.41), we consider

$$F_3 = F_2 - \frac{2}{(\bar{U} - c)} \frac{d\bar{U}}{d\bar{y}}. \quad (4.45)$$

In the case of a non-reacting and calorically perfect gas,  $F_3 = -\bar{T}'/\bar{T}$ . Figure 4.9 illustrates the difference between reacting and non-reacting gases for the coefficient  $F_3$ . Qualitatively,

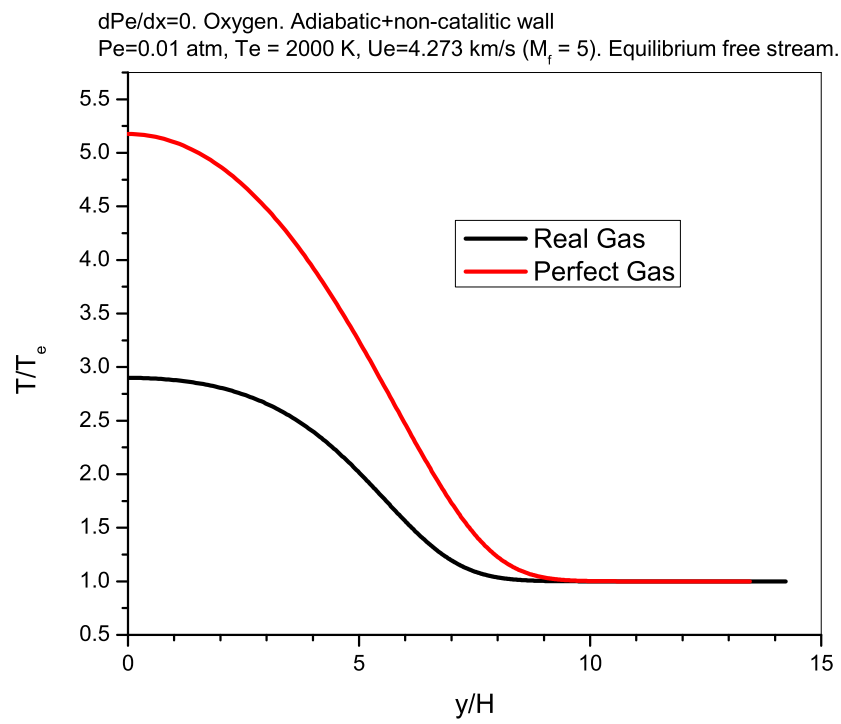


Figure 4.7: Comparison of the temperature profiles in real and perfect gases.

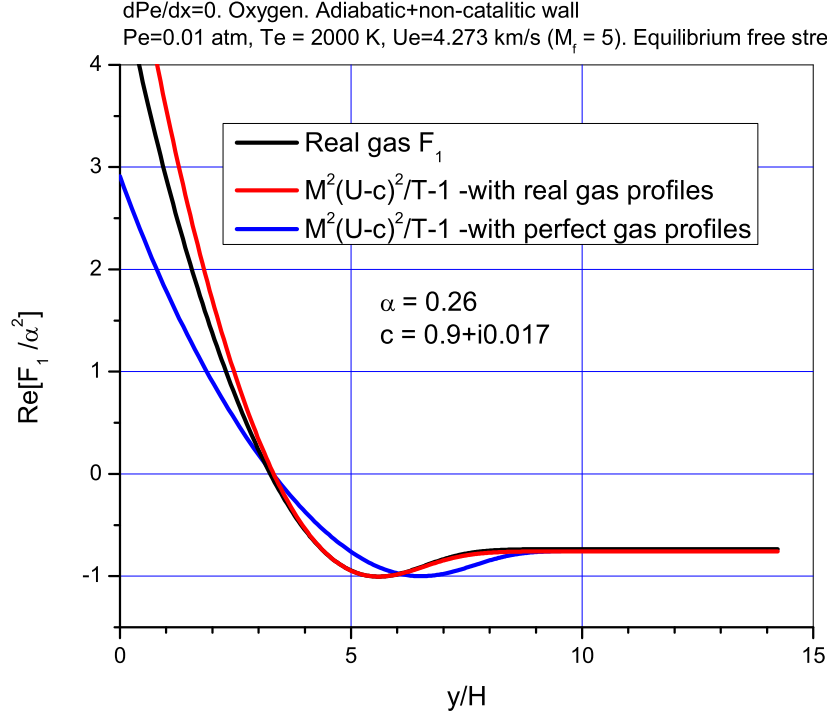


Figure 4.8: Effect of the real gas flow on the coefficient  $F_1$  on Eq. (4.41).

the behavior of the coefficient is the same for both gas models. These comparisons indicate that the structure of the spectrum should be qualitatively the same.

Figure 4.10 shows the imaginary part  $c_i$  versus  $\alpha$ . One case shown in Fig. 10 corresponds to integration with 4000 intervals in the boundary layer on the interval  $[0, 14.23]$ ; the other case corresponds to 8000 intervals. This illustrates that the result is independent of the step size used in integration. One can see the typical structure of the spectrum having the first and the second modes (the reader can find details regarding the terminology in [FT10]).

Figure 4.11 shows a comparison of  $c_i$  for a real gas and a calorically perfect gas. One can see that real gas effects stabilize the first mode and destabilize the second mode. This phenomenon was noted in [MA91]. It was interpreted as the result of wall cooling due to real gas effects. However, interpretation of the result as a pure temperature effect might be incorrect as we will see in our discussion of the results for nitrogen in the following section.

The typical eigenfunctions for mode 1 and mode 2 are shown in Figs. 4.12 and 4.13 as the magnitude of the pressure perturbation. The shapes of these eigenfunctions are similar to those observed for non-reacting gases [Mac69].

The real gas effects appear in the governing stability equations as non-calorically perfect gas properties, as changes in the mean velocity and temperature profiles, and as the presence of perturbations of the species mass fractions. If we exclude the equation for mass fraction perturbations from the governing equations, the eigenvalues are changed as shown in Fig.

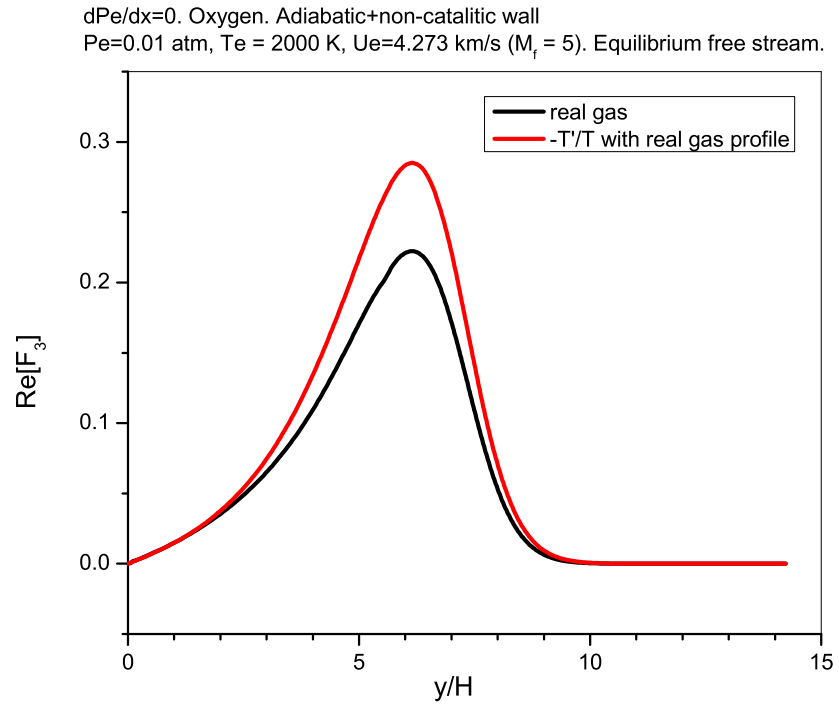


Figure 4.9: Effect of the real gas flow on the coefficient  $F_3$  on Eq. (4.45).

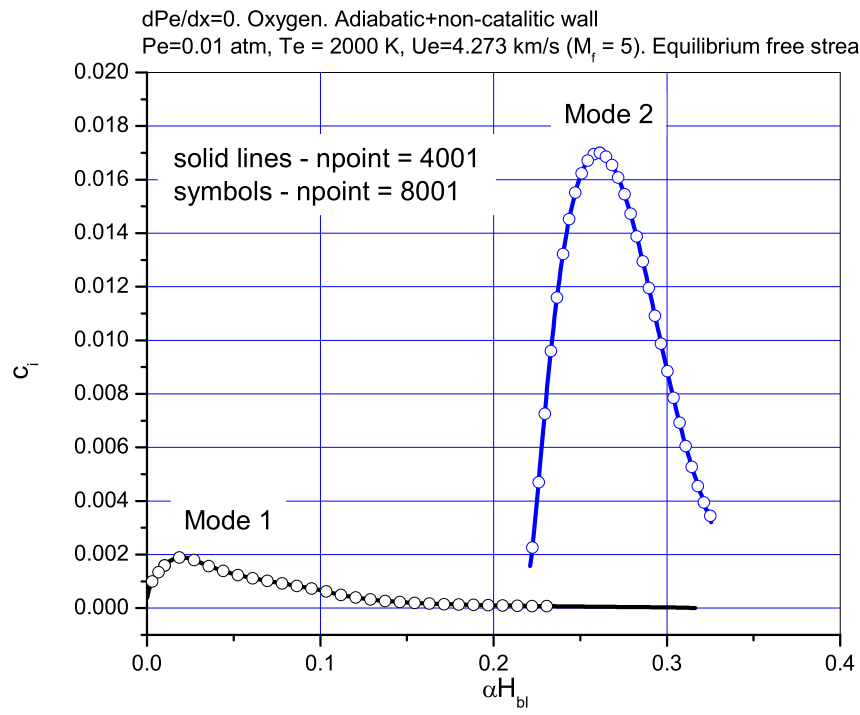


Figure 4.10: Comparison of  $c_i$  for two different step sizes used in integration.

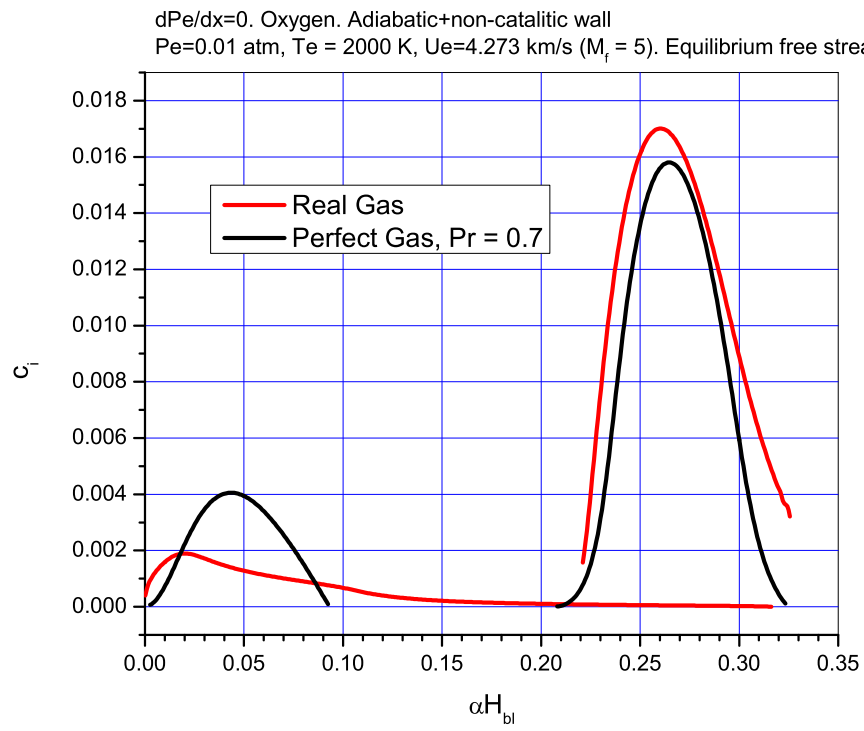


Figure 4.11: Comparison of  $c_i$  for real gas and calorically perfect gas.



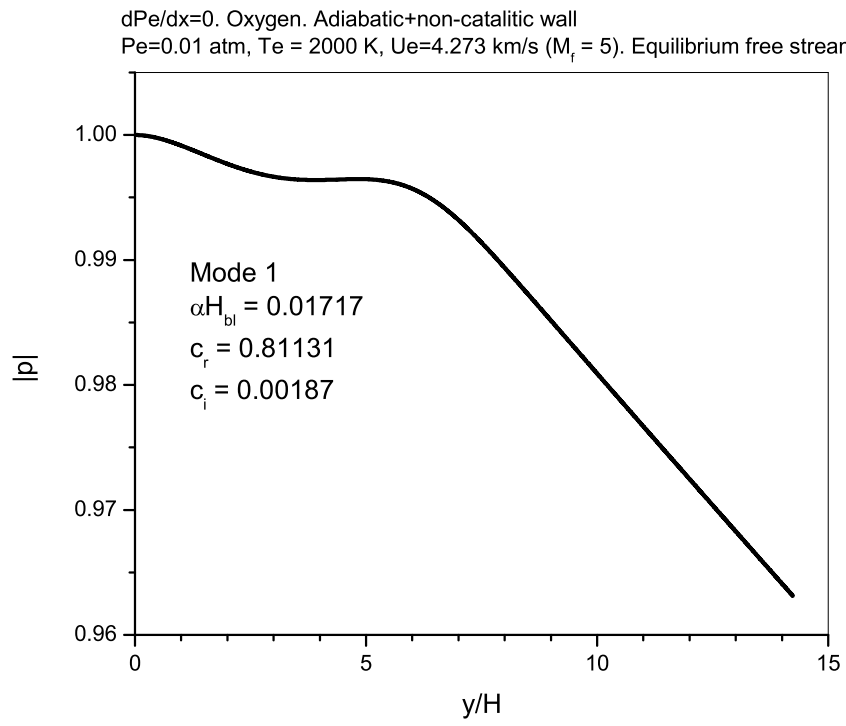


Figure 4.12: Pressure distribution across the boundary layer for mode 1.

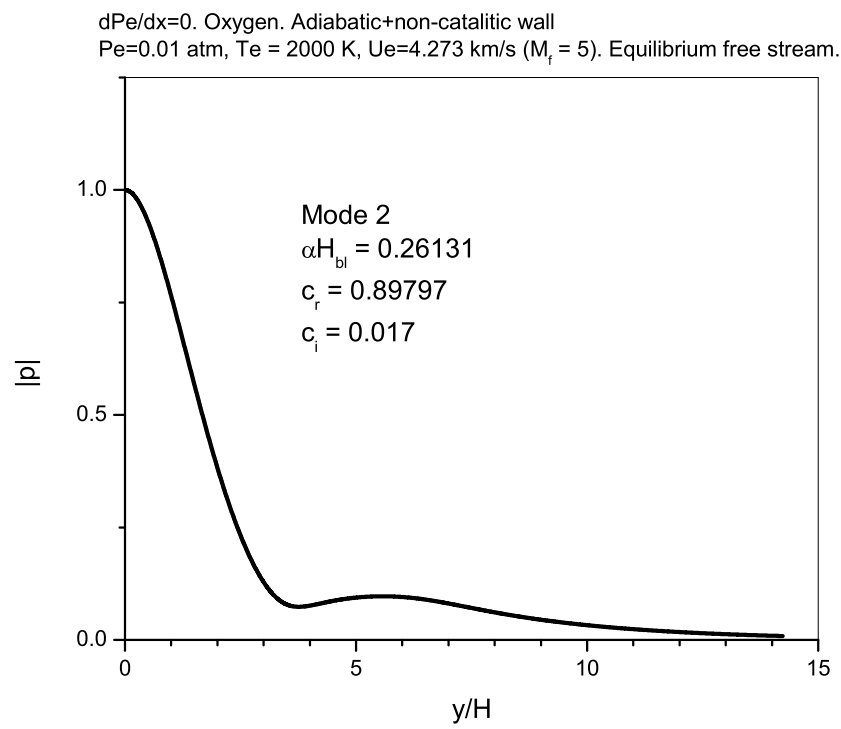


Figure 4.13: Pressure distribution across the boundary layer for mode 2.

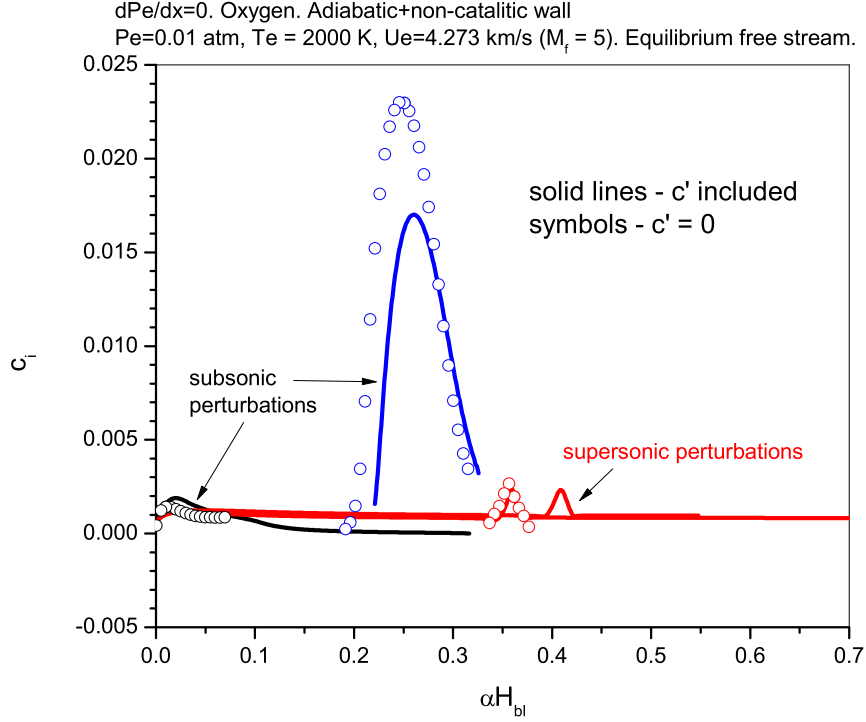


Figure 4.14: Pressure distribution across the boundary layer for mode 2.

4.14. However, the spectrum structure remains qualitatively the same. This result agrees with studies of the free-stream total enthalpy effect in [JSC98]. In addition to modes 1 and 2 that are subsonic (the external flow in the frame moving with the phase speed of the perturbations is subsonic), Fig. 4.14 also shows two supersonic perturbations found in this study. As was pointed out by Mack [Mac69], the supersonic perturbations have a much smaller growth rate than the second mode has. Chang et al. [CVM97] also found unstable supersonic discrete modes in boundary-layer flows of air within the parabolized stability equations framework.

The effect of mass fraction perturbations on the stability of the binary mixture of oxygen in Fig. 4.14 was obtained within the temporal stability framework. In the spatial framework, we observe the same phenomenon (see Fig. 4.15 where the imaginary part of the streamwise wave numbers is shown as a function of frequency).

In the next example, we consider the effect of wall cooling on the inviscid two-dimensional perturbations. The wall temperature is  $T_w = 1000$  K, and the mass fraction of atoms on the wall is  $c_{2w} = 0$ . One can see from Fig. 4.16 that cooling destabilizes the second mode as is known from studies of non-reacting gases. There is not a strong effect on the first mode at the chosen flow parameters.

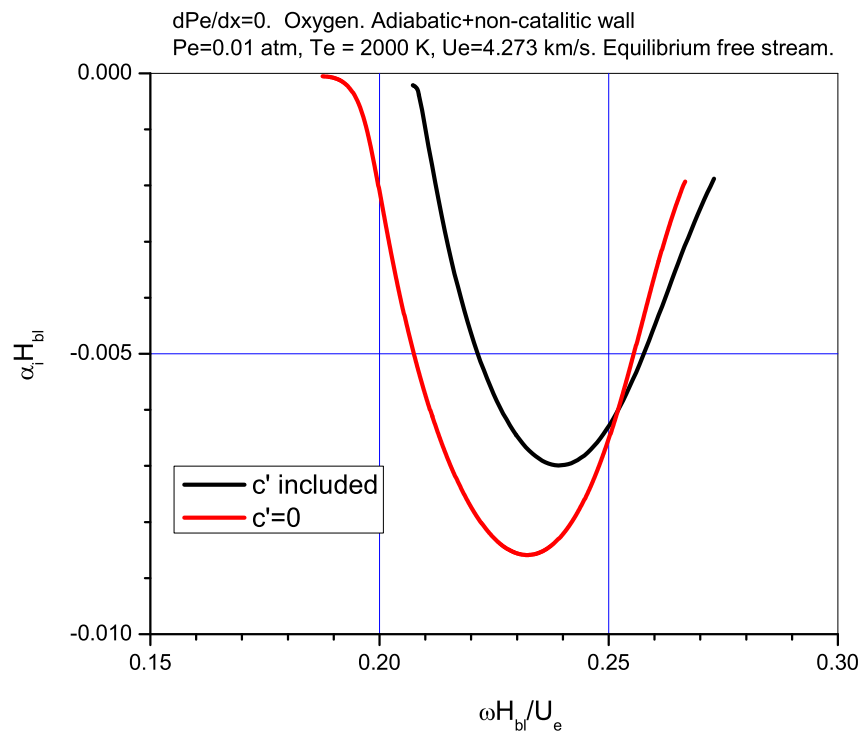


Figure 4.15: Pressure distribution across the boundary layer for mode 2.

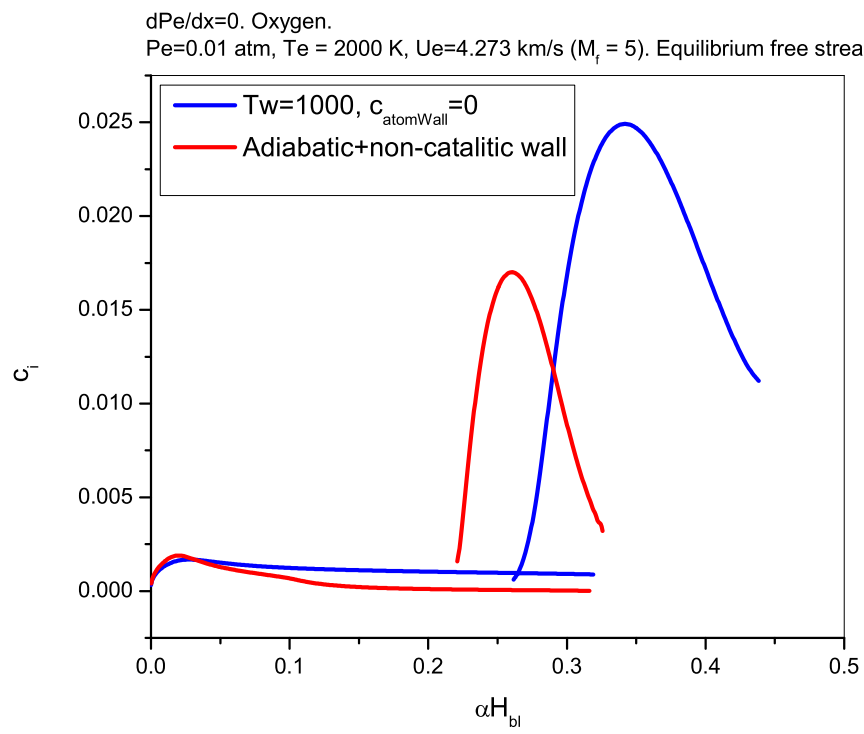


Figure 4.16: Pressure distribution across the boundary layer for mode 2.

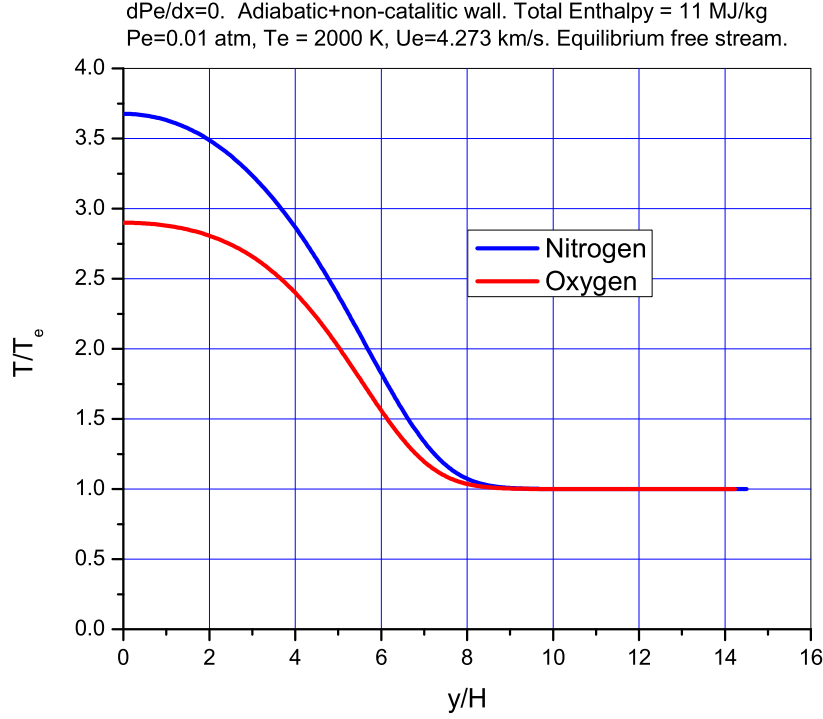


Figure 4.17: Temperature profiles in binary mixtures of oxygen and nitrogen.

### 4.5.2 Nitrogen

In order to compare stability characteristics of nitrogen and oxygen, we consider an equilibrium free stream flow of a binary mixture of nitrogen at the same conditions chosen for oxygen: pressure  $p_e = 0.01$  atm, edge velocity  $u_e = 4.273$  km/s, and edge temperature  $T_e = 2000$  K. The edge parameters correspond to the frozen Mach number  $M = 4.9$ . In order to explain the differences in these two examples (binary mixture of oxygen and binary mixture of nitrogen), Figs. 4.17 and 4.18 show the temperature and mass fraction of molecules in the boundary layers. One can see that the temperature in the oxygen mixture is lower than in the binary mixture of nitrogen due to dissociation.

One could expect that the lower temperature of the wall should destabilize the second mode as was illustrated in Fig. 4.11 by comparison of the results for a perfect gas with results for a binary mixture. However, in the present case, the second mode in nitrogen is more unstable (see Fig. 4.19). This means that an interpretation of the real gas effects on the second mode may be more complicated than simply a pure temperature effect. In the present example, profiles of specific heats of oxygen and nitrogen in the boundary layers are qualitatively different. Figure 4.20 shows the distribution of the frozen specific heats,  $C_{pf}$ , in boundary layers of oxygen and nitrogen. One can see the qualitative difference: while the specific heat of nitrogen increases in the vicinity of the wall due to the temperature effect,

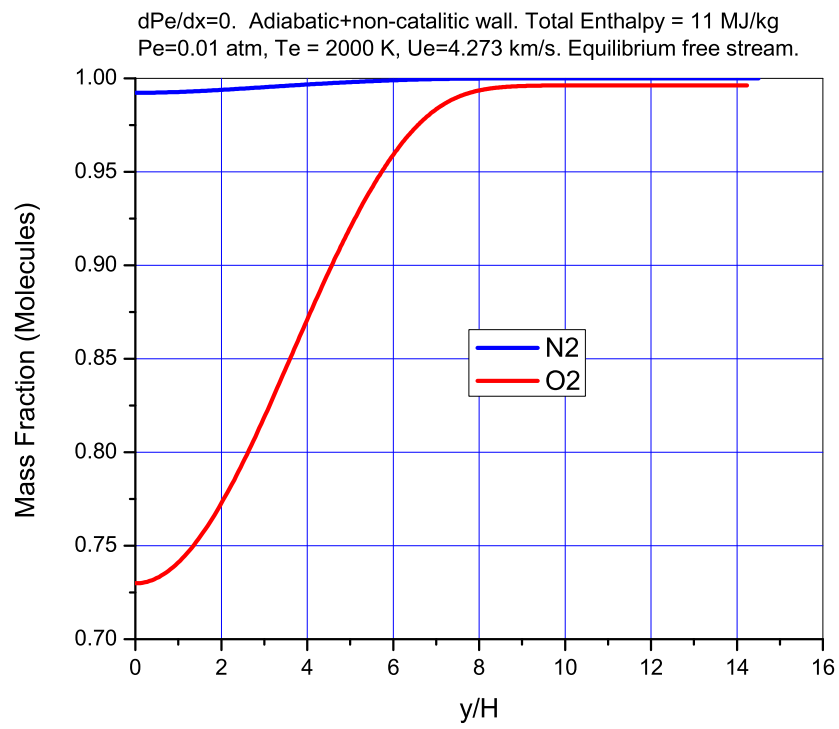


Figure 4.18: Molecular mass fractions in binary mixtures of oxygen and nitrogen.

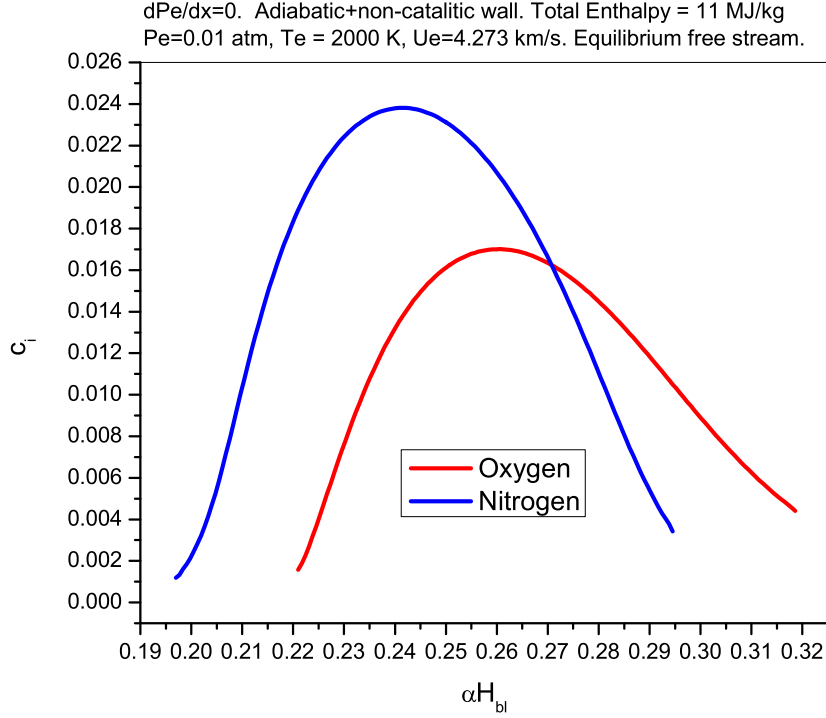


Figure 4.19: Comparison of  $c_i$  for boundary layers in nitrogen and oxygen.

the specific heat of oxygen is affected by dissociation near the wall. This could be the reason for the stabilizing effect on the binary mixture of oxygen in comparison with the binary mixture of nitrogen.

Because there is no significant dissociation in nitrogen, there is no difference between the results with and without mass fraction perturbations in the stability equations (Fig. 4.21).

Figures 4.22 and 4.23 illustrate coefficients  $F_1$  and  $F_3$  in Eqs. (4.41) and (4.45), respectively, for the case of nitrogen at  $\alpha = 0.23$ ,  $c = 0.914 + i0.023$ . One can see that they have the same qualitative behavior as in the case of oxygen presented in Figs. 4.8 and 4.9.

## 4.6 Conclusion

The considered examples of boundary layer flows in binary mixtures of oxygen and nitrogen indicate that the real gas effects stabilize the first mode and destabilize the second one in the inviscid limit of the stability equations (see [FT10] regarding the terminology). The result is in agreement with [MA91] where this observation was made for boundary layer flow for air in chemical and thermal equilibrium with the stability equations including the effect of viscosity, diffusivity, and thermal conductivity. Real gas effects lead to a decrease in wall temperature and can have an impact on the perturbations similar to the wall cooling effect



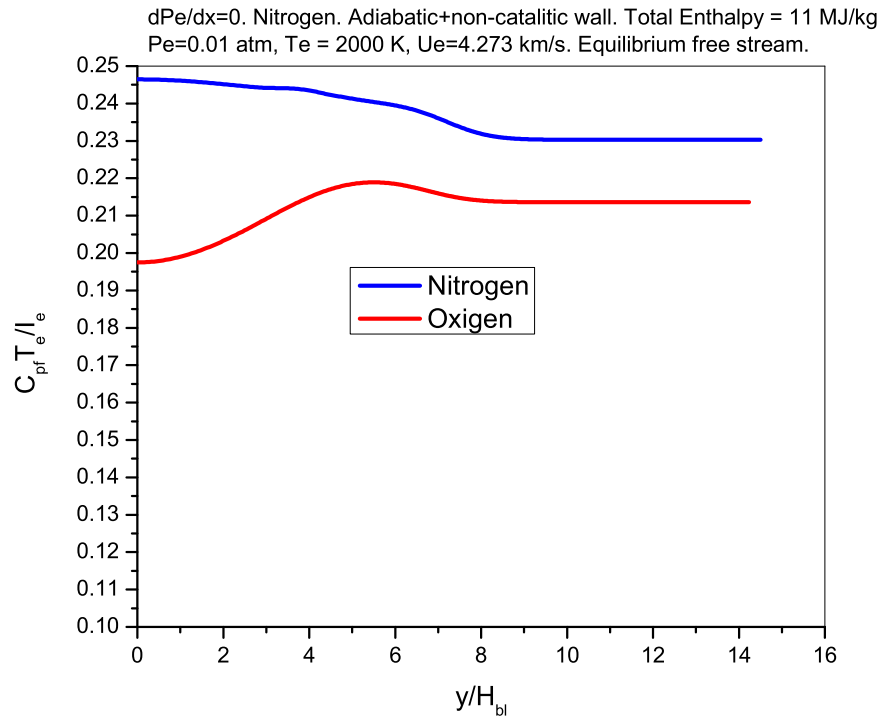


Figure 4.20: Comparison of frozen specific heats in the binary mixtures of oxygen and nitrogen.

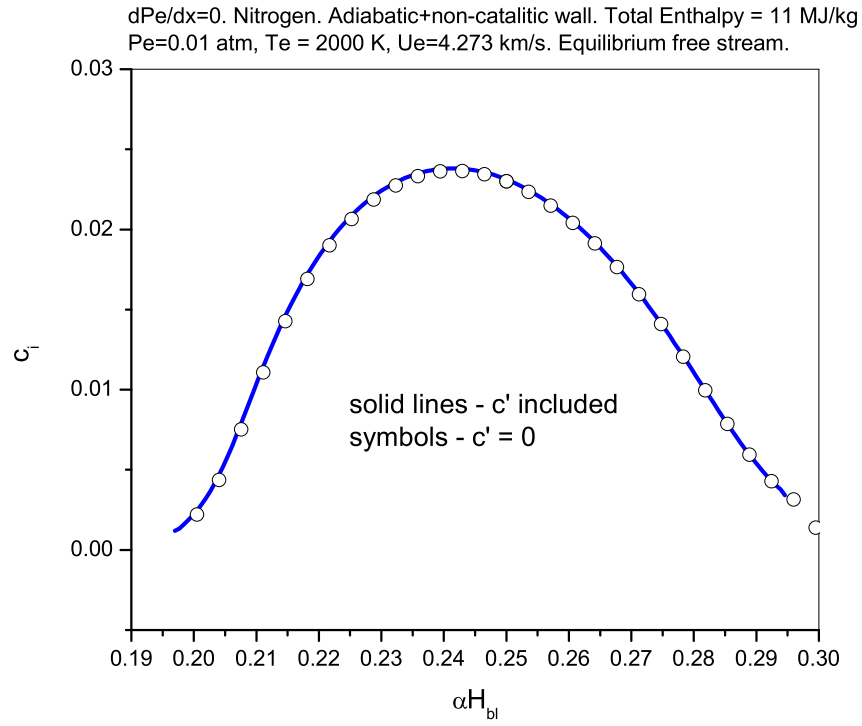


Figure 4.21: Comparison of  $c_i$  for boundary layer in nitrogen when perturbations of mass fractions are included/excluded in the stability equations.

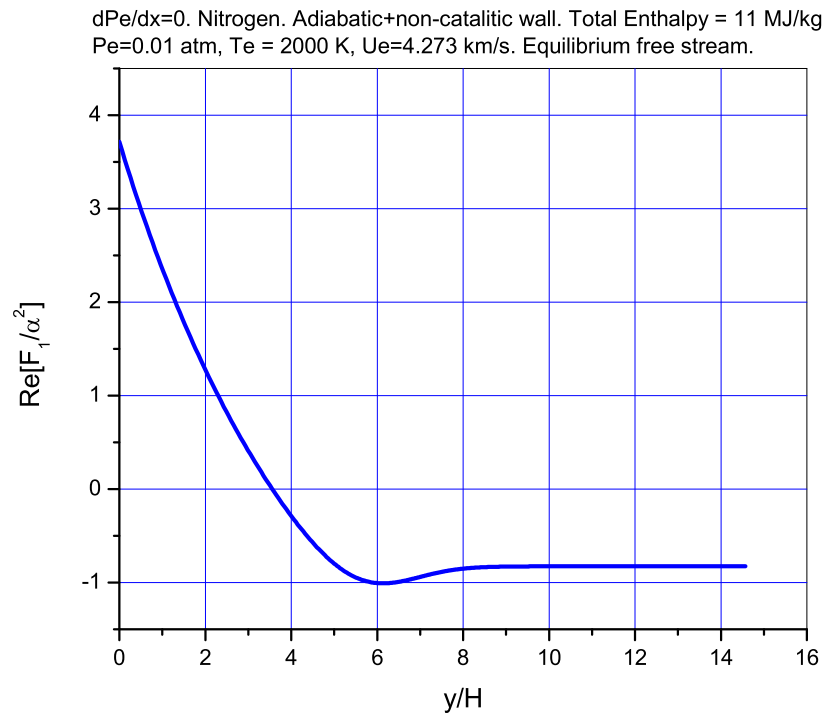


Figure 4.22: Coefficient  $F_1$  in Eq. (4.41). Nitrogen.  $\alpha = 0.23$ ,  $c_i = 0.914 + i0.023$ .

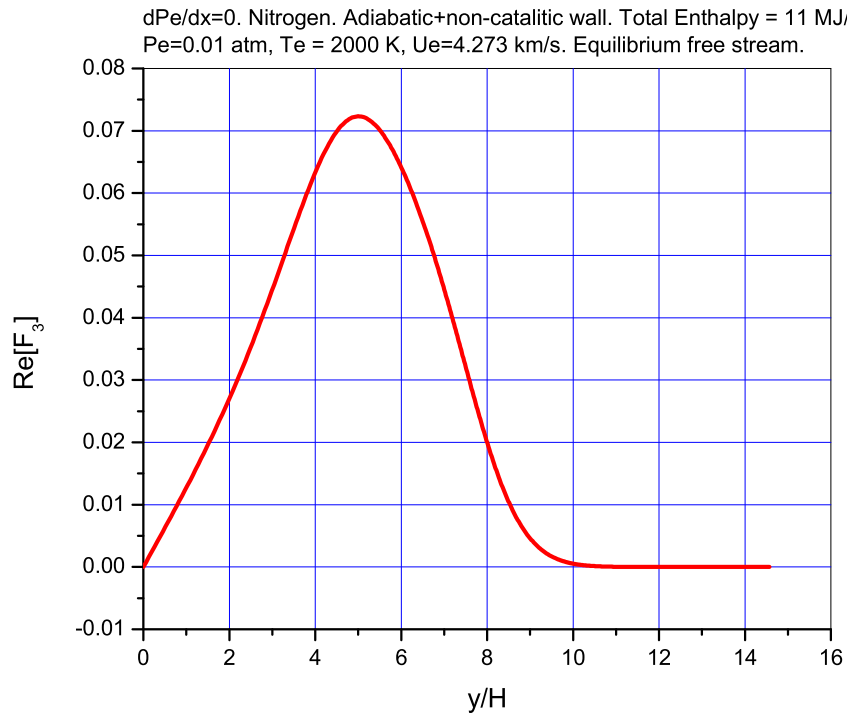


Figure 4.23: Coefficient  $F_3$  in Eq. (4.45). Nitrogen.  $\alpha = 0.23$ ,  $c_i = 0.914 + i0.023$ .

in boundary layers of non-reacting, calorically perfect gases. However, such an interpretation of the wall temperature effect might be misleading when binary mixtures of nitrogen and oxygen are compared. In the considered example, nitrogen does not experience significant dissociation, whereas oxygen goes through dissociation. The difference leads to qualitative differences in the specific heats, and the second mode in nitrogen is more unstable than the second mode in oxygen in spite of the higher wall temperature.

The analysis of the coefficients in the Eq. (4.41) for pressure perturbations in the inviscid limit indicates that the coefficients qualitatively have the same structure as in the case of non-reacting calorically perfect gases. Thus, the conclusions about multiple unstable eigenmodes in high-speed boundary layers should be applicable to the considered examples of reacting boundary layers.

The inviscid stability analysis can be helpful in understanding the structure of the spectrum due to the simplicity of the governing equations. Because there is a limited number of studies examining reacting boundary layers, it should be useful to initially explore the real gas effects in binary mixtures of oxygen and nitrogen before moving on to the five species model of air. The present work demonstrates only a small sampling of examples of the flow conditions, and studies considering a broader range of flow parameters are still required.

# Chapter 5

## Flow instabilities and transition

This chapter is based on the article [Tum10]

### 5.1 Introduction

The first study of laminar-turbulent transition was carried out by [Rey83] who attributed the phenomenon to flow instability. The importance of the problem for design of laminar wings for commercial aircraft, prediction of viscous drag and heating of the surface of a hypersonic vehicle and for many other technical applications stimulated broad theoretical and experimental studies of flow instabilities. Today, one can find a vast bibliography on stability and transition of shear flows ([DR81, SH01, CJJ67]). There are a variety of paths to turbulence depending on the level of free-stream disturbances and also the nature of disturbances introduced into the flow from a wall (for example, isolated and distributed roughness). There are also different mechanisms governing the flow instability. In order to develop and use a reliable tool for transition prediction, one has to be familiar with the broad picture of the transition phenomenon. A short article in the *Encyclopedia* cannot provide all the necessary details on the problem. Our goal is to provide an introduction to the flow instability concept focusing on the Tollmien-Schlichting mechanism in boundary layers and to outline how the knowledge about this mechanism can be used for transition prediction. Other mechanisms such as Görtler and cross-flow mechanisms are discussed in the books cited above, as well as the review papers [RS89, Flo91, Sar94a], and [SRW03] on these topics. We skip the discussion of free shear layers (mixing layers and wakes) that are also important in technical applications.

## 5.2 Stability analysis of two-dimensional flows

### 5.2.1 Outline of the linear stability theory

For simplicity, consider a two-dimensional flow of an incompressible fluid governed by the Navier-Stokes equations. In the Cartesian coordinates, the equations are written as follows:

$$\begin{aligned}\frac{\partial u}{\partial x} + \frac{\partial v}{\partial y} &= 0 \\ \frac{\partial u}{\partial t} + u \frac{\partial u}{\partial x} + v \frac{\partial u}{\partial y} &= -\frac{1}{\rho} \frac{\partial p}{\partial x} + \nu \left( \frac{\partial^2 u}{\partial x^2} + \frac{\partial^2 u}{\partial y^2} \right) \\ \frac{\partial v}{\partial t} + u \frac{\partial v}{\partial x} + v \frac{\partial v}{\partial y} &= -\frac{1}{\rho} \frac{\partial p}{\partial y} + \nu \left( \frac{\partial^2 v}{\partial x^2} + \frac{\partial^2 v}{\partial y^2} \right)\end{aligned}\tag{5.1}$$

where  $u(x, y, t)$  and  $v(x, y, t)$  are  $x$ - and  $y$ - velocity components, respectively;  $p(x, y, t)$  is the pressure;  $\rho$  is the density; and  $\nu$  is the kinematic viscosity. We assume that the flow field can be presented as the sum of a basic steady flow and a perturbation:

$$u = U(x, y) + u'(x, y, t), v = V(x, y) + v'(x, y, t), p = P(x, y) + p'(x, y, t)\tag{5.2}$$

After substituting the decomposed velocities and the pressure in equations (5.1) and subtracting equations for the basic flow, we arrive at a system of nonlinear equations for perturbations  $u'$ ,  $v'$ , and  $p'$ . In the linear stability analysis, the nonlinear terms are neglected assuming that the amplitude of the perturbations is small.

$$\begin{aligned}\frac{\partial u'}{\partial x} + \frac{\partial v'}{\partial y} &= 0 \\ \frac{\partial u'}{\partial t} + U \frac{\partial u'}{\partial x} + v' \frac{\partial U}{\partial y} + \underline{u' \frac{\partial U}{\partial x} + V \frac{\partial u'}{\partial y}} &= -\frac{1}{\rho} \frac{\partial p'}{\partial x} + \nu \left( \frac{\partial^2 u'}{\partial x^2} + \frac{\partial^2 u'}{\partial y^2} \right) \\ \frac{\partial v'}{\partial t} + U \frac{\partial v'}{\partial x} + \underline{u' \frac{\partial V}{\partial x} + v' \frac{\partial V}{\partial y} + V \frac{\partial v'}{\partial y}} &= -\frac{1}{\rho} \frac{\partial p'}{\partial y} + \nu \left( \frac{\partial^2 v'}{\partial x^2} + \frac{\partial^2 v'}{\partial y^2} \right)\end{aligned}\tag{5.3}$$

In a parallel flow such as a fully developed channel flow, the mean velocity profile  $U = U(y)$ ,  $V = 0$ , and so the underlined terms in equation (5.3) are absent. Boundary-layer and free shear layers (mixing layer and far wake) are not parallel. However, these flows can be considered in the first approximation as quasi-parallel because there is a significant difference in the length scales. There is a length scale,  $L$ , associated with the weak dependence of the mean velocity profiles on the streamwise coordinate  $x$ . Another length scale is the boundary-layer thickness (thickness of the mixing layer or wake)  $\delta$ . At high Reynolds numbers,  $\delta/L \sim 1/Re_\delta \ll 1$ , where  $Re_\delta$  is the Reynolds number based on  $\delta$  and characteristic velocity (for example, velocity at the edge of the boundary layer,  $U_e$ ). The  $y$ - velocity component of the mean flow,  $V$ , has the order of magnitude  $U_e/Re_\delta$ , and  $U \sim U_e$ . In addition, the length scale of the perturbation,  $\lambda$ , usually has the same order of magnitude as the boundary-layer thickness ( $L \gg \lambda \geq \delta$ ). As a result of the scale differences, the underlined terms in equations

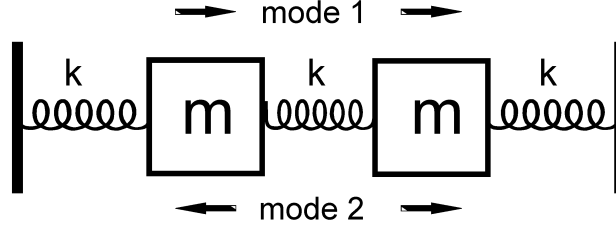


Figure 5.1: A mechanical system having two degrees of freedom

(5.3) are neglected in the first approximation when we study the stability of boundary and free shear layers. In this case, the local coordinate  $x$  in the mean flow velocity profile,  $U(x, y)$ , is treated as a parameter. In other words, the quasi-parallel flow approximation deals with the local velocity profiles that are considered parallel on the scale having an order of magnitude  $\lambda$ .

The quasi-parallel flow approximation leaves us with a system of partial (linear) differential equations. A rigorous mathematical analysis requires the formulation of the initial and boundary conditions for the perturbations and even once these are formulated, the problem may remain challenging. In practical applications, we are not interested in the solution of specific initial-value problems. The main questions of interest are: 1. Is the flow stable/unstable? 2. What are the unstable modes? 3. Are the unstable modes amplified in the flow and how much?

At this point, we should address the normal modes concept. The simplest illustration of the normal modes concept is the mechanical system shown in figure 5.1. The system has two masses  $m$  connected by a spring of stiffness  $k$ . The masses are also attached to the walls by springs. The system has two normal modes of vibration: Mode 1 has frequency  $\omega = (k/m)^{1/2}$  when the masses oscillate in phase, whereas mode 2 has frequency  $\omega = (3k/m)^{1/2}$ , and the displacements of the masses are shifted in  $\pi$ . It is known that any vibration of the system can be presented as a sum of these normal modes. The study of the normal modes provides information about the properties of the system. In order to find the amplitudes and phases of each mode, we have to address a specific initial-value problem for the system.

In hydrodynamic stability analysis, the normal mode concept suggests considering simple wave-like solutions in the complex form as  $q'(x, y, t) = \tilde{q}(y) \exp(i\alpha x - i\omega t)$ , where  $\tilde{q}(y)$  is a complex amplitude function. The idea is the same as in the example of the mechanical system: instead of solving a specific physical initial and boundary value problem, we look at the normal modes existing in the system, expecting that the solution of the initial and boundary value problem for the partial differential equations (5.3) can be presented as a sum of the normal modes. If there is an unstable mode, one can expect that the mode will also be present in the solution of a specific physical problem (in a real experiment or in direct numerical simulation) and that the mode can be observed (perhaps after a space or time delay required for sufficient amplification of the mode). The main difference between the simple mechanical system and perturbations in a fluid is that the continuum medium has an infinite number of degrees of freedom. As result, one can arrive at a enumerable discrete spectrum



or at a continuous spectrum, or at a combination of discrete and continuous spectra.

Following the normal modes concept, the solution of equations (5.3) is sought in the form

$$(u', v', p') = (\tilde{u}, \tilde{v}, \tilde{p}) \exp(i\alpha x - i\omega t) \quad (5.4)$$

and the system of the partial differential equations is reduced to a system of ordinary differential equations (ODEs) for the amplitude functions.

$$\begin{aligned} i\alpha\tilde{u} + \frac{d\tilde{v}}{dy} &= 0 \\ i(\alpha U - \omega)\tilde{u} + \tilde{v}\frac{dU}{dy} &= -\frac{i\alpha}{\rho}\tilde{p} + \nu\left(\frac{d^2\tilde{u}}{dy^2} - \alpha^2\tilde{u}\right) \\ i(\alpha U - \omega)\tilde{v} &= -\frac{1}{\rho}\frac{d\tilde{p}}{dy} + \nu\left(\frac{d^2\tilde{v}}{dy^2} - \alpha^2\tilde{v}\right) \end{aligned} \quad (5.5)$$

Although we use the symbol of an ordinary derivative  $dU/dy$  in the second equation, in the case of weakly non-parallel flows we use the velocity profile at a chosen coordinate  $x$  that is considered as a parameter.

The normal modes are described by the complex amplitude functions that provide amplitudes and phases depending on the coordinate  $y$ . Similarly to the spring-mass problem discussed above, solution of the linearized Navier-Stokes equations can be presented as an expansion into the normal modes.

The system of equations (5.5) can be recast as one ODE of the fourth order for the amplitude function  $\tilde{v}$ :

$$(\alpha U - \omega)(\tilde{v}'' - \alpha^2\tilde{v}) - \alpha\tilde{v}U'' = -i\nu(\tilde{v}^{iv} - 2\alpha^2\tilde{v}'' + \alpha^4\tilde{v}) \quad (5.6)$$

where  $(\dots)'$  stands for  $d/dy$ , and  $\tilde{v}^{iv} = d^4\tilde{v}/dy^4$ . Usually, a perturbation of streamfunction  $\varphi(y) \exp(i\alpha x - i\omega t)$  is introduced ( $\tilde{v} = -i\alpha\varphi$ ), and the equation (5.6) is written in dimensionless form (using the characteristic length scale  $\delta$  and the velocity scale  $U_e$ ) as follows:

$$(\alpha U - \omega)(\varphi'' - \alpha^2\varphi) - \alpha\varphi U'' = \frac{1}{iRe_\delta}(\varphi^{iv} - 2\alpha^2\varphi'' + \alpha^4\varphi) \quad (5.7)$$

This is the famous Orr-Sommerfeld equation in hydrodynamic stability theory. One may compare the Orr-Sommerfeld equation with the system of ODEs (5.5) written using the primitive variables (velocity components and pressure). Equation (5.7) requires the second derivative of the mean flow profile, whereas equations (5.5) contain only the first derivative. Because theoretical studies historically had been linked to equation (5.7), there is a misunderstanding that stability analysis of low speed boundary layers requires the second derivative  $U''$ .

Equation (5.7) (or equations (5.5)) require boundary conditions. On a solid wall, the no-slip boundary condition must be satisfied:

$$\tilde{u} = \varphi' = 0, \quad \tilde{v} = -i\alpha\varphi = 0 \quad (5.8)$$

In the case of an unbounded domain (as in boundary-layer flow), one may require boundness of the solution outside the boundary layer. One can find a solution that decays outside the boundary layer ( $\tilde{u}, \tilde{v}, \tilde{p} \rightarrow 0$ ), and there is also the option that the solution is bounded but does not decay (having an oscillating character along coordinate  $y$ ). The first case corresponds to the discrete spectrum, and the second option leads to the continuous spectrum. The solutions from the continuous spectrum can be associated with perturbations in the free stream. For example, turbulence in the free stream may be associated with a normal mode of the continuous spectrum. In the case of a compressible gas, acoustic and entropy perturbations in the free stream can be presented by the continuous spectrum.

In what follows, our main interest will be associated with modes of the discrete spectrum because these include the unstable modes. In order to clarify the origin of the discrete spectrum, consider equation (5.7) outside the boundary layer, where the dimensionless mean flow velocity  $U = 1$ . At  $y \rightarrow \infty$ , the Orr-Sommerfeld equation becomes an equation with constant coefficients

$$(\alpha - \omega)(\varphi'' - \alpha^2 \varphi) = \frac{1}{iRe_\delta}(\varphi^{iv} - 2\alpha^2 \varphi'' + \alpha^4 \varphi) \quad (5.9)$$

and one can easily find four linear independent solutions

$$\begin{aligned} \varphi_1 &= \exp(-\alpha y), \quad \varphi_2 = \exp(+\alpha y), \quad \varphi_3 = \exp(-\gamma y), \quad \varphi_4 = \exp(+\gamma y) \\ \gamma &= \sqrt{\alpha^2 + iRe_\delta(\alpha - \omega)} \end{aligned} \quad (5.10)$$

To be specific, we chose real parts of  $\alpha$  and  $\lambda$  to be positive. Therefore, only two linear independent solutions  $\varphi_1$  and  $\varphi_3$  decay outside the boundary layer. The decaying solution can be written as a sum

$$\varphi(y) = C_1 \varphi_1(y) + C_3 \varphi_3(y) \quad (5.11)$$

where constants  $C_1$  and  $C_3$  are unknown. One can continue  $\varphi_1$  and  $\varphi_3$  into the boundary layer numerically and try to find the constants  $C_1$  and  $C_3$  from the wall boundary conditions (5.8). However, one of the constants can be chosen arbitrarily because the equation is linear. The choice of the constant will affect the normalization of solution (5.11) only. The other constant can be found from a boundary condition on the wall, whereas the second wall-boundary condition still cannot be satisfied. Only a special choice of parameters  $\alpha, \omega$ , and  $Re_\delta$  can lead to the solution satisfying both boundary conditions (5.8). This is the discrete spectrum obeying a dispersion relation:

$$\omega = \omega(\alpha, Re_\delta) \text{ or } \alpha = \alpha(\omega, Re_\delta) \quad (5.12)$$

At this point, the normal mode analysis leads to an ambiguity that can be readily found in the literature. In the general case, we may consider the wave number,  $\alpha = \alpha_r + i\alpha_i$ , and frequency,  $\omega = \omega_r + i\omega_i$  as complex numbers. Very often two formulations are mentioned: temporal and spatial theories.

In the temporal stability theory,  $\alpha_i = 0$  and  $\alpha_r$  is considered as a parameter, while the complex number  $\omega$  is found from the dispersion relation (5.12). According to the normal

mode presentation, the solution depends on time as  $\exp(-i\omega t) = \exp(-i\omega_r t + \omega_i t)$ . At  $\omega_i > 0$ , the solution is unstable (it grows exponentially in time), and it decays at  $\omega_i < 0$  (the solution is neutral at  $\omega_i = 0$ ).

In the spatial theory,  $\omega_i = 0$  and  $\omega_r$  is considered as a parameter, while the complex number  $\alpha$  is found from the dispersion relation (5.12). Now, the amplitude of the solution depends on the coordinate  $x$  as  $\exp(i\alpha x) = \exp(i\alpha_r x - \alpha_i x)$ . At  $\alpha_i < 0$ , the amplitude grows exponentially downstream, and the perturbation decays downstream at  $\alpha_i > 0$ .

The reader can find an ambiguity in the literature within the choice of temporal or spatial formulation in the stability problems. Usually, the spatial formulation is recommended as more suitable for analysis of experimental data. The ambiguity has its origin at the step when the solution of the partial differential equations is suggested in the form of the normal modes (5.4). At this point, the link with the initial and boundary value problem for a specific experimental setup is lost, and we have the artificial dilemma of spatial versus temporal formulations.

[Gus79] solved an initial value problem for a perturbation in an incompressible boundary layer. [SG81] proved that Gustavsson's solution is an expansion into the modes of discrete and continuous spectra in the temporal formulation. [AR90] considered the signaling problem when a periodic-in-time point source introduces perturbations through the wall starting at  $t = 0$ . They showed that the solution of the initial and boundary value problem can be presented (after some time when the transient effect is smeared out) as an expansion into the modes of discrete and continuous spectra in the spatial formulation. Therefore, the analysis of a specific initial boundary value problem for PDEs leads to a unique expansion of the solution into normal modes without any ambiguity. Usually experiments deal with disturbance source like in the signaling problem, and the spatial framework should be used for analysis of the data.

## 5.2.2 Blasius boundary-layer flow

The neutral stability curve for a Blasius boundary layer flow (section 5.2.2) is shown in figure 5.2, where  $F = 2\pi f\nu/U_e^2$  ( $f$  is the dimensional frequency) and  $Re = (U_e x/\nu)^{1/2}$ .

Figure 5.2 illustrates the remarkable two-fold role of viscosity. The flow is stable at low Reynolds numbers due to the viscous dissipation. The flow is also stable at large Reynolds numbers. This means that the underlying instability mechanism is viscous (see a discussion in section 5.2.4). The unstable modes having a viscous nature are called Tollmien-Schlichting (TS) waves to honor the theoretical studies of W. Tollmien and H. Schlichting in the late 1920s and the early 1930s (see the references in [SG00]). Their theoretical predictions were confirmed by the experiments of [SS43]. Stability experiments require quiet wind tunnels and high accuracy of measurements. The reader can find a number of useful data and description of recent experiments in review papers [Sar94b] and [Sar07].

The imaginary part of the wave numbers (in the spatial formulation) are shown in figure 5.3 as functions of the Reynolds number at the frequency parameters  $F = n \times 10^{-5}$  ( $n = 1, \dots, 5$ ). The Blasius length scale  $L_B = (\nu x/U_e)^{1/2}$  is used in the definition of the dimensionless wave number.

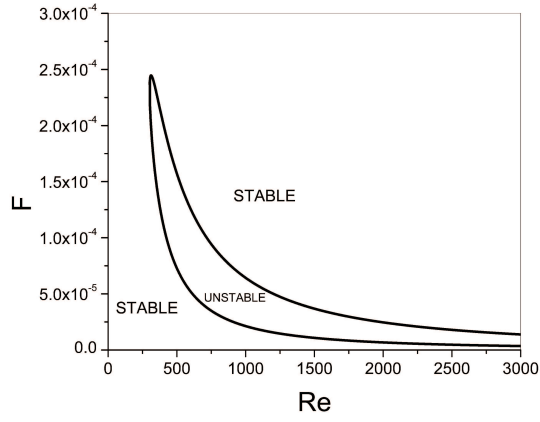


Figure 5.2: Neutral stability curve for Blasius boundary layer flow in the quasi-parallel flow approximation.

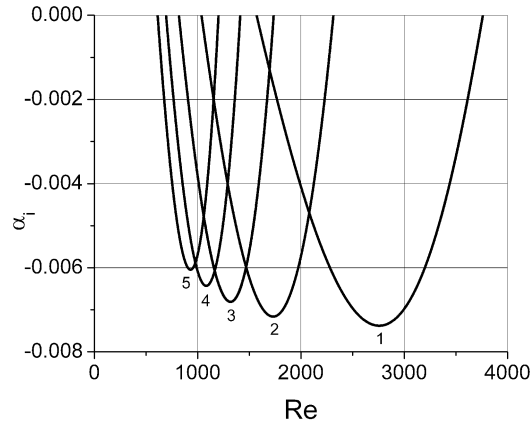


Figure 5.3: Imaginary part of the wave numbers versus the Reynolds number for Blasius boundary layer flow. The numbers  $n = 1, 2, 3, 4$ , and  $5$  indicate the frequency parameters  $F = n \times 10^{-5}$ .

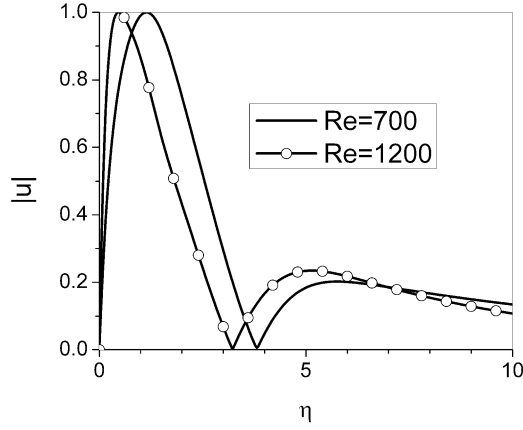


Figure 5.4: Amplitude distributions for streamwise velocity perturbation at  $F = 5 \times 10^{-5}$ .

A typical streamwise velocity profile of the TS waves in a Blasius boundary layer is shown in figure 5.4 at  $F = 5 \times 10^{-5}$  at two Reynolds numbers, where the dimensionless distance from the wall is defined using the Blasius length scale,  $\eta = y/L_B$ . A comparison of the velocity profiles in figure 5.4 illustrates the non-parallel flow effect: the shape of the velocity profiles depends on the distance from the leading edge. One can consider an experiment where velocity perturbations are measured using a hot wire. One can see from figure 5.4 that the measured growth (decay) of the perturbation will depend on the location of the hot wire within the boundary layer. In addition to quantitative corrections required when the nonparallel flow effects are taken into account, the perturbation growth rate will depend on the measured quantity. For example, one may consider amplification measured for the inner or outer maxima in the velocity profile. The nonparallel flow effects in incompressible flows were studied using the method of multiple scales by [Bou72, Gas74]; [SN75, SN77]; and [PN79]. Figure 5.5 illustrates the neutral curves ([Gas74]) defined for the inner and outer maxima of the streamwise velocity profile in a TS wave. The Reynolds number in figure 5.5 is defined using the displacement thickness  $\delta^*$ . Experimental studies of non-parallel flow effects are discussed by [Sar07].

### 5.2.3 The Falkner-Skan profiles. The pressure gradient effect

The Falkner-Skan boundary layer flow is characterized by the edge velocity  $U_e(x) = Cx^m$ . In this case, it is common to use the Hartree parameter  $\beta = 2m/(m+1)$  (section refeae012). Stability analyses have shown that a favorable pressure gradient ( $\beta > 0$ ) stabilizes, and an unfavorable pressure gradient ( $\beta < 0$ ) destabilizes the boundary layer flow. [DR81] collected data for the critical Reynolds numbers (minimal Reynolds numbers on the neutral curve) of Falkner-Skan profiles from [OML69] and plotted them as function of the shape factor  $H = \delta^*/\theta$ , where  $\theta$  is the momentum thickness. Figure 5.6 reproduces the plot from [DR81].

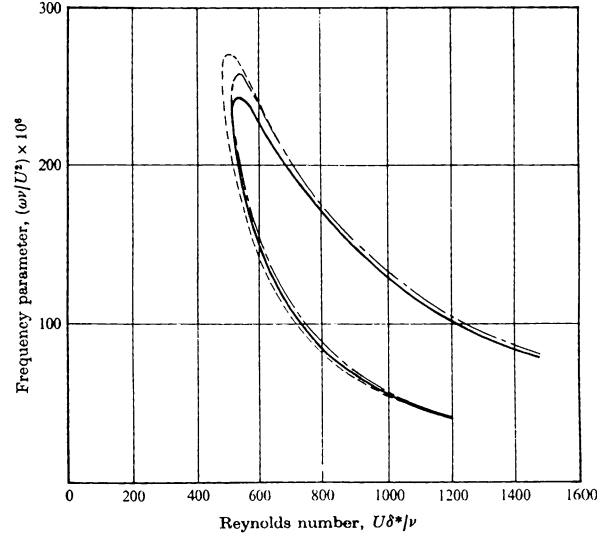


Figure 5.5: Neutral stability curves for Blasius boundary layer flow (Gaster, 1974. Reproduced by permission of Cambridge University Press). Solid line quasi-parallel flow approximation; dash line inner maximum of  $|u|$ ; dash-dot line outer maximum of  $|u|$ .

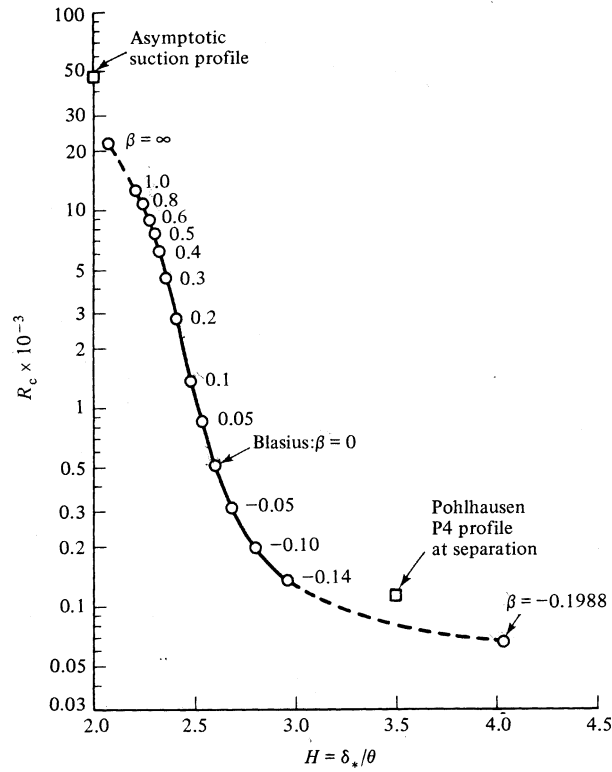


Figure 5.6: The values of the minimal critical Reynolds number (based on the displacement thickness) for the Falkner-Skan family of boundary profiles (Drazin and Reid, 1981).

### 5.2.4 The Rayleigh equation and structure of the TS wave at high Reynolds numbers

In the limit of high Reynolds numbers, the solution of the Orr-Sommerfeld equation can be considered in a rigorous way using the method of matched asymptotic expansions ([Smi79, SB80, BS81, ZR83]). In the following discussion, we are using a simplified structure of the solution at high Reynolds numbers in order to outline the main ideas ([Gra66, Eag69, DR81, SH01]).

In the limit  $\alpha Re_\delta \rightarrow \infty$ , one can ignore the viscous terms in equation (5.7). The inviscid approximation is the Rayleigh equation:

$$(U - c)(\varphi'' - \alpha^2 \varphi) - \varphi U'' = 0 \quad (5.13)$$

where  $c = \omega/\alpha$  is the phase velocity. One can expect that the viscous terms are still significant in the vicinity of the wall (viscous sublayer) in order to satisfy the no-slip boundary condition. In addition, equation (5.13) is singular in the vicinity of the point  $y_c$ , where  $U(y_c) = c$  (critical layer). The viscous terms are significant in the vicinity of the critical layer as well. In order to find an estimate of the viscous sublayer thickness  $\delta_{vs}$ , we compare the order of magnitude of the viscous term having the highest derivative with the order of magnitude of the term  $(U - c)\varphi''$  at  $y \rightarrow 0$ :

$$(U - c)\varphi'' \sim c\varphi'' \sim c\varphi/\delta_{vs}^2, \quad \frac{1}{\alpha Re_\delta} \varphi^{iv} \sim \frac{\varphi}{\alpha Re_\delta \delta_{vs}^4} \quad (5.14)$$

These terms are balanced when  $\delta_{vs} \sim (\alpha c Re_\delta)^{-1/2}$ . In order to estimate the thickness of the critical layer, we consider a balance of the same terms at  $y \rightarrow y_c$ .

$$(U - c)\varphi'' \sim \frac{U'_c \varphi \delta_c}{\delta_c^2}, \quad \frac{1}{\alpha Re_\delta} \varphi^{iv} \sim \frac{\varphi}{\alpha Re_\delta \delta_c^4} \quad (5.15)$$

where  $U'_c$  is the derivative at the critical point. A balance of the terms requires  $\delta_c \sim (\alpha U'_c Re_\delta)^{-1/3}$ . There are two possibilities. The critical layer can be close to the wall and overlap with the viscous sublayer. In this case, the viscous effects are significant in the vicinity of the wall only. Such a structure corresponds to the asymptotic behavior of the lower branch of the neutral curve. Another possibility is when the critical layer and viscous sublayer are separated, and there is an inviscid region between the viscous layers. This structure corresponds to the upper branch of the neutral curve.

In order to shed some light onto the nature of the viscous instability mechanism, let us consider a neutral perturbation with  $\alpha > 0$  corresponding to the upper branch of the neutral curve. One can easily derive from the Rayleigh equation the following result:

$$\begin{aligned} \frac{d}{dy} (\bar{\varphi} \varphi' - \varphi \bar{\varphi}') &= 0 \\ (\bar{\varphi} \varphi' - \varphi \bar{\varphi}') &= 2i \operatorname{Im} (\bar{\varphi} \varphi') = \text{const} \end{aligned} \quad (5.16)$$

where bar stands for complex conjugation.

In order to understand the physical meaning of  $(\bar{\varphi}\varphi' - \varphi\bar{\varphi}')$ , consider the Reynolds stress that the neutral perturbation generates in the boundary layer.

$$\tau = -\frac{1}{T} \int_0^T u^*(x, y, t) v^*(x, y, t) dt \quad (5.17)$$

$$T = 2\pi/\omega$$

The velocity components  $u^*(x, y, t)$  and  $v^*(x, y, t)$  are presented using the complex stream function as follows

$$u^*(x, y, t) = \text{Re} [\varphi' e^{i(\alpha x - \omega t)}], \quad v^*(x, y, t) = \text{Re} [-i\alpha\varphi e^{i(\alpha x - \omega t)}] \quad (5.18)$$

After substitution of (5.18) into integral (5.17), one can find the Reynolds stress

$$\tau = -\frac{\alpha i}{4} [\bar{\varphi}\varphi' - \varphi\bar{\varphi}'] = \frac{\alpha}{2} \text{Im} (\bar{\varphi}\varphi') \quad (5.19)$$

Using equation (5.16), we conclude that the Reynolds stress is constant within the inviscid regions at  $\alpha Re_\delta \rightarrow \infty$ . Because the eigenfunction corresponding to the TS wave decays at  $y \rightarrow \infty$ , we conclude that the Reynolds stress  $\tau = 0$  in the inviscid region above the critical layer. The Reynolds stress also has to be constant within the inviscid region between the viscous sublayer and the critical layer, and the sign of  $\tau$  is very important. In order to have energy production,  $\tau$  must be positive.

We can explore the sign of  $\tau$  using an approximate solution of the Orr-Sommerfeld equation in the vicinity of the wall. The leading term is determined by the solution of the following equation:

$$-\omega\varphi'' = \frac{1}{iRe_\delta}\varphi^{iv} \quad (5.20)$$

Equation (5.20) was obtained from equation (5.7) when the highest derivatives are kept in viscous and inviscid terms at  $y \rightarrow 0$ . The no-slip boundary conditions on the wall are as follows:

$$\varphi(0) = \varphi'(0) = 0 \quad (5.21)$$

The solution of the equation satisfying the boundary conditions can be easily found (linear independent solution  $\exp(+q\zeta)$  has to be excluded):

$$\varphi = e^{-q\zeta} + q\zeta - 1 \quad (5.22)$$

$$q = \frac{1-i}{\sqrt{2}}, \quad \zeta = y(\omega Re_\delta)^{1/2}$$

In the limit  $\zeta \rightarrow \infty$  (outer limit of the inner solution) we find,

$$\varphi \sim q\zeta - 1 \quad (5.23)$$



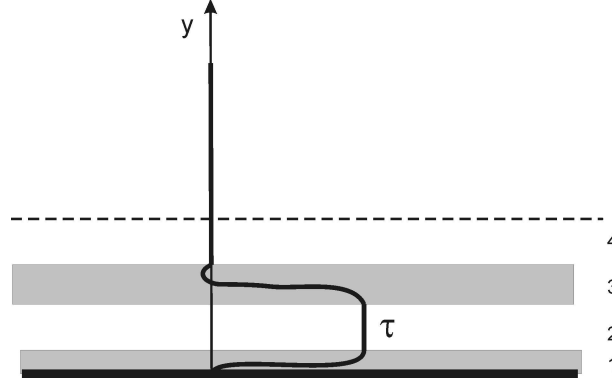


Figure 5.7: Sketch of the Reynolds stress distribution across the boundary layer in the high Reynolds number limit when the viscous sublayer and critical layer are separated (upper branch of the neutral curve). 1 viscous sublayer; 2 inviscid region; 3 critical layer; 4 inviscid region.

Substitution of the result into (5.19) gives the Reynolds stress outside of the viscous sublayer.

$$\tau = \frac{\alpha \sqrt{\omega Re_\delta}}{2\sqrt{2}} \quad (5.24)$$

A sketch of the asymptotic Reynolds stress structure is shown in figure 5.7. It is important that  $\tau$  is positive. In other words, the viscous sublayer provides a phase shift between the streamwise,  $u^*(x, y, t)$ , and normal,  $v^*(x, y, t)$ , velocity components leading to  $\tau > 0$  (energy production). In the case of the neutral perturbation, one can show that the energy production between the critical and viscous sublayer is balanced by the energy dissipation within the viscous sublayer ([ZT87]).

### 5.2.5 The Rayleigh theorem

Using the Rayleigh equation, one can establish the following Rayleigh theorem ([DR81, SH01]): A necessary condition for inviscidly unstable flow is the existence of an inflection point  $U''(y_*) = 0$ . The Rayleigh theorem provides a necessary but not a sufficient condition. It is interesting to compare neutral curves for Blasius boundary layer flow with neutral curves for boundary layers with an unfavorable pressure gradient when the velocity profile has an inflection point. A sketch of the neutral curves is shown in figure 5.8 ([Pan05]). Other typical examples of inviscidly unstable flows are mixing layers and wakes. Examples of their stability analysis are presented in books by [SH01], and [CJJ67]. Although  $U''$  is not required for the stability analysis (section 5.2), an inflection point indicates a possibility for the inviscid mechanism of the flow instability.

Inviscid stability analysis of a mixing layer becomes very simple in the case when the wave length of the perturbation is much larger than the mixing layer thickness ( $\lambda \gg \delta$ ). In this limit, one may consider two uniform streams having velocities  $U_1$  and  $U_2$ . The

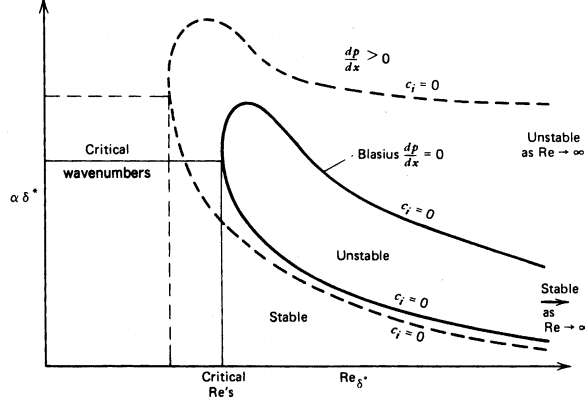


Figure 5.8: General shape of the neutral stability curve for a Blasius boundary layer and for layers with adverse pressure gradient (Panton, 2005).

slip surface is the sheet vortex of uniform density. The stability analysis includes finding perturbations of the velocity potential in the uniform streams. The pressure perturbations and normal velocities of particles at the disturbed interface are to be equal on both sides. These conditions lead to a simple result for the complex phase velocity

$$c = \frac{1}{2}(U_1 + U_2) \pm \frac{i}{2}|U_2 - U_1| \quad (5.25)$$

Sign “+” in equation (5.25) corresponds to unstable mode. The result means that sheet vortex is unstable. This is the Kelvin-Helmholtz instability (see [Bat03, Pan05]). Computational studies of mixing layers demonstrate that the finite thickness  $\delta \approx \lambda$  stabilizes the flow. However, the flow is always unstable in the limit  $\lambda \gg \delta$  when  $U_1 \neq U_2$ .

### 5.2.6 Three-dimensional perturbations

The normal mode analysis in the case of three-dimensional perturbations includes dependence on the spanwise coordinate  $z$ . Three velocity components and pressure perturbations are sought in the form

$$(u', v', w', p') = (\tilde{u}, \tilde{v}, \tilde{w}, \tilde{p}) \exp(i\alpha x + i\beta z - i\omega t) \quad (5.26)$$

After substitution of (5.26) into linearized Navier-Stokes equations, one can derive a system of ODEs for the amplitude functions  $(\tilde{u}, \tilde{v}, \tilde{w}, \tilde{p})$  similar to equation (5.5). One can also derive one ODE of the fourth order for the amplitude function  $\tilde{v}$ :

$$(U - c)(\tilde{v}'' - (\alpha^2 + \beta^2)\tilde{v}) - \tilde{v}U'' = \frac{1}{i\alpha \text{Re}_{\delta 3D}} \left( \tilde{v}^{iv} - 2(\alpha^2 + \beta^2)\tilde{v}'' + (\alpha^2 + \beta^2)^2\tilde{v} \right) \quad (5.27)$$

[Squ33] found that one can transform the equation into the form of an Orr-Sommerfeld equation for two-dimensional disturbances:

$$\alpha_{2D} = \sqrt{\alpha^2 + \beta^2}, \quad \alpha_{2D} \text{Re}_{\delta 2D} = \alpha \text{Re}_{\delta 3D} \quad (5.28)$$

Transformation (5.28) is the Squire transformation leading to the two-dimensional form of the Orr-Sommerfeld equation:

$$(U - c) (\tilde{v}'' - \alpha_{2D}^2 \tilde{v}) - \tilde{v} U'' = \frac{1}{i \alpha_{2D} \text{Re}_{\delta 2D}} (\tilde{v}^{iv} - 2 \alpha_{2D}^2 \tilde{v}'' + \alpha_{2D}^4 \tilde{v}) \quad (5.29)$$

Using the temporal framework of the stability analysis, one can say the following about three-dimensional perturbations ([Squ33]): “if any velocity profile is unstable for a particular value of Reynolds’ number, it will be unstable at a lower value of Reynolds’ number for two-dimensional disturbances.” Squire’s transformation does not have a straight-forward spatial formulation; it leads to complex values of  $\text{Re}_{\delta 2D}$  that defy simple physical interpretation. And, in fact, one can find (at low frequencies) that the lower branch of the neutral curve for three-dimensional perturbations can be shifted upstream with respect to the neutral curve for two-dimensional perturbations. However, the overall amplification of two-dimensional disturbances is larger than the amplification of the three-dimensional perturbations having the same frequency. Although the fact is often interpreted as a result of the Squire transformation, this is not quite correct. In contrast, three-dimensional disturbances are more amplified in supersonic boundary layers.

### 5.3 Receptivity of boundary layers

Having introduced the normal modes concept in section 5.2.1, we pointed out that the analysis of the normal modes is missing a link with the PDEs and the physical initial and boundary value problem. In other words, the normal mode analysis substitutes solving a real physical problem with studies of some elements of the bases (eigenfunctions), omitting a discussion of what their weights might be in a physical setup. (This problem is often called the receptivity problem). It had been understood by the mid-1970s that the instability of flow is only one element of the laminar-turbulent transition scenario. [Mor69] and [Res76] clarified the important role of the receptivity problem in the laminar-turbulent transition process. These papers motivated intensive investigations of various mechanisms responsible for the excitation of unstable TS waves. The vast bibliography on the topic is presented in [Cho98, SRK02, CJJ67, Fed03]; and [Tum06b, Tum07]. For our further discussion it is important to keep in mind that the receptivity issue is a significant element in the formulation of a physics-based transition prediction.

### 5.4 Paths to turbulence in wall layers

Before a discussion of possible scenarios for laminar-turbulent transition, we have to point out that the previous sections were aimed at modes that can be unstable and lead to the transition. However, this concept is not adequate for the whole spectrum of experimental observations. For example, the Couette flow and Hagen-Poiseuille flow in a circular pipe are stable, though one can observe in experiments a laminar-turbulent transition in these flows.

There are also examples when a transition to turbulent flow can be triggered at Reynolds numbers lower than the critical value predicted by the stability theory. These observations indicate that there are other routes in transition to turbulence aside from amplification of the instability modes. One of the possible mechanisms of transition to turbulence is associated with the transient growth phenomenon.

Small perturbations in a stable shear flow can have a significant transient amplification before they die out in accordance with the stability theory prediction. A pair of counter-rotating streamwise vortices in a boundary layer illustrates the transient growth phenomenon. The vortices redistribute the streamwise momentum by lifting up slow fluid particles from the wall and bringing down the high-speed particles toward the wall. Although the streamwise vortices decay downstream, the cumulative effect of the momentum redistribution can be significant, and one can observe the streaky structures in boundary layers. In turn, the transiently growing perturbations can lead to a flow structure that is unstable with respect to other small perturbations, serving as a path to turbulence without the presence of unstable modes (non-modal path to transition). One can find bibliographies on theoretical studies of this phenomenon in [SH01], and [ZTR06]. The transient growth phenomenon can be observed in experiments with an array of roughness elements placed on the wall ([Whi02, FBTC04, WRE05, EW06, DW08]). The transient growth phenomenon has been studied extensively using theoretical, experimental, and computational methods in recent years because of its potential application for transition prediction ([Res01, RT04, RT06]).

Professor E. Reshotko ([RT06]) analyzed possible paths in transition to turbulence and summarized the contemporary understanding in the diagram shown in figure 5.9. It is important to point out that the path to turbulence depends on the level of external disturbances. Depending on the environment (noisy wind tunnel, flight in a quiet atmosphere, flow in a turbine etc), different paths can have different values at particular conditions, and a physics-based transition prediction has to take into account the variety of mechanisms.

Despite the variety of the transition mechanisms, they all lead to nonlinear flow dynamics at the final stage of the flow breakdown. Historically, the following transition scenarios have been distinguished: the K-regime (after [KTS62]), the subharmonic- (also known as N- or H-) regime discovered by [KKL77], and the oblique transition studied by [FTB93, BLH94], and others. Discussions of the nonlinear mechanisms in transition scenarios can be found in [Kac94], and [SH01]. Recent experimental and computational studies indicate that these different mechanisms are the same at the late stages of the transition ([SFK00]). Experiments in a circular pipe flow ([HTW00]) also demonstrate that the late stage of transition is similar to transition in boundary layers.

## 5.5 Transition prediction: modal growth scenario (path A)

The laminar-turbulent transition depends on many factors, and prediction of the “transition point” is a challenging task. Because the phenomenon depends on external forcing (free

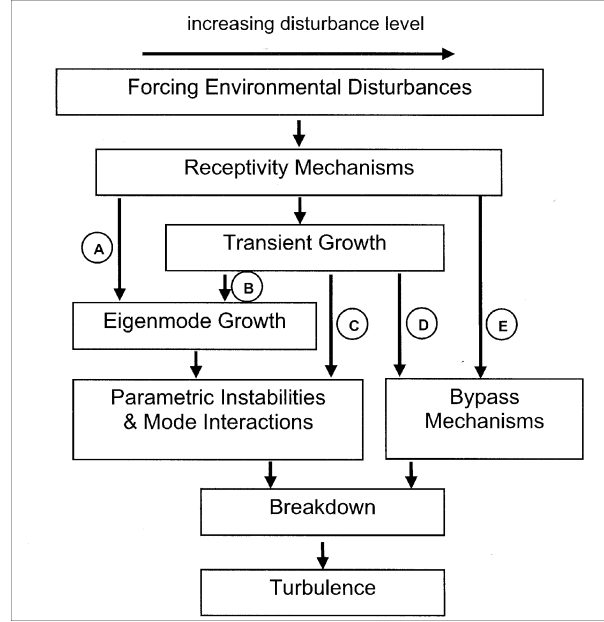


Figure 5.9: Paths to turbulence in wall layers (Reshotko and Tumin, 2006).

stream turbulence, acoustic noise, roughness induced perturbations etc), transition prediction suffers uncertainty related to the flow conditions. The level of perturbations (and their spectrum) in wind tunnels might be different from flight conditions, and one cannot use wind tunnel experiments for transition prediction in a flight. However, if the transition path is determined, one can work on a physics-based transition prediction method. Consider transition on a smooth surface due to low-level free stream perturbations (path A in figure 5.9). The main stages of the transition are: receptivity, linear amplification of TS waves, and nonlinear breakdown. As follows from experiments in quiet wind tunnels and their comparisons with the linear stability theory, a significant part of the transition region can be described by the linear stability theory, and the length of the nonlinear region is relatively short. Comparison of experimental data with the theoretical results (see, for example, [ZT87]) indicates that the nonlinear dynamics of perturbations become significant when the velocity of the perturbation achieves about 1% of the free stream velocity. Therefore, one can assume that there is a threshold amplitude  $\varepsilon_*$  associated with the laminar-turbulent transition (amplitude criterion of transition). Let's assume that we know the spectrum of the free stream perturbations,  $\varepsilon_\infty(f)$ , and the receptivity coefficient  $K(f)$  such that the amplitude of the unstable wave at the neutral point,  $x_{np}$ , can be found as  $\varepsilon_{TS}(f) = K(f)\varepsilon_\infty(f)$ . The linear amplification of the perturbation can be predicted by the factor  $\exp(-\int_{x_{np}}^x \alpha_i dx)$ . Therefore, the “transition point,”  $x_{tr}$  can be estimated from the amplitude criterion:

$$\varepsilon_* = K(f)\varepsilon_\infty(f) \exp(-\int_{x_{np}}^{x_{tr}} \alpha_i dx) \quad (5.30)$$

Equation (5.30) can be recast as follows:

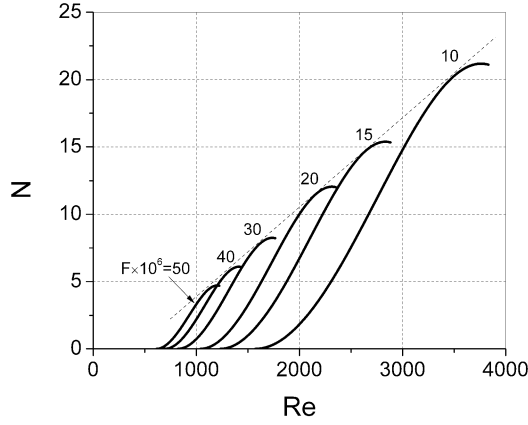


Figure 5.10:  $N$ -factors for the Blasius boundary layer flow (quasi-parallel flow approximation).

$$N(x_{tr}) = \ln \left[ \frac{\varepsilon_*}{K(f)\varepsilon_\infty(f)} \right] \quad (5.31)$$

$$N(x_{tr}) \equiv - \int_{x_{np}}^{x_{tr}} \alpha_i dx$$

Because the effects of the unknown factors,  $K(f)\varepsilon_\infty(f)$ , are smoothed by the logarithm, one can try to correlate  $N(x_{tr})$  for different flow conditions (noisy/quiet wind tunnels, flight, etc). This is the underlying concept of the  $e^N$  method transition prediction ([vI56, Smi59]). Figure 5.10 illustrates the  $N$ -factors for the Blasius boundary layer in the quasi-parallel approximation.

Because the nonparallel flow effect can have a significant impact on the growth rate, the contemporary applications of the  $e^N$  method are based on the Parabolized Stability Equations (PSE) introduced by [HB87] (see also [Ber91, Her97]). In the PSE method, one has to solve a system of parabolized equations using a downstream marching algorithm. The approach allows capturing the nonparallel flow effects in the leading term without additional steps as required in the method of multiple scales. The reader can find a bibliography and examples on the  $e^N$  method's application in [HLRA96, JC99, JC05]; [AC00, SRW03, CCN01]; [Cha03, Cha04]; and [CC05].

## 5.6 Conclusion

This brief discussion demonstrates that transition to turbulence is a complex phenomenon. It depends on a variety of factors (free-stream disturbances, perturbations originated on the wall etc) that might be beyond our control. Therefore, the designer of laminarized aircrafts

has to deal with the uncertainties and to distinguish different mechanisms responsible for the flow transition.

# Chapter 6

## Toward the foundation of a global (bi-global) modes concept

This section is based on the invited talk at the fourth symposium on Global Flow Instability and Control [Tum09].

### 6.1 Introduction

Recent progress in using global (bi-global) modes for the analysis of a variety of complex (and “simple”) flows led to their applications in flow control. The progress in computational capabilities brings this advanced technique to common practice in studies of flow perturbations [The03, EG05, ÅEGH08, RT08, BÅBH09, BHHS09]. However, the formulation of global eigenvalue problems is accompanied by some uncertainties in the choice of boundary conditions over a 2D domain. The choice of boundary conditions has a heuristic nature, and this provokes questions regarding the suitable formulation of the eigenvalue problems. In this note, I would like to suggest a simple model that can help us understand the effect of the upstream and downstream boundary conditions on the eigenvalues and eigenfunctions, and possible limitations of the global formulation. Originally, my idea was to link the global stability analysis of simple flows (such as a flat plate boundary layer) with the conventional quasi-parallel analysis based on the Orr-Sommerfeld equation. The analysis of a weakly non-parallel flow has been carried out in [ÅEGH08]. A comprehensive analysis of the upstream and downstream boundary conditions’ effect on the spectrum of parallel boundary-layer flow was carried out in [RT08]. These explorations shed some light onto the representation of discrete TS modes within the “box formulation.” However, because the underlying complexity of the 2D eigenvalue problem demands significant computational power, there is a lack of understanding of the qualitative features of this advanced formulation. As we know, the initial-value problem in a parallel boundary layer flow can be presented as an expansion into normal modes of discrete and continuous spectra [Gus79, SG81]. What can happen when we approach the problem using the “box formulation”? What can we get rid of completely, and what are possible constraints on the perturbations under consideration?



## 6.2 A model

To make the model as transparent as possible, I suggest beginning with the initial-value problem in a uniform incompressible flow ( $U_\infty = \text{const}$ ). The solution of this problem can be found analytically using the Laplace transform in time and Fourier transform in  $x$ - and  $y$ - directions. There are no discrete normal modes, and the solution can be presented as an expansion into the vorticity modes of the continuous spectrum. For a given streamwise wave number,  $\alpha$ , and transversal wave number,  $k$ , the vorticity modes have complex frequency  $\omega = \alpha - i(k^2 + \alpha^2)/R$ , where  $R$  is the Reynolds number based on the free stream velocity,  $U_\infty$ , and on the appropriate length scale  $L$ . Let's address the known problem using the "box formulation" for a 2D domain:  $x = [-L_x, L_x], y = [-L_y, L_y]$ . It is still a challenging problem if we use advanced computational tools to shed some qualitative light onto the effect of the boundary conditions on the 2D normal modes. In order to elucidate the features of using the "box formulation", let's consider a case when  $L_y \gg L_x$ . In the limit of the "tall" box, we arrive at a consideration of the strip  $x = [-1, 1], y = (-\infty, +\infty)$  ( $L_x$  is the length scale). The limit allows Fourier transform in  $y$  similarly to analysis in [Tum03], in which the strip of uniform flow with inhomogeneous upstream and downstream boundary conditions for perturbations was considered. Here, we use the same model of perturbations in a strip of uniform flow, but we formulate homogeneous boundary conditions at  $x = -1$ , and  $x = +1$ .

The linearized Navier-Stokes equations can be written in the matrix-vector form:

$$ik\mathbf{A} - i\omega\mathbf{H}_t\mathbf{A} = \mathbf{H}_1\mathbf{A} + \mathbf{H}_2\frac{d\mathbf{A}}{dx},$$

where  $\mathbf{H}_t, \mathbf{H}_1$ , and  $\mathbf{H}_2$  are  $4 \times 4$  matrices. Vector  $\mathbf{A} = (u, p, v, \Omega)^T$  is comprised of the pressure perturbation  $p$ ,  $x$ - and  $y$ - velocity components  $u$  and  $v$ , respectively;  $\Omega = \partial u / \partial y - \partial v / \partial x$ . The solution of the system of ODEs with constant coefficients can be written in the form:

$$\mathbf{A} = \sum_{j=1}^4 C_j \mathbf{Z}_j \exp(\lambda_j x), \text{ where}$$

$$\begin{aligned} \lambda_1 = -k, \lambda_2 = k, \lambda_3 = \frac{1}{2} \left( R - \sqrt{4k^2 + R^2 - 4iR\omega} \right), \lambda_4 = \frac{1}{2} \left( R + \sqrt{4k^2 + R^2 - 4iR\omega} \right), \\ \mathbf{Z}_1 = \left( i, -i\frac{k+i\omega}{k}, 1, 0 \right)^T, \mathbf{Z}_2 = \left( -i, i\frac{k-i\omega}{k}, 1, 0 \right)^T, \\ \mathbf{Z}_3 = \left( \frac{2ik}{-R + \sqrt{4k^2 + R^2 - 4iR\omega}}, 0, 1, \frac{R(R - 2i\omega - \sqrt{4k^2 + R^2 - 4iR\omega})}{-R + \sqrt{4k^2 + R^2 - 4iR\omega}} \right)^T, \\ \mathbf{Z}_4 = \left( -\frac{2ik}{R + \sqrt{4k^2 + R^2 - 4iR\omega}}, 0, 1, -\frac{R(R - 2i\omega + \sqrt{4k^2 + R^2 - 4iR\omega})}{R + \sqrt{4k^2 + R^2 - 4iR\omega}} \right)^T. \end{aligned}$$

The first and the second fundamental solutions can be interpreted as "pressure waves" (they have zero vorticity and non-zero pressure). The third and the fourth fundamental solutions can be interpreted as "vorticity waves" (they have zero pressure and non-zero vorticity). The

coefficients  $C_j$  are determined from the boundary conditions. The box formulation delivers the pressure perturbation. The downstream and upstream pressure waves are localized within the layers having an order of magnitude  $\sim 1/|k|$ . In order to have a reasonable approximation of the unbounded domain, one has to consider perturbations having the characteristic scale  $l_y \ll 1$ , and to keep in mind that the solution is affected by the boundary conditions within the layers  $x \approx [-1, -1 + l_y]$  and  $x \approx [1 - l_y, 1]$ . At finite  $k$  and  $R \gg 1$ , one can find:

$$\lambda_3 \approx i\omega - \frac{k^2 + \omega^2}{R}, \quad \lambda_4 \approx R - i\omega.$$

The third fundamental solution represents a vorticity mode propagating with the flow and slowly decaying due to the viscosity. The fourth fundamental solution represents a vorticity perturbation stemming from the right boundary ( $x = 1$ ) and localized within the layer of thickness  $O(1/R)$ .

### 6.3 An example of “global” modes with the Dirichlet boundary conditions

Consider an example of the boundary conditions:

$$u(-1) = v(-1) = 0; \quad u(1) = v(1) = 0.$$

Homogeneous boundary conditions lead to a dispersion relation  $\omega = \omega(R, k)$ . The dispersion relation can be written in the form:

$$\begin{aligned} \Delta(k, R, \omega) = & -2k\sqrt{4k^2 + R^2 - 4iR\omega}\cosh(R) + \\ & k\sqrt{4k^2 + R^2 - 4iR\omega}\cosh\left(2k - \sqrt{4k^2 + R^2 - 4iR\omega}\right) + \\ & k\sqrt{4k^2 + R^2 - 4iR\omega}\cosh\left(2k + \sqrt{4k^2 + R^2 - 4iR\omega}\right) + \\ & 2(-2k^2 + iR\omega)\sinh(2k)\sinh\left(\sqrt{4k^2 + R^2 - 4iR\omega}\right) = 0 \end{aligned}$$

The eigenvalues can be found as roots of  $\Delta(k, R, \omega) = 0$ . One can also approach the problem directly by using the spectral collocation method (SCM) for the system of ODEs. Figure 6.1 illustrates the spectrum when parameter  $k$  is varied (obtained using Mathematica) and results obtained using SCM at  $k = 2$  and 5.

It is worth mentioning that the lines in Fig. 6.1 are skewed at their tips similarly to global spectra [see Fig. 2 in [ÆEGH08]]. In the unbounded domain, the continuous spectrum represented by the vorticity modes corresponds to a straight line in the complex plane  $\omega$ . In the case of the box formulation, the tips of the modes correspond to small  $k$ , and they are affected by the boundary conditions. Figure 6.2 illustrates streamwise velocity perturbation in mode 2,  $k = 5$ . It is tempting to say that the temporal global modes also reflect the spatial amplification, but such a statement apparently is irrelevant to the physical problem, and is a pure effect of the downstream boundary condition.

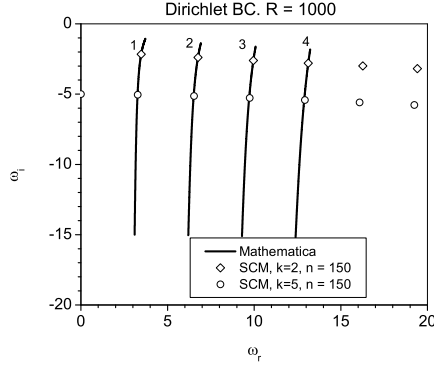


Figure 6.1: Comparison of SCM results with results obtained using Mathematica.

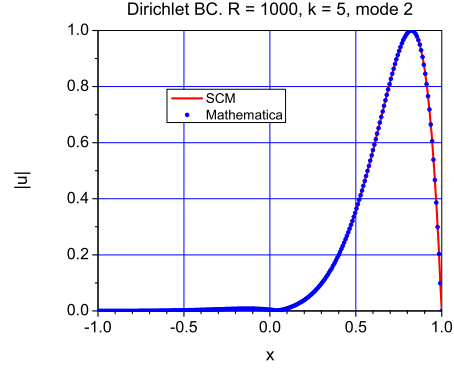


Figure 6.2: Streamwise velocity perturbation in mode 2,  $k = 5$ .

## 6.4 Preliminary conclusions

1. Assuming that the 2D eigenvalue problem leads to a complete set of eigenfunctions, we should not discuss how “wrong” or “correct” the boundary conditions are in the “box formulation.” The discussion should address the appropriateness of the set of eigenfunctions for the specific problem.
2. The “box formulation” introduces artifacts such as upstream pressure and vorticity waves. There is a boundary layer within the downstream boundary of the domain. The pressure wave penetrates upstream at a distance of approximately the characteristic scale of the perturbation in the  $y$  direction. In order to have the physical picture unaffected by the boundary conditions, size of the box should be chosen depending on the typical scales of the perturbations under consideration.
3. The spatial growth of velocity perturbation within a global mode does not necessarily mean that the mode captures a spatial amplification associated with the convective instability.

# Chapter 7

## Conclusions

A comprehensive study of stability of hypersonic boundary layers has been carried out under the support from the Air Force Office of Scientific Research, USAF under grant FA9550-08-1-0332 monitored by Dr. J. D. Schmisser.

The main results of the project:

- The multimode decomposition technique may serve as a tool for gaining insight into the flow dynamics in the presence of perturbations belonging to different modes. In the past, one could compare DNS results with theoretical prediction for the unstable mode only far downstream from an actuator where the unstable mode dominates the total signal. Using the biorthogonal eigenfunction system, one can compare DNS results with theoretical predictions for the unstable and stable modes in the vicinity of the actuator as well.
- In Ref. [TWZ07] and in the present work, we have found that the multimode decomposition requires a more elaborate analysis within the point of synchronism of mode F with the continuous spectrum. Therefore, an extension of the theoretical model of Ref. [FK01] to the case of continuous spectrum is required.
- The structure of the discrete spectrum in stability analysis of high-speed boundary layers depends on basic flow parameters such as the Mach number, Prandtl number, Reynolds number etc. The spectrum may have two unstable modes that are easily associated with inviscid instabilities of Macks first and second modes. With another choice of the basic parameters, the spectrum may have only one unstable mode having two maxima of the growth rate.
- Terminology introduced by Mack [Mac69] using modes 1 and 2 (the well-known first and second modes) is inconsistent with a proper mathematical treatment of normal modes. Macks family of solutions is actually what should be called a normal mode, whereas his definitions of first-mode amplified solutions and second-mode amplified/damped

solutions lead to confusion when normal modes are used to represent a solution of the linearized Navier-Stokes equations.

- The considered examples of boundary layer flows in binary mixtures of oxygen and nitrogen indicate that the real gas effects stabilize the first mode and destabilize the second one in the inviscid limit of the stability equations (see [FT10] regarding the terminology). The result is in agreement with [MA91] where this observation was made for boundary layer flow for air in chemical and thermal equilibrium with the stability equations including the effect of viscosity, diffusivity, and thermal conductivity. Real gas effects lead to a decrease in wall temperature and can have an impact on the perturbations similar to the wall cooling effect in boundary layers of non-reacting, calorically perfect gases. However, such an interpretation of the wall temperature effect might be misleading when binary mixtures of nitrogen and oxygen are compared. In the considered example, nitrogen does not experience significant dissociation, whereas oxygen goes through dissociation. The difference leads to qualitative differences in the specific heats, and the second mode in nitrogen is more unstable than the second mode in oxygen in spite of the higher wall temperature.
- The “box formulation” used in global (bi-global) stability analysis introduces artifacts such as upstream pressure and vorticity waves. There is a boundary layer within the downstream boundary of the domain. The pressure wave penetrates upstream at a distance of approximately the characteristic scale of the perturbation in the  $y$  direction. In order to have the physical picture unaffected by the boundary conditions, size of the box should be chosen depending on the typical scales of the perturbations under consideration.

# Appendix A

## Appendices to Chapter 2

- A.1 Comparison of DNS mean velocity and temperature profiles with the self-similar solution. Comparison of eigenvalues  $\alpha = \alpha_r + i\alpha_i$  obtained using DNS and self-similar profiles.

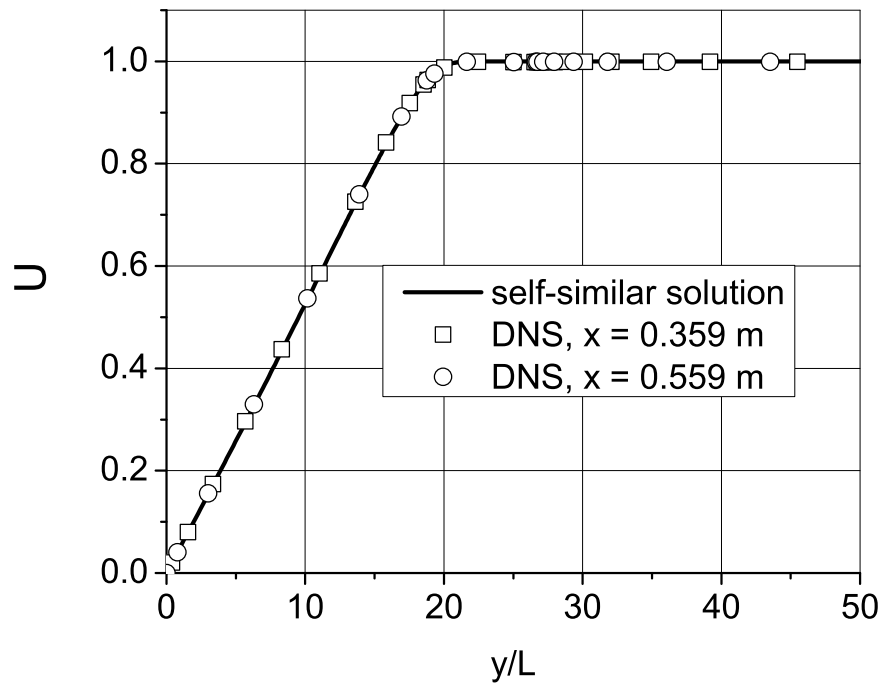


Figure A.1: Self-similar solution (solid line) and DNS results (symbols) for the mean velocity profile  $U(y)$ .

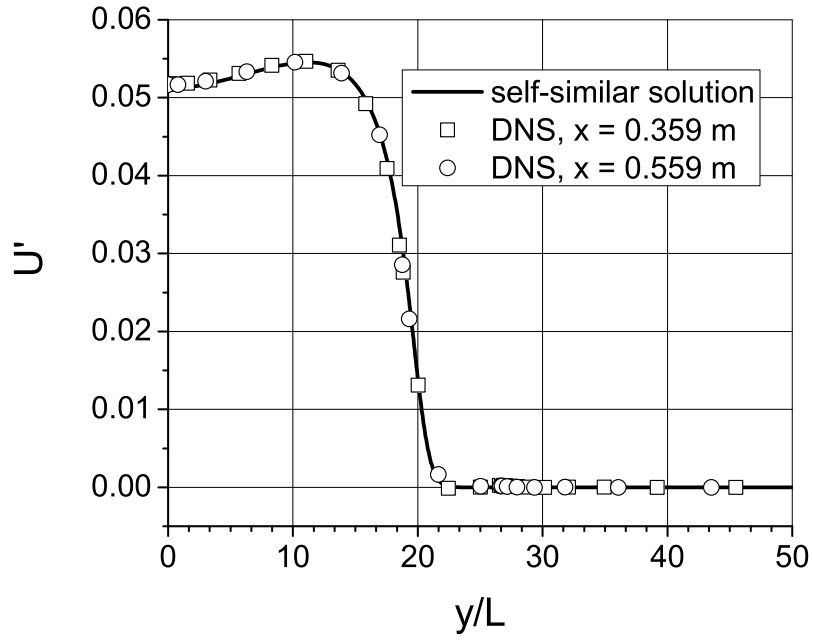


Figure A.2: Derivative  $dU/dy$ : solid line - self-similar solution, symbols - DNS.

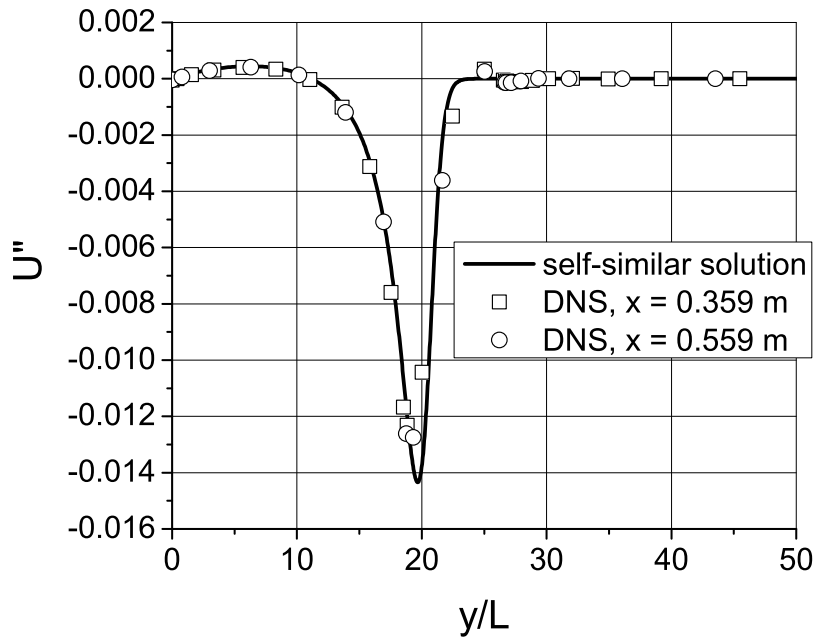


Figure A.3: Derivative  $d^2U/dy^2$ : solid line - self-similar solution, symbols - DNS.



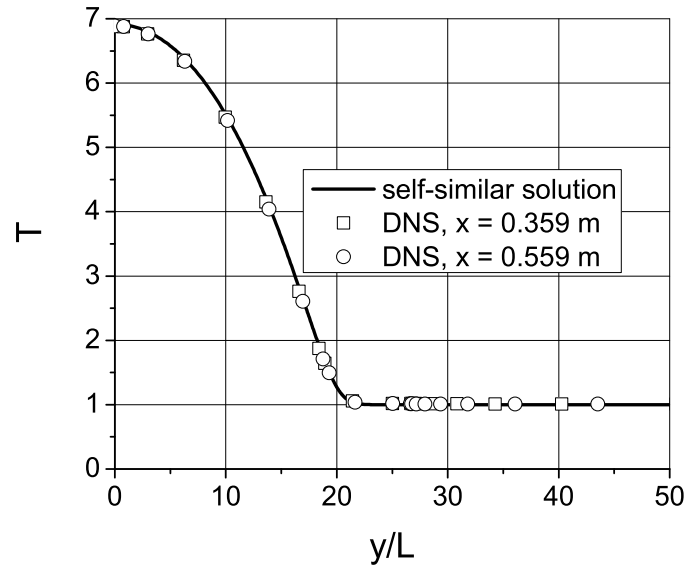


Figure A.4: Mean temperature profile  $T(y)$ : solid line - self-similar solution, symbols - DNS.

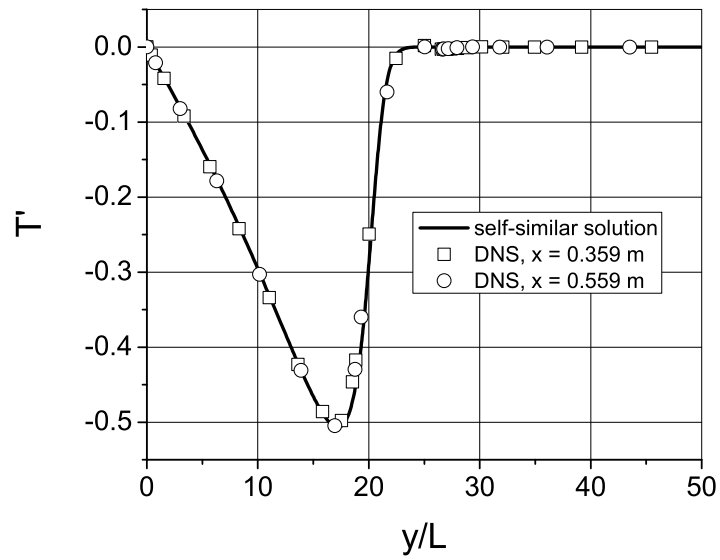


Figure A.5: Derivative  $dT/dy$ : solid line - self-similar solution, symbols - DNS.

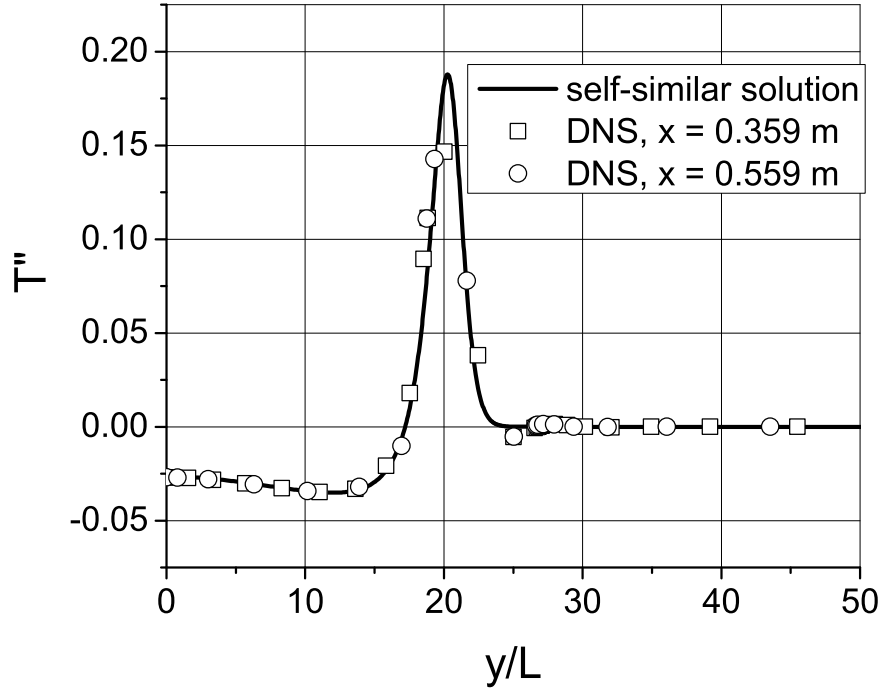


Figure A.6: Derivative  $d^2T/dy^2$ : solid line - self-similar solution, symbols - DNS.

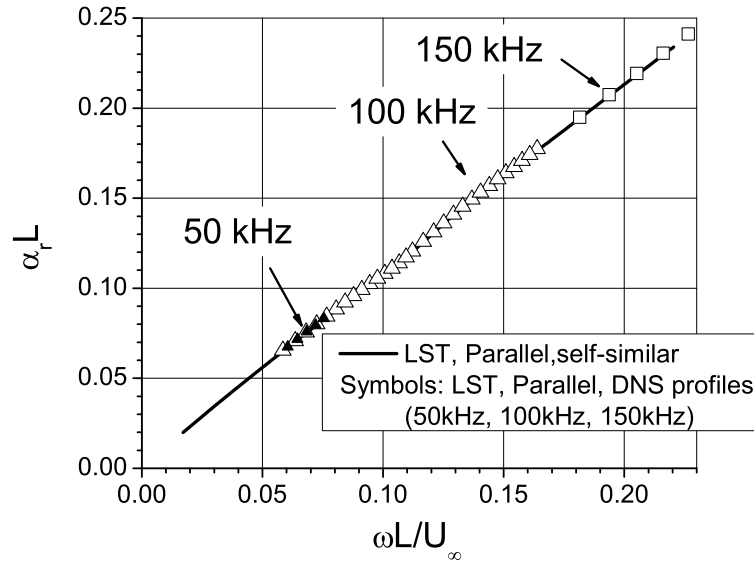


Figure A.7: Comparison of  $\alpha_r$  obtained using DNS and self-similar velocity and temperature profiles. Solid line - self-similar profiles; symbols - DNS profiles.

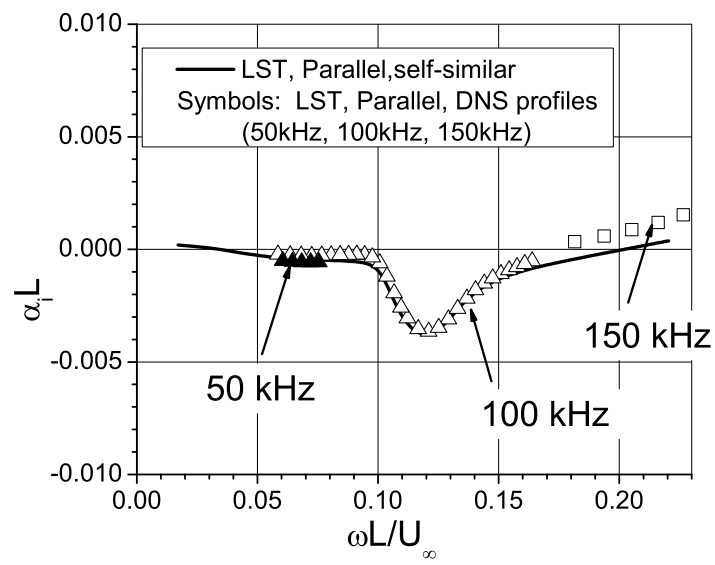


Figure A.8: Comparison of  $\alpha_i$  obtained using DNS and self-similar velocity and temperature profiles. Solid line - self-similar profiles; symbols - DNS profiles.

# Bibliography

- [AC00] D. Arnal and G. Casalis. Laminar-turbulent transition prediction in three-dimensional flows. *Prog. Aero. Sci.*, 36:173–191, 2000.
- [ÅEGH08] E. Åkervik, U. Ehrenstein, F. Gallaire, and D. S. Henningson. Global two-dimensional stability measures of the flat plate boundary-layer flow. *European J. Mech. B/Fluids*, 27:501–513, 2008.
- [AR90] D. Ashpis and E. Reshotko. The vibrating ribbon problem revisited. *J. Fluid Mech.*, 213:531–547, 1990.
- [BÅBH09] S. Bagheri, E. Åkervik, L. Brandt, and D. S. Henningson. Matrix-free methods for stability and control of boundary layers. *AIAA J.*, 47:1057–1068, 2009.
- [Bat03] G. K. Batchelor. *An introduction to fluid dynamics*. Cambridge University Press, 2003.
- [Ber91] F. P. Bertolotti. *Linear and nonlinear stability of boundary layers with streamwise varying properties*. Phd thesis, Ohio State University, 1991.
- [Ber98] F. P. Bertolotti. The influence of rotational and vibrational energy relaxation on boundary-layer stability. *J. Fluid Mech.*, 372:93–118, 1998.
- [BHHS09] S. Bagheri, D. S. Henningson, J. Høpfner, and P. J. Schmid. Input-output analysis and control design applied to a linear model of spatially developing flows. *Appl. Mech. Reviews*, 62:020803–1 – 020803–27, 2009.
- [BLH94] S. Berlin, A. Lundbladh, and D. S. Henningson. Spatial simulations of oblique transition. *Phys. Fluids*, 6:1949–1951, 1994.
- [BM92] P. Balakumar and M. R. Malik. Discrete modes and continuous spectra in supersonic boundary layer. *J. Fluid Mech.*, 239:631–656, 1992.
- [Bou72] M. Bouthier. Stabilité linéaire des écoulements presque parallèles. *J. de Mécanique*, 11(4):599–621, 1972.
- [BS81] R. J. Bodonyi and F. T. Smith. The upper branch stability of the Blasius boundary layer, including non-parallel flow effects. *Proc. Roy. Soc., Series A*, 375:65–92, 1981.

- [CC05] C. L. Chang and M. Choudhari. Boundary-layer receptivity and integrated transition prediction. AIAA Paper 2005-0526, 2005.
- [CCN01] J. D. Crouch, I. W. M. Crouch, and L. L. Ng. Estimating the laminar/turbulent transition location in three-dimensional boundary layers for cfd applications. AIAA Paper 2001-2989, 2001.
- [Ceb99] T. Cebeci. *An Engineering Approach to the Calculation of Aerodynamic Flows*. Springer, 1999.
- [Cha03] C. L. Chang. The langley stability and transition analysis code (lastrac): Lst, linear & nonlinear pse for 2-d, axisymmetric, and infinite swept wing boundary layers. AIAA Paper 2003-974, 2003.
- [Cha04] C. L. Chang. Lastrac.3d: transition prediction in 3d boundary layers. AIAA Paper 2004-2542, 2004.
- [Cho98] M. Choudhari. Receptivity. In R. W. Johnson, editor, *The Handbook of Fluid Dynamics*, pages 13-25 – 13-40. CRC Press, 1998.
- [CJJ67] W. O. Criminale, T. L. Jackson, and R. D. Joslin. *Theory and computation in hydrodynamic stability*. Cambridge University Press, 1967.
- [CM93] C.-L. Chang and M. R. Malik. Non-parallel stability of compressible boundary layers. AIAA Paper 93-2912, 1993.
- [CVM97] C. L. Chang, H. Vinh, and M. R. Malik. Hypersonic boundary-layer stability with chemical reactions. AIAA Paper 1997-2012, 1997.
- [Dor62] W. H. Dorrance. *Viscous Hypersonic Flow*. McGraw-Hill, 1962.
- [DR81] P. G. Drazin and W. H. Reid. *Hydrodynamic Stability*. Cambridge University Press, 1981.
- [DW08] N. A. Denissen and E. B. White. Roughness induced bypass transition revisited. *AIAA J.*, 46:1874-1877, 2008.
- [DW09] N. A. Denissen and E. B. White. Continuous spectrum analysis of roughness-induced transient growth. *Phys. Fluids*, 21, 2009. paper 114105.
- [Eag69] P. M. Eagles. Composite series in the orr-sommerfeld problem. *Quart. J. Mech. and Appl. Math.*, 22:129-182, 1969.
- [EFS06] I. V. Egorov, A. V. Fedorov, and V. G. Soudakov. Numerical modeling of the receptivity of a supersonic boundary layer to acoustic disturbances. *Fluid Dynamics*, 41(1):37-48, 2006. Translated from *Izvestiya Rossiiskoi Akademii Nauk, Mekhanika Zhidkosti i Gaza*, No. 1, 2006.

- [EFS08] I. V. Egorov, A. V. Fedorov, and V. G. Soudakov. Receptivity of a hypersonic boundary layer over a flat plate with a porous coating. *J. Fluid Mech.*, 601:165–187, 2008.
- [EG05] U. Ehrenstein and F. Gallaire. On two-dimensional temporal modes in spatially evolving open flows: the flat plate boundary layer. *J. Fluid Mech.*, 536:209–218, 2005.
- [EH80] N. M. El-Hady. On the stability of three-dimensional, compressible nonparallel boundary layers. AIAA Paper 80–1374, 1980.
- [EW06] F. G. Ergin and E. B. White. Unsteady and transitional flows behind roughness elements. *AIAA J.*, 44:2504–2514, 2006.
- [FA03] A. Fedorov and A. Tumin. Initial-value problem for hypersonic boundary layer flows. *AIAA J.*, 41:379–389, 2003.
- [FBTC04] J. H. M. Fransson, L. Brandt, A. Talamelli, and C. Cossu. Experimental and theoretical investigation of the non-modal growth of steady streaks in a flat plate boundary layers. *Phys. Fluids*, 16:3627–3638, 2004.
- [FC04] P. Fischer and M. Choudhari. Numerical simulation of roughness-induced transient growth in a laminar boundary layer. AIAA Paper 2004–2539, 2004.
- [Fed03] A. V. Fedorov. Receptivity of a high-speed boundary layer to acoustic disturbances. *J. Fluid Mech.*, 491:101–129, 2003.
- [Fed11] A. V. Fedorov. Transition and stability of high-speed boundary layers. *Annu. Rev. Fluid Mech.*, 43:79–85, 2011.
- [FK01] A. V. Fedorov and A. P. Khokhlov. Prehistory of instability in a hypersonic boundary layer. *Theor. Comp. Fluid Dyn.*, 14:359–375, 2001.
- [FK02] A. V. Fedorov and A. P. Khokhlov. Receptivity of hypersonic boundary layer to wall disturbances. *Theor. Comp. Fluid Dyn.*, 15:231–254, 2002.
- [Flo91] J. M. Floryan. On the görtler instability of boundary layers. *Prog. Aerospace Sci.*, 28:235–271, 1991.
- [Fri90] B. Friedman. *Principles and Techniques of Applied Mathematics*. Dover Publications, 1990.
- [FT05] E. Forgoston and A. Tumin. Initial-value problem for three-dimensional disturbances in a hypersonic boundary layer. *Phys. Fluids*, 17, 2005. paper No. 084106.
- [FT10] A. Fedorov and A. Tumin. Branching of discrete modes in high-speed boundary layers and terminology issues. AIAA Paper 2010–5003, 2010.

- [FT11] A. Fedorov and A. Tumin. High-speed boundary-layer instability: Old terminology and a new framework. *AIAA J*, 2011.
- [FTB93] H. Fasel, A. Thumm, and H. Bestek. Direct numerical simulation of transition in supersonic boundary layer: Oblique breakdown. In L. D. Kral and T. A. Zang, editors, *Transitional and turbulent compressible flows*, pages 77–92. FED, ASME No. 151, 1993.
- [Gap80] S. A. Gaponov. Influence of nonparallel flow on the development of disturbances in a supersonic boundary layer. *Fluid Dynamics*, 15:195–199, 1980.
- [Gas74] M. Gaster. On the effects of boundary layer growth on flow stability. *J. Fluid Mech.*, 66:465–480, 1974.
- [GF] V. R. Guschin and A. V. Fedorov. Qualitative properties of the instability of currents at a wall in the presence of a flow at high supersonic speeds. Technical Report NASA-TT-20683.
- [GF89] V. R. Guschin and A. V. Fedorov. Short-wave instability in a perfect-gas shock layer. *Fluid Dynamics*, 24(1):7–10, 1989. Translated from *Izvestiya Akademii Nauk SSSR, Mekhanika Zhidkosti I Gaza*, No. 1, January-February 1989, pp. 10-14.
- [GF90] V. R. Guschin and A. V. Fedorov. Excitation and development of unstable disturbances in supersonic boundary layer. *Fluid Dynamics*, 25(3):344–352, 1990. Translated from *Izvestiya Akademii Nauk SSSR, Mekhanika Zhidkosti I Gaza*, No. 3, May-June 1990, pp. 21-29.
- [Gra66] W. P. Graebel. On determination of the characteristic equations for the stability of parallel flows. *J. Fluid Mech.*, 24:497–508, 1966.
- [GT04] P. Gaydos and A. Tumin. Multimode decomposition in compressible boundary layers. *AIAA J.*, 42:1115–1121, 2004.
- [Gus79] L. H. Gustavsson. Initial-value problem for boundary layer flows. *Phys. Fluids*, 22:1602–1605, 1979.
- [GYTL90] R. N. Gupta, J. M. Yos, R. A. Thompson, and K. P. Lee. A review of reaction rates and thermodynamic and transport properties for an 11 species air model for chemical and thermal nonequilibrium calculations to 30 000 k. NASA Reference Publication 1232, 1990.
- [HB87] T. Herbert and F. B. Bertolotti. Stability analysis of nonparallel boundary layers. *Bull. Am. Phys. Soc.*, 32:2079, 1987.
- [HCC97] M. L. Hudson, N. Chokani, and G. V. Candler. Linear disturbances in hypersonic, chemically reacting shock layers. *AIAA J.*, 35:958–964, 1997.

- [Her97] T. Herbert. Parabolized stability equations. *Ann. Rev. Fluid Mech.*, 29:245–283, 1997.
- [HLRA96] W. S. Saric H. L. Reed and D. Arnal. Linear stability theory applied to boundary layers. *Ann. Rev. Fluid Mech.*, 28:289–428, 1996.
- [HTW00] G. Han, A. Tumin, and I. Wygnanski. Laminar-turbulent transition in poiseuille pipe flow subjected to periodic perturbation emanating from the wall. part 2. late stage of transition. *J. Fluid Mech.*, 419:1–27, 2000.
- [JC99] H. B. Johnson and G. V. Candler. Pse analysis of reacting hypersonic boundary layer transition. AIAA Paper 1999–3793, 1999.
- [JC05] H. B. Johnson and G. V. Candler. Hypersonic boundary layer stability analysis using pse-chem. AIAA Paper 2005–5023, 2005.
- [JSC98] H. B. Johnson, T. G. Seipp, and G. Candler. Numerical study of hypersonic reacting boundary layer transition on cones. *Phys. Fluids*, 10:2676–2685, 1998.
- [Kac94] Y. S. Kachanov. Physical mechanisms of laminar-boundary-layer transition. *Ann. Rev. Fluid Mech.*, 26:411–482, 1994.
- [KKL77] Y. S. Kachanov, V. V. Kozlov, and V. Y. Levchenko. Nonlinear development of a wave in a boundary layer. *Fluid Dynamics*, 12:383–390, 1977.
- [KTS62] P. S. Klebanoff, K. D. Tidstrom, and L. M. Sargent. The three-dimensional nature of boundary-layer transition. *Phys. Fluids*, 12:1–41, 1962.
- [LL46] L. Lees and C. C. Lin. Investigation of the stability of the laminar boundary layer in a compressible fluid. NACA TN 1115, 1946.
- [LP81] E. M. Lifshitz and L. P. Pitaevskii. *Course of Theoretical Physics*, volume 10. Pergamon Press, 1981.
- [LR62] L. Lees and E. Reshotko. Stability of the compressible laminar boundary layer. *J. Fluid Mech.*, 12:555–590, 1962.
- [LR05] I. J. Lyttle and H. L. Reed. Sensitivity of second-mode linear stability to constitutive models within hypersonic flow. AIAA Paper 2005-0889, 2005.
- [Lyt03] I. J. Lyttle. *Stability of Boundary Layers Within High-Speed Viscous Flows*. Phd thesis, Arizona State University, 2003.
- [MA91] M. R. Malik and E. C. Anderson. Real gas effects on hypersonic boundary-layer stability. *Phys. Fluids A*, 3:803–821, 1991.
- [Mac] L. M. Mack. Boundary layer stability theory: Special course on stability and transition of laminar flow. AGARD Report 709.



- [Mac65] L. M. Mack. Computation of the stability of the laminar compressible boundary layer. *Methods in Computational Physics*, 4:247–299, 1965.
- [Mac69] L. M. Mack. Boundary layer stability theory. JPL Report 900–277, Jet Propulsion Lab., California Institute of Technology, Pasadena, CA, USA, 1969.
- [Mac75] L. M. Mack. Linear stability theory and the problem of supersonic boundary layer transition. *AIAA J.*, 13:278–289, 1975.
- [Mik74] A. B. Mikhailovskii. Theory of plasma instabilities. *Consultants Bureau in New York*, 2:60–62, 1974.
- [MLS99] M. R. Malik, R. S. Lin, and R. Sengupta. Computation of hypersonic boundary-layer response to external disturbances. AIAA Paper 1999–0411, 1999.
- [Mor69] M. V. Morkovin. Critical evaluation of transition from laminar to turbulent shear layers with emphasis on hypersonic traveling bodies. AFRL Report AFF DL–TR–68–149, Air Force Flight Dynamics Laboratory, Wright-Patterson AFB, OH, USA, 1969.
- [MSSA01] A. A. Maslov, A. N. Shiplyuk, A. A. Sidorenko, and D. Arnal. Leading-edge receptivity of a hypersonic boundary layer on a flat plate. *J. Fluid Mech.*, 426:73–94, 2001.
- [MZ03a] Y. Ma and X. Zhong. Receptivity of a supersonic boundary layer over a flat plate. Part 1: Wave structures and interactions. *J. Fluid Mech.*, 488:31–78, 2003.
- [MZ03b] Y. Ma and X. Zhong. Receptivity of a supersonic boundary layer over a flat plate. Part 2: Receptivity to freestream sound. *J. Fluid Mech.*, 488:79–121, 2003.
- [Nay80] A. H. Nayfeh. Stability of three-dimensional boundary layers. *AIAA J.*, 18:406–416, 1980.
- [OML69] H. J. Obremski, M. V. Morkovin, and M. Landahl. A portfolio of stability characteristics of incompressible boundary layers. AGARDograph 134, Paris, 1969.
- [Pan05] R. L. Panton. *Incompressible flow*. John Wiley and Sons, 2005. 3rd edition.
- [PN79] A. R. Padhye and A. H. Nayfeh. Nonparallel stability of three-dimensional flows. AIAA Paper 79–1281, 1979.
- [Res76] E. Reshotko. Boundary-layer stability and transition. *Ann. Rev. Fluid Mech.*, 8:311–349, 1976.
- [Res01] E. Reshotko. Transient growth: A factor in bypass transition. *Phys. Fluids*, 13:1067–1075, 2001.

- [Rey83] O. Reynolds. An experimental investigation of the circumstances which determine whether the motion of water shall be direct or sinuous, and of the law of resistance in parallel channels. *Phil. Trans. Roy. Soc London A*, 174:935–982, 1883.
- [RS89] H. L. Reed and W. S. Saric. Stability of three-dimensional boundary layers. *Ann. Rev. Fluid Mech.*, 21:235–284, 1989.
- [RT04] E. Reshotko and A. Tumin. Role of transient growth in roughness-induced transition. *AIAA J.*, 42(4):766–770, 2004.
- [RT06] E. Reshotko and A. Tumin. Application of transient growth theory to bypass transition. In G. E. A. Meier, K. R. Sreenivasan, and H. J. Heinemann, editors, *One hundred years of boundary layer research*, pages 83–93. Springer, 2006.
- [RT08] D. Rodríguez and V. Theofilis. On instability and structural sensitivity of incompressible laminar separation bubbles in a flat-plate boundary layer. *AIAA Paper* 2008–4148, 2008.
- [RV07] D. P. Rizzetta and M. R. Visbal. Direct numerical simulations of flow past an array of distributed roughness elements. *AIAA J.*, 45:1967–1976, 2007.
- [SAD<sup>+</sup>09] K. A. Stephani, J. Albright, C. Doolittle, M. Jackson, and D. Goldstein. Dns study of transient disturbance growth and bypass transition. *AIAA Paper* 2009–0585, 2009.
- [Sar94a] W. S. Saric. Görtler vortices. *Ann. Rev. Fluid Mech.*, 26:379–409, 1994.
- [Sar94b] W. S. Saric. Low-speed boundary-layer transition experiments. In T. C. Corke, M. Y. Erlebacher, and M. Y. Hussaini, editors, *Transition: experiments, theory and Computations*, pages 1–114. Oxford, 1994.
- [Sar07] W. S. Saric. Boundary-layer stability and transition. In C. Tropea, A. Yarin, and J. F. Foss, editors, *Handbook of experimental fluid mechanics*, pages 886–896. Springer-Verlag, 2007.
- [SB80] F. T. Smith and R. J. Bodonyi. On the stability of the developing flow in a channel in circular pipe. *Quart. J. Mech. Appl. Math.*, 33:293–320, 1980.
- [SFK00] S. Bakke S, H. H. Fernholz, and Y. S. Kachanov. Resemblance of k- and n-regimes of boundary-layer transition at late stages. *Eur. J. Mech. B-Fluids*, 19:1–22, 2000.
- [SG81] H. Salwen and C. E. Grosch. The continuous spectrum of the Orr–Sommerfeld equation. Part 2. eigenfunction expansion. *J. Fluid Mech.*, 104:445–465, 1981.
- [SG00] H. Schlichting and K. Gersten. *Boundary layer theory*. Springer, 2000. 8th edition.

- [SH01] P. J. Schmid and D. S. Henningson. *Stability and Transition in Shear Flows*. Springer, New York, 2001.
- [Smi59] A. M. O. Smith. Transition, pressure gradient and stability theory. *J. Aerospace Sci.*, 26:229–245, 1959.
- [Smi79] F. T. Smith. On the non-parallel flow stability of the blasius boundary layer. *Proc. Roy. Soc. London*, A366:91–109, 1979.
- [SN75] W. S. Saric and A. H. Nayfeh. Nonparallel stability of boundary-layer flow. *Phys. Fluids*, 18(8):945–950, 1975.
- [SN77] W. S. Saric and A. H. Nayfeh. Nonparallel stability of boundary layers with pressure gradients and suction. Technical Report AGARD-CP-224, 1977.
- [Squ33] H. B. Squire. On the stability for three-dimensional disturbances of viscous fluid flow between parallel walls. *Proc. Roy. Soc., Series A*, 142(847):621–628, 1933.
- [SR94] G. K. Stuckert and H. L. Reed. Linear disturbances in hypersonic, chemically reacting shock layers. *AIAA J.*, 32:1384–1394, 1994.
- [SRK02] W. S. Saric, H. L. Reed, and E. J. Kerschen. Boundary-layer receptivity to free-stream disturbances. *Ann. Rev. Fluid Mech.*, 34:291–319, 2002.
- [SRW03] W. S. Saric, H. L. Reed, and E. B. White. Stability and transition of three-dimensional boundary layers. *Ann. Rev. Fluid Mech.*, 35:413–440, 2003.
- [SS43] G. B. Schubauer and H. K. Skramstad. Laminar boundary layer oscillations and transition on a flat plate. NACA-TR 909, 1943.
- [Stu91] G. K. Stuckert. *Linear Stability of Hypersonic, Chemically Reacting Viscous Flows*. Phd thesis, Arizona State University, 1991.
- [TF82] A. M. Tumin and A. V. Fedorov. On the weakly nonparallel flow effect on characteristics of flow stability. *Uchenye Zapiski TsAGI*, 13(6):91–96, 1982. (in Russian).
- [TF83] A. M. Tumin and A. V. Fedorov. Spatial growth of disturbances in a compressible boundary layer. *J. Appl. Mech. Tech. Phys.*, 24:548–554, 1983.
- [The03] V. Theofilis. Advances in global linear instability analysis of nonparallel and three-dimensional flows. *Prog. Aero. Sci.*, 39:249–315, 2003.
- [Tum03] A. Tumin. Multimode decomposition of spatially growing perturbations in a two-dimensional boundary layer. *Phys. Fluids*, 15:2525–2540, 2003.
- [Tum06a] A. Tumin. Biorthogonal eigenfunction system in the triple-deck limit. *Studies in Applied Mathematics*, 117:165–190, 2006.

- [Tum06b] A. Tumin. Receptivity of compressible boundary layers to three-dimensional wall perturbations. AIAA Paper 2006-1110, 2006.
- [Tum07] A. Tumin. Three-dimensional spatial normal modes in compressible boundary layers. *J. Fluid Mech.*, 586:295–322, 2007.
- [Tum08] A. Tumin. Nonparallel flow effects on roughness-induced perturbations in boundary layers. *J. Spacecraft and Rockets*, 45(1):1176–1184, 2008.
- [Tum09] A. Tumin. Toward the foundation of a global (bi-global) modes concept. In V. Theofilis, T. Colonius, and A. Seifert, editors, *Global Flow Instability and Control-IV*, Creta Maris, Hersinissos, Crete, 2009. ISBN-13: 978-84-692-6247-4.
- [Tum10] A. Tumin. Flow instabilities and transition. In R. Blochley and W. Shyy, editors, *Encyclopedia of Aerospace Engineering*, pages 139–150. John Wiley & Sons Ltd, 2010. Chichester, UK.
- [TWZ07] A. Tumin, X. Wang, and X. Zhong. Direct numerical simulation and the theory of receptivity in a hypersonic boundary layer. *Phys. Fluids*, 19(1), 2007. paper 014101.
- [TWZ10] A. Tumin, X. Wang, and X. Zhong. Numerical simulation and theoretical analysis on hypersonic boundary-layer receptivity to wall blowing-suction. AIAA Paper 2010-0534, 2010.
- [TWZ11] A. Tumin, X. Wang, and X. Zhong. Numerical simulation and theoretical analysis of perturbations in hypersonic boundary layers. *AIAA J.*, 49(3), 2011. To appear.
- [UKT11] E. Ulker, J. Klentzman, and A. Tumin. Stability of boundary layers in binary mixtures of oxygen and nitrogen. AIAA Paper 2011-0370, 2011.
- [Ulk10] E. Ulker. Boundary layer solvers for binary reacting mixtures of oxygen and nitrogen, and for 5-species model of air, 2010.
- [vI56] J. L. van Ingen. A suggested semi-empirical method for the calculation of boundary layer transition region. Report UTH-74, Univ of Technol., Dept. of Aero. Eng., Delft, Netherlands, 1956.
- [WE03] E. B. White and F. E. Ergin. Receptivity and transient growth of roughness-induced disturbances. AIAA Paper 2003-4243, 2003.
- [Whi02] E. B. White. Transient growth of stationary disturbances in a flat plate boundary layer. *Phys. Fluids*, 14:4429–4439, 2002.
- [WRE05] E. B. White, J. M. Rice, and F. G. Ergin. Receptivity of stationary transient disturbances to surface roughness. *Phys. Fluids*, 17, 2005. paper No. 064109.

- [WZ09] X. Wang and X. Zhong. Effect of wall perturbations on the receptivity of a hypersonic boundary layer. *Phys. Fluids*, 21, 2009. Paper 044101.
- [WZ23] X. Wang and X. Zhong. Role of the synchronization point on boundary layer stabilization using porous coating. AIAA Paper 2008-4382, 23.
- [Zho98] X. Zhong. High-order finite-difference schemes for numerical simulation of hypersonic boundary-layer transition. *Journal of Computational Physics*, 144:662–709, 1998.
- [ZR83] V. I. Zhuk and O. S. Ryzhov. On asymptotic solution of the orr-sommerfeld equation for unstable perturbations at high reynolds numbers. *Dokl. Akad. Nauk SSSR*, 268:1328–1332, 1983. in Russian.
- [ZT87] V. N. Zhigulev and A. M. Tumin. *Origin of Turbulence*. Nauka, Novosibirsk, 1987. (in Russian) [NASA TT-20340, October 1988 (translated)].
- [ZTR06] S. Zuccher, A. Tumin, and E. Reshotko. Parabolic approach to optimal perturbations in compressible boundary layers. *J. Fluid Mech.*, 556:189–216, 2006.
- [Zuc06a] S. Zuccher. 4th order finite difference solver for compressible optimal perturbations over a sharp cone. Contractor’s report, Tucson, 2006.
- [Zuc06b] S. Zuccher. 4th order finite difference solver for compressible optimal perturbations over an axisymmetric body of revolution. Contractor’s report, Tucson, 2006.
- [Zuc06c] S. Zuccher. General finite-difference solver for compressible optimal perturbations in supersonic flows. Contractor’s report, Tucson, 2006.